Università degli Studi di Padova

Università degli Studi di Padova
Dipartimento di Fisica e Astronomia "Galileo Galilei"
Corso di Dottorato di Ricerca in Fisica - Ciclo XXIX

in cotutela con:
Universidad de Sevilla
Departamento de Física Atómica, Molecular y Nuclear
Programa de Doctorado en Ciencias y Tecnologías Físicas

Structure and reactions of weakly-bound nuclei within a one-dimensional model

---

Coordinatore: Ch.mo Prof. Gianguido Dall'Agata

Supervisori: Ch.mo Prof. Andrea Vitturi
Ch.mo Prof. Antonio M. Moro Muñoz

Dottoranda: Laura Moschini

Abstract

The line of research developed within the present work is the description of the structure and the dynamics of weakly-bound systems with one or more valence particles. Even considering inert cores, the problem is relatively easy only with one valence particle (one-particle halo), and starts to be more complex with two particles (two-particle halo), becoming extremely complicated for systems with more active particles. For these reasons one typically resorts to approximated schemes (coupled- channels, first order approximation, space truncation, effective optical potentials and form factors, continuum discretization, etc) that need to be tested, not only against experimental data. So the main purpose of this work is the comparison between approximate models and exact ones. However, mathematical complexities and the high computational power required constitute a huge difficulty. Therefore, to make feasible the solution of the problem, particles are assumed to move just in one dimension and nuclei move according to a classical trajectory. In spite of the drastic assumptions, the problem retains the main features and properties of a full three-dimensional case. In addition, one could shed some light on the reaction mechanism, namely, on the description of the process in terms of single or repeated action of the external field in a perturbative expansion. A typical example is provided by the two-particle transfer process: is the pair transferred in a single step or in a correlated sequence of two single-particle transfer through a number of intermediate states?
In the case of one-particle halo nuclei, the process involves one active neutron initially sitting on a single-particle level of a one-body Woods-Saxon potential (target) and feeling the action of a second moving potential (projectile). The target potential is assumed to be at rest in a fixed position, whereas the projectile moves following a fixed classical trajectory. The choice of the parameters entering the calculation will lead to various structural and kinematical conditions, corresponding to rather different physical situations

and simulating different bombarding energy regimes, impact parameters, and Q-values for particle transfer. Essentially, one has to fix the parameters characterizing the potential wells (energies of single-particle states in both potentials), initial wavefunction (selecting one of the levels in target potential), distance of closest approach, and asymptotic energy of the collision. The "exact" results can be obtained by directly solving the time-dependent Schroedinger equation. The probability for populating the different channels after the collision is determined by projecting the asymptotic wavefunction (i.e. the solution for large values of t) onto the corresponding eigenstates of the wells. The same equation is solved within the first order approximation and standard coupled-channels formalism, thus testing the validity of the necessary truncations and continuum discretization (that is obtained through different methods). In particular, by this comparison, one might infer the importance of including the continuum to obtain the proper result expected from the "exact" calculation, even if the system is not very weakly-bound.
In the case of two-particle halo nuclei, as in previous case, the initial two-particle state is generated by the fixed well and the time evolution of the two-particle wave function is due to the action of two moving one-body potentials along a classical trajectory. In addition, one can include a residual short-range pairing interaction between the two valence particles. For simplicity the pairing interaction is taken to be a density-dependent zero-range potential, and hence it acts only when the two particles are both inside the same well. Again, the solution is obtained by solving the time-dependent two-particle Schroedinger equation. At the end of the process one can single out the population of the different final channels: elastic/inelastic (both particles still in the initial well), one-particle transfer (one particle in the initial well and one in the moving one), one-particle breakup (one particle in the continuum outside the wells and one in the initial or final well), two-particle transfer (both particles in the moving well), and breakup (one or both particles outside the wells). For the two-body process one can study the reaction mechanism by switching on or off the pairing interaction. Due to the absence of correlations the transfer process is induced by the one-body mean-field generated by the moving wells and, in terms of reaction mechanism, the two-particle transfer can only be interpreted as produced by the successive transfer of single particles. In the correlated case the probability of finding both particles on the same side is clearly favored, and the effect of this

initial correlation will propagate during the scattering process. In fact one finds a final probability larger than that for the uncorrelated estimate. This rapresents therefore the enhancement factor due to the pairing correlation. In conclusion, despite its simplicity, the model provides a framework for the understanding of direct reactions mechanisms involving one- and two-particle halo nuclei. In particular, it permits to test in a simple way the role of continuum and usual approximate approaches. It also allows to prove the role of pairing interaction between the two valence particles.

Acknowledgements

I would like to thank my supervisors, Andrea and Antonio, for having taught me how fundamental is in research to achieve the most general, simple, and clean overall view, without forgetting details and subtle shades.
I also thank all the people of Dipartimento di Fisica e Astronomia "G. Galilei" of Padova (Italy) and Departamento de Física Atómica, Molecular y Nuclear of Sevilla (Spain), where I have been working for the past three years, for the warm and friendly hospitality. In particular, I am thankful to Curro Pérez-Bernal and José Antonio Lay for the useful discussions and precious suggestions.
I finally wish to thank all my family for their unconditional support.

Laura

November 2016

Contents

List of Figures

List of Tables

Chapter 1

Introduction

One of the most relevant research lines in nowadays nuclear physics is the investigation, both experimentally and theoretically, of nuclei under extreme conditions and, in particular, nuclei far from the stability line (nuclei highligted in black in figure 1.1). Nuclei that do not bind more neutrons define on the isotope chart the neutron drip line (solid line on the left indicates proton drip line and solid line on the right marks neutron drip line in figure 1.1). Along this line truly enticing and striking novel nuclear structure phenomena are being observed. In particular, these so-called exotic nuclei present low proton or neutron separation energy, short lifetime, and a radius which noticeably deviates from the $A^{1/3}$ dependence of stable nuclei, a fact that is related to a skin or a halo structure [1, 2]. The excess of

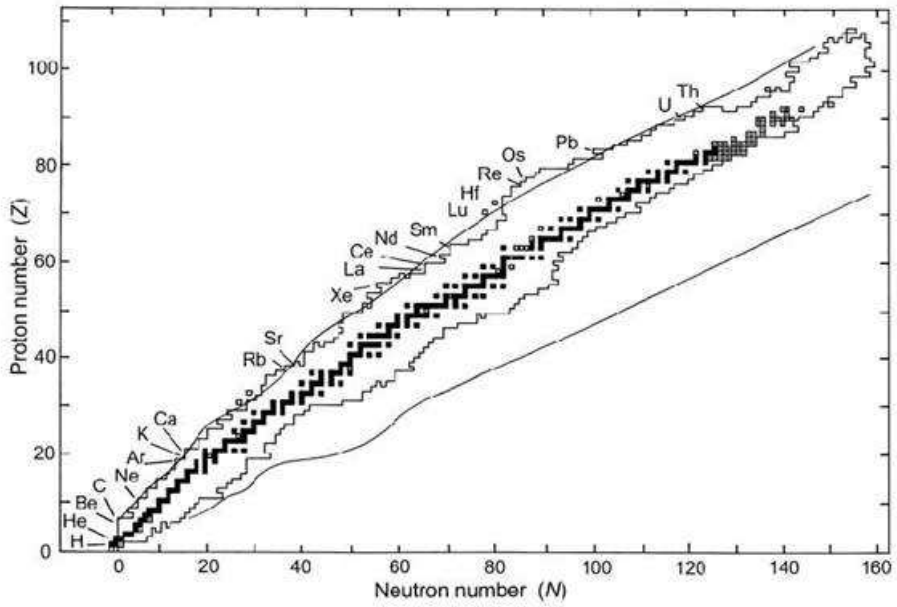

Figure 1.1: The nuclear chart mapping the existing nuclei. The black squares in central zone are stable nuclei. The outer lines denote the theoretical estimate for the proton and neutron drip lines.

neutrons or protons also leads to a different rearrangement which is generally described as deformation: this is indicated by new single-particle character of states and new magic numbers related to new shell closure [3, 4]. Because of the large spatial separation between the centre-of-mass and the centre-of-charge, in presence of an extenal electric field low energy electric dipole

oscillations can result, as well as very clear cluster effects [5]. Nowadays measuring the properties of such nuclei is the goal of the main experimental nuclear facilities around the world [6, 7]. Due to their short lifetimes targets of such nuclei are impossible to be constructed, so they can not be studied by usual spectroscopic tecniques. Thus, the challenge to measure nuclei on the drip lines has made possible the development of radioactive nuclear beams. From a theoretical point of view, the conventional theories valid for the description of stable nuclei are no longer able to describe exotic systems, thus indicating the necessity to improve them and include the description of the new phenomena taking place at the limits of stability, taking into account the new features. An advantage of nuclear physics is the communication and cooperation of both experimental and theoretical sides to go forward in the knowledge of nuclei.

As we have seen, examples of exotic systems are nuclei with large neutron excess, with the barely bound outermost ones creating an extended density distribution, named as halo. There can be different kinds of halo systems, as shown in figure 1.2. A nucleus with one valence neutron is for example ^{11}Be, on the other side ^{8}B is a nucleus presenting a one proton halo[1]. Particular

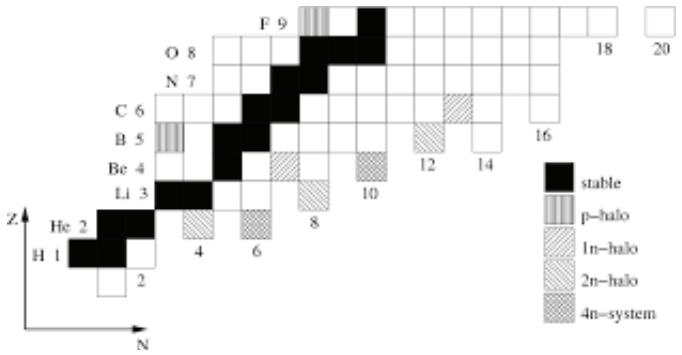

Figure 1.2: The nuclear chart, zoom on the light nuclei area. Black cells indicate stable nuclei, halo nuclei are highlighted by striped cells.

halo systems, the two-neutron halo nuclei, are the so-called Borromean. Borromean nuclei are three-body systems[2] with at least one bound state but

[1] Due to the Coulomb barrier the proton halo is suppressend, for this reason proton drip line is closer to the stability valley than the neutron drip line

[2] We consider here those systems composed by an inert core plus two particles.

with no bound binary sub-systems. The best known examples of Borromean nuclei are ^{6}He and ^{11}Li, but other Borromean nuclear systems have been proposed, e.g. ^{14}Be and ^{22}C [8]. The pairing interaction, which tends to couple the nucleons to spin 0, seems to play an important role in binding those systems and in the reaction mechanism involving Borromean nuclei [9].

The theoretical description of halo nuclei is strongly characterized by its weakly-bound nature. To understand this point let us consider a schematic picture in which the nucleus is modeled with a mean field potential filled with nucleons (protons and neutrons). Bound nuclei in the vicinity of the stability valley partially occupy the available bound states, as it is schematically depicted in figure 1.3a. In this configuration the lowest nuclear excitations can be obtained by promoting one or more nucleons to the still bound higher energy states, as shown in figure 1.3b. How is this simplified picture affected as nuclei get close to the neutron drip line? In this case the neutrons occupy all the bound levels so that the neutron Fermi energy approaches to zero, as shown in figure 1.3c, and the corresponding neutron excited states must involve the promotion of a neutron to continuum states (figure 1.3d). The last nucleons are so weakly-bound that the addition of any correlation to the simple mean field model inevitably involves the inclusion of the continuum in the system description. For this reason the description of their structure or dynamics is more involved (above all for more than two valence particles), even considering inert cores.

1.1 Nuclear reactions

Most of our present knowledge of stable and exotic nuclei stems from the analysis of nuclear reactions. As schematically shown in figure 1.4, these processes are traditionally separated into two groups: compound nucleus and direct reactions [10].

Compound nucleus reactions are those processes in which the colliding elements fuse to form an intermediate system, the compound nucleus, which successively decays by evaporating nucleons or γ-rays to different final nuclei. In this case the final systems do not have any "memory" of the initial reacting nuclei (a + A $\rightarrow$ C $\rightarrow$ b + B). On the other hand, direct reactions refer to collisions in which the nuclei make "glancing" contact and immediately

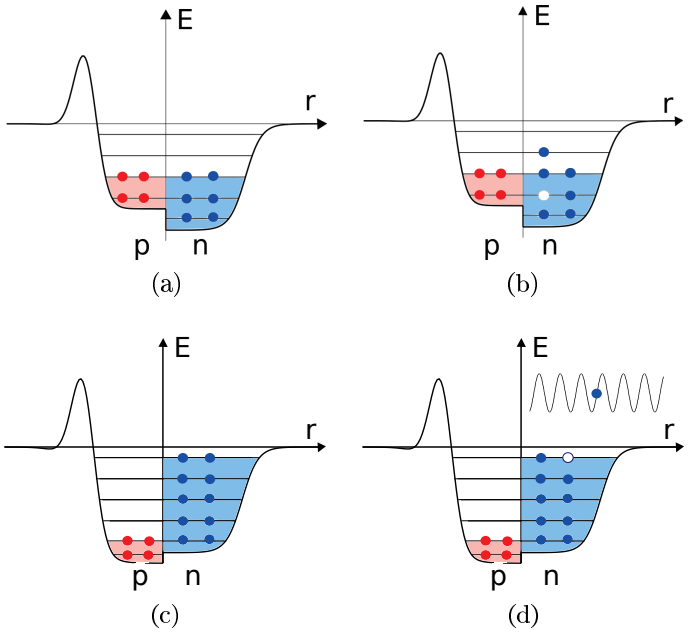

Figure 1.3: Schematic single-particle configuration of the ground-state (a) and its particle-hole excitation (b) for a nucleus close to the stability valley. Corresponding situation for a system close to the neutron drip line, with ground-state (c) and its excitation of a nucleon to the continuum (d). Note that the dominant interaction is n-p interaction, but in configurations (c) and (d), characterized by an excess of neutrons, the result is a less bound neutron well.

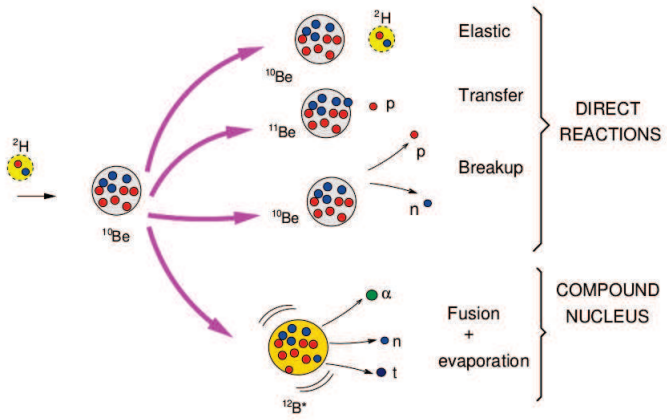

Figure 1.4: Schematic representation of compound nucleus and direct reactions.

separate, they are said to be peripheral or surface processes. The colliding nuclei preserve their "identity" (a + A $\rightarrow$ a* + A*). Direct reactions are characterized by different channels: elastic and inelastic scattering, transfer of nucleons between the colliding nuclei, breakup (i.e. excitation to positive energy states).

It is possible to have direct and compound-nucleus processes both contribute to a given reaction, but usually each one corresponds to a precise regime. For example, direct processes occur very rapidly in a time of the order of 10^{-10} ps, while a compound process tipically takes much longer, perhaps 10^{-4} to 10^{-6} ps. Another threashold is the de Broglie wavelength $\lambda = 2\pi\hbar c/E$ [11]: as the energy of the incident particle is increased, its de Broglie wavelength decreases, until it becomes more likely to interact with a nucleon-sized object than with a nucleus-sized object. So a 1 MeV incident nucleon has a de Broglie wavelength of about $\lambda = 4$ fm, and thus does not "see" individual nucleons; it is more likely to interact through a compound-nucleus reaction. Meanwhile, a 20 MeV nucleon has a de Broglie wavelength of about $\lambda = 1$ fm and therefore may be able to partecipate in direct processes. Direct processes are most likely to involve one nucleon or very few valence nucleons near the surface of the projectile or target nuclei, in a one-step process. The emphasis on a simple, one-step process means a tendency for only small amounts of momentum to be transferred in a direct reaction [10], hence the angular distribution of the reaction products tends to be asymmetric about 90^o and to be peaked at forward angles. The angular dependence of a direct reaction is forward peaked, since the interaction is restricted mainly to peripheral collisions from which the outgoing particle will carry most of the incident energy and momentum of the projectile, and this allows the angular distribution peak to be narrow (localized in scattering angle). The characteristic angular distribution of particles evaporated from a compound nucleus is generally more isotropic and symmetric around 90^o. Furthermore, direct reactions are expected to vary slowly as the bombarding energy is changed.

As we mentioned, direct nuclear reactions are useful tools to investigate nuclear structure, because a direct reaction will feed a particular channel in a way that depends sensitively on its character. In particular, inelastic scattering excites collective states strongly; one-neutron transfer probes the single-particle character of states; two-nucleon transfer goes preferentially to

states that exhibit strong pairing correlations; pairing could also be tested via multi-nucleon transfer, as well as clustering; the role of continuum is investigated through breakup reactions. This is of particular value in probing different aspects of nuclear structure.

1.2 Direct reactions models

In this thesis we focus our attention on direct reactions involving nuclei with one valence neutron and in Borromean nuclei. For that, we need to apply a scattering theory. The final goal of the scattering theory is to develop appropriate models to which compare the measured observables, with the aim of extracting information on the structure of the colliding nuclei as well as understanding the dynamics governing these processes. The measured quantities are typically total or partial cross sections with respect to angle and/or energy of the outgoing nuclei. Therefore, the challenge of reaction theory is to obtain these cross sections by solving the dynamical equations of the system (at non-relativistic energies, the Schoroedinger equation) with a realistic but amenable structure model of the colliding nuclei. By solving the Shroedinger equation, one obtains the wavefunction of the system. This wavefunction will be a function of the degrees of freedom (e.g. internal coordinates) of the projectile and target, denoted generically as ξ_P and ξ_T, as well as of the relative coordinate between them ($\mathbf{R}$). Thus we will express the total wavefunction as $\Psi(\mathbf{R}, \xi_P, \xi_T)$. The system Hamiltonian is

$$\mathcal{H} = \hat{T}_{\mathbf{R}} + \mathcal{H}_P(\xi_P) + \mathcal{H}_T(\xi_T) + V(\mathbf{R}, \xi_P, \xi_T), \tag{1.1}$$

where $\hat{T}_{\mathbf{R}} = -\frac{\hbar^2}{2\mu}\nabla^2_{\mathbf{R}}$, $\mathcal{H}_P(\xi_P)$ ($\mathcal{H}_T(\xi_T)$) denotes the projectile (target) internal Hamiltonian, and $V(\mathbf{R}, \xi_P, \xi_T)$ is the projectile-target interaction. After the collision, the projectile and the target may excange some nucleons, or even break up, so the Hamiltonian (1.1) corresponds actually to the entrance channel. To denote the possible mass partitions that may arise in a reaction, we will denote α as the initial partition and β as the final one. So the previous Hamiltonian is rewritten as

$$\mathcal{H} = \hat{T}_\alpha + \mathcal{H}_\alpha(\xi_\alpha) + V_\alpha(\mathbf{R}_\alpha, \xi_\alpha), \tag{1.2}$$

where ξ_α denotes the projectile and target internal coordinates in partition α. The total energy of the system is given by the sum of the kinetic energy (E_α) and the internal energy of projectile and target (ϵ_α)

$$E = E_\alpha + \epsilon_\alpha = \frac{\hbar^2 k_\alpha^2}{2\mu_\alpha} + \epsilon_\alpha \tag{1.3}$$

where $\hbar\mathbf{k}_\alpha$ is the linear momentum. The wavefunction $\Psi(\mathbf{R}, \xi)$ will be a solution of the time independent Schroedinger equation

$$[\mathcal{H} - E]\,\Psi_{\mathbf{k}} = 0. \tag{1.4}$$

This is a second order differential equation that must be solved subject to the appropriate boundary conditions, which must reflect the nature of a scattering process.

In a time-independent picture, typical of the quantum approach, the incident beam is represented by a plane wave[3]. After the collision with the target, a set of outgoing spherical waves will be formed. The situation is schematically depicted in figure 1.5.

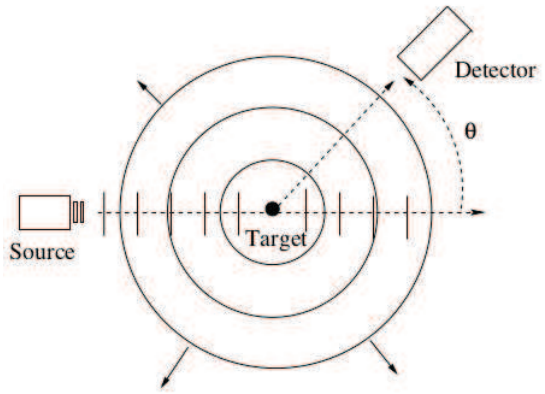

Figure 1.5: Schematic representation of a scattering process.

[3]This is true only for the case of short-range potentials; in presence of Coulomb potential the incient wavefunction is represented by a Coulomb wave.

So, asymptotically

$$\Psi^{(+)}_{\mathbf{k}_0}(\mathbf{R},\xi) \to \Phi_0(\xi)e^{i\mathbf{k}_0\cdot\mathbf{R}} \quad + \text{ outgoing spherical waves,} \tag{1.5}$$

with $\Phi_0(\xi) \equiv \Phi^0_P(\xi_P)\Phi^0_T(\xi_T)$, and where the superscript "+" indicates that this corresponds to the solution with outgoing boundary conditions (mathematically, one may construct also the solution with incoming boundary conditions).

During the collision, the incident wave will be highly distorted by the projectile-target interaction but, after the collision, at sufficiently large distances (that is, when V becomes negligible), the projectile and target will manifest any of the kinematically allowed eigenstates of the system. So, asymptotically, we may write[4]

$$\begin{aligned}\Psi^{(+)}_{\mathbf{k}_\alpha} \xrightarrow{R_\alpha \gg} & \Phi_\alpha(\xi_\alpha)e^{i\mathbf{k}_\alpha\cdot\mathbf{R}_\alpha} + \Phi_\alpha(\xi_\alpha)f_{\alpha,\alpha}(\theta)\frac{e^{ik_\alpha R_\alpha}}{R_\alpha} \\ & + \sum_{\alpha'\neq\alpha}\Phi_{\alpha'}(\xi_\alpha)f_{\alpha',\alpha}(\theta)\frac{e^{ik_{\alpha'}R_\alpha}}{R_\alpha} \\ \Psi^{(+)}_{\mathbf{k}_\alpha} \xrightarrow{R_\beta \gg} & \sum_\beta \Phi_\beta(\xi_\beta)f_{\beta,\alpha}(\theta)\frac{e^{ik_\beta R_\beta}}{R_\beta}.\end{aligned} \tag{1.6}$$

First, second, and third lines correspond to elastic, inelastic, and transfer channels, respectively. The angle θ is the CM scattering angle, and corresponds to the angle between the incident and final momenta ($\mathbf{k}_\alpha$ and $\mathbf{k}_\beta$). Note that $\mathbf{k}_\beta$ and $\mathbf{R}_\beta$ are parallel. The function $\frac{e^{ik_\beta R_\beta}}{R_\beta}$ is a spherical outgoing wave. The function multiplying this outgoing wave is the scattering amplitude for channel β. The differential cross section for particles scattering in the direction θ in channel β is defined as the flux of scattered particles through the area $dA = r^2 d\Omega$, per unit incident flux. This quantity is directly related to the scattering amplitude as

$$\left(\frac{d\sigma}{d\Omega}\right)_{\alpha\to\beta} = \frac{\mu_\alpha}{\mu_\beta}\left|\frac{k_\beta}{k_\alpha}f_{\beta,\alpha}(\theta)\right|^2. \tag{1.7}$$

[4]Note that we distinguish between R_α and R_β since, for a riarrangement process, the coordinate will be different.

1.2.1 Semiclassical solution to the scattering problem

When the de Broglie wave length associated to the projectile motion is small compared to the size of the scatterer, one may solve the scattering problem making use of a semiclassical picture, in which the projectile-target relative distance is described by means of a classical trajectory, but keeping the quantum-mechanical description of the projectile and target internal motion. This approach is possible when the cross sections of the reactions involving heavy nuclei does not present the typical oscillations of the interference patterns of a quantum interaction. An andvantage of semiclassical methods is that, from a computational point of view, they are less demanding as compared to fully quantum-mechanical methods.
In the semiclassical theory the target-projectile interaction is time-dependent, because the distance $\mathbf{R}$ between target and projectile is changing with time; for a given impact parameter b the projectile-target relative motion is given by a classical trajectory $\mathbf{R}(t)$, and the intrinsic dynamics is treated as a time-dependent quantum mechanics problem [12]. Therefore for the semiclassical calculation, the coupling interaction is time-dependent $V(\mathbf{R}, \xi_P, \xi_T) \equiv V(\mathbf{R}(t), \xi_P, \xi_T)$. The problem is traditionally solved in the so-called coupled-channels approach (or in its lower order approximations in presence of strong transitions) in which the wavefunction of the system is expressed as an expansion in a basis of internal states of the system, with some time-dependent coefficients

$$|\Psi(t)\rangle = \sum_{j=1}^{N} c_j(b,t)|\Phi_j\rangle e^{iE_j t/\hbar} + |\Psi_C(t)\rangle, \tag{1.8}$$

where $|\Psi_C(t)\rangle$ is the component of the wavefunction in the continuum, and N is the number of bound states $|\Phi_j\rangle$ of the system. The solution of the problem moves to the study of the evolution in time of the coefficients $c_i(b,t)$ corresponding to each reaction channel i given the impact parameter b. The time evolution of these coefficients is obtained from the time-dependent Schroedinger equation with Hamiltonian

$$\mathcal{H} = \hat{T}_{\mathbf{R}} + \mathcal{H}_P(\xi_P) + \mathcal{H}_T(\xi_T) + V(\mathbf{R}(t), \xi_P, \xi_T). \tag{1.9}$$

As the collision proceeds the amplitudes $c_i(b,t)$ evolve, and their final values contain the relevant information on the probability of the corresponding channels, e.g. the final probability to excite the i-th channel for an impact paramenter b is $\mathcal{P}_i = |c_i(b,t_f)|^2$.

The application of scattering theory to weakly-bound systems has lead to the development and extension of reactions formalisms to account for the effects of the coupling to breakup channels on reaction observables. These methods must take into account the new features of exotic nuclei. In particular one has to deal with continuum, and this usually involves a procedure of defining, discretizing and truncating continuum states. Many approaches have been developed: continuum-discretized coupled-channels (CDCC) method [13, 14], the adiabatic approximation [15, 16], and a variety of semiclassical approximations [12, 17–19].
Typically, these approaches make use of a few-body description of the weakly-bound systems, which, in the case of halo nuclei, consists of a core plus one or two weakly bound valence particles.

Extensions of existing formalisms to include excitations of the involved clusters is also an intense topic being currently addressed by several groups [20–25].

1.3 Why a one dimensional model?

As we have seen many models to describe these processes are available and usually compared to experimental data. But since these models are based on approximations, not always the exact solution can be obtained, e.g. for problems related to basis choice, uniqueness or convergence. The different approximations and subsequent limitations should be tested. In particular, in this thesis we are interested in understanding the role of continuum in direct reactions mechanism and how to include it properly in a CDCC calculation. As example, let us consider the $^{11}Be + p \rightarrow n + p +^{10} Be$ breakup reaction. In CDCC, this process would be treated as an inelastic excitation of ^{11}Be to its two-body continuum, i.e. $^{11}Be{+}p \rightarrow (^{10}Be{+}n){+}p$. This approach will be valid to describe final situations in which the outgoing n and ^{10}Be fragments are detected with a small relative energy and angular momentum, thus populating low-lying states of the ^{11}Be continuum. For large energy

and/or angular-momentum transfer, the CDCC expansion may require a very large model space, and the convergence of the reaction observables as the model space increases can be very slow. In this case, an expansion in terms of $p-n$ states (including deuteron continuum) may be more apropriate. Each basis selection tends to emphasize the properties of a given binary system, partially neglecting correlations on the other binary systems. This will give rise to some limitations of the CDCC model, for example, when both transfer and breakup are important [26–28].

A more complete reaction theory which incorporates on equal footing the correlations between the different binary sub-systems is provided by the Faddeev formalism. Recently, it has become possible to solve the Faddeev equations for nuclear reactions involving light systems, thus providing a very useful benchmark for more approximate theories, like CDCC [29, 30]. However, these calculations are sometimes bias by numerical and convergence difficulties. Moreover, the complexity of the Faddeev method limits so far its applicability to relatively light systems.

Since we would like to face the problem in the simplest framework possible, we move to one dimension (1D) where, despite the drastic assumption, the model encompasses many features found in the three-dimensional case. In particular, the influence of the positive energy states on the scattering observables can be studied in this framework.

Within this assumption, we model the reaction following the time evolution of the wave function of the system

$$\Psi(x,t) = \sum_{j=1}^{N} c_j(t)\Phi_j(x)e^{iE_jt/\hbar}, \tag{1.10}$$

where N is the number of basis states including bound and discretized continuum states. In the frame of a semiclassical approach, we start from an initial wavefunction $\Psi(x,t_i)$ describing system at $t_i = -\infty$, we let the system evolve in time by solving the time-dependent Schroedinger equation to obtain at $t_f = +\infty$ the final wavefunction $\Psi(x,t_f)$. In this simplified case it is possible to follow easily the time evolution for both the exact total wavefunction $\Psi(x,t)$ and the set of coefficients $c_i(t)$: the exact solution can be compared with the results obtained by expanding the wavefunction in a basis that includes discretization of the positive energy part of the spectrum

as in the CDCC approach. We can thus check the validity of the different approximations connected to the different discretization methods.

Although the simplification achieved devising our 1D model precludes us from comparing directly to real nuclei, we expect that the present model, notwithstanding its simplicity, contains the basic physical ingredients for a correct description of the problem under study. A solution of a simplified model frequently sheds light upon a physical problem whose full solution is hindered by mathematical complexities or is simply not possible.

Different aspects of the one dimensional problem have been already developed and discussed in many papers. Reduced dimensionality models of application in nuclear physics can be found e. g. in [31–33]. In [34] the authors discuss the problem of the excitation to the continuum (breakup) of a particle, initially moving in a single-particle orbit of a one-dimensional well, due to the action of an external perturbation (simulating the interaction with a reaction partner). In [35] the exact solution for the same scattering problem we proposed here is compared to the results of a CDCC model, but without including the continuum. In [36–38] the structure of a two-particle Borromean system, bound to the action of a residual pairing interaction, is investigated. In [39] the autors investigate the break-up of such Borromean systems due to the action of an external one-body field, pointing out the role of the residual pairing interaction in enhancing the correlated two-particle breakup in comparison with the single-particle breakup. In particular, some results for the model investigated in the present thesis can already be found in [40] with regard to the structure aspects, and in [41–43] and [44] for the one- and two-neutron systems dynamics.

1.4 Summary

In accordance with this picture we present in this dissertation results for a one-dimensional (1D) model of two particular kinds of halo nuclei: the one-neutron halo nuclei, and the so-called Borromean two-neutron halo nuclei. First of all we present a description of the structure of one-neutron systems in chapter 2, and then we use those results for the dynamical description in chapters 3. In the case of one valence neutron, the structure is identified by a a mean field 1D Woods-Saxon potential, where the core occupies the lowest

well-bound states and the one-body halo is identified with a last weakly-bound level.
It is clear that the description of such systems requires an adequate consideration of the role of the continuum. In order to do so we study different methods to deal with continuum in sections 2.1 and 2.2: we select a set of Woods-Saxon potential parameter values that qualitatively model a nuclear structure problem and discretize the system continuum, using a finite set of normalizable (square-integrable) functions (known as pseudostates); three different approaches have been followed. The first one consists in diagonalizing the Woods-Saxon potential Hamiltonian matrix in a truncated Harmonic Oscillator (HO, section 2.2.1) basis; the second makes use of a local scale transformation, applied to the HO basis, to construct a truncated Transformed Harmonic Oscillator (THO, section 2.2.2) basis; the third one uses a rigid wall box (BOX, section 2.1.2) to achieve continuum discretization. Another way to treat continuum, simple in the one-body case, is the determination of the "exact" continuum wavefunction by applying a finite difference method (we used the Numerov method); this results are presented in section 2.1.3.

We present in sections 2.3 and 2.4 results obtained for the one-neutron system: eigenvalues, eigenfunctions, and other quantities of interest (single-particle transition of x and x^2 operators, total strength, and sum rules), studying and comparing the convergence properties of the different approaches. Once the pseudostate description of the model Woods-Saxon potential for the one-body systems has been set up, we proceed to the dynamical part.

We present the exact (section 3.1) and the approximate (sections 3.2 and 3.3) solutions for the scattering of one-particle in the field of two potential wells. We study the influence on the Q-value and the distance of closest approach on the exact solutions in section 3.4, and we present results for different model cases in section 3.5.

In chapter 4 we describe both the structure and dynamics of the Borromean systems. The main ingredients of the Borromean system are the mean field 1D Woods-Saxon potential, with all bound levels supposed to be totally filled by inert core, plus two extra neutrons. The resulting system, unbound at the mean-field level, is bound due the action of a residual point contact density-dependent interaction, which models the pairing interaction.

To specify the two-body problem, in section 4.1 we introduce an appropriate basis and construct bound and excited states by diagonalizing the system Hamiltonian with the different continuum discretization procedures described previously in chapter 2. Besides the discussion on the convergence of eigenvalues and eigenfunctions (section 4.1.1), we compute other quantities of interest as anomalous density and transition intensities of x and x^2 operators in sections 4.1.2 and 4.1.3. Then, these results are compared with those obtained describing the same system (core plus two neutrons) within the "popular" di-neutron cluster model. Once we have the description of the structure of Borromean nuclei, in section 4.2 we develop the scattering process of the two-body system in the field of two potential wells. Finally, we study the influence of the binding energy and pairing interaction in the reaction mechanism (4.2.1 and 4.2.2).

In conclusion, we summarize the main results of this work in chapter 5, where we present some concluding remarks and suggestions of future investigations along the present line of research.

The document ends with some appendixes which complete the discussion. We deepen the study of continuum structure giving a more detailed comparison between HO and THO discretization methods (A), and investigating resonances and virtual states (B). We also give some hints on the non-covariance of Schroedinger equation in non-inertial frame of reference (C), as well as some demonstrations supporting the calculations presented in the thesis (D).

As a last remark we would like to mention that the calculations presented in this thesis have been carried out using FORTRAN90, GNU-Octave, and PERL codes [5] [6].

[5] We have also made use of NAG, ATLAS, LAPACK95, and LAPACK libraries.

[6] In these programs the following values of the relevant physical constants are used: $\hbar c = 197.32858$ MeV·fm, $amu = 938.92635$ MeV/c^2, $\hbar^2/amu = 41.4713768$ MeV^{2}fm^2.

Chapter 2

Bound and unbound states of a particle in a potential well

In this chapter we start considering the problem of a particle moving in a potential well. This can be considered as a toy model for the more realistic problem of a two-body nucleus consisting of a tighly bound core plus one weakly bound nucleon, such as a halo nucleus. We discuss several numerical and approximate methods to obtain the states of this system and the corresponding wave functions in sections 2.1 and 2.2; we then compare them in section 2.3. Moreover, the quality of the description of the excited states is investigated by means of the calculation of several sum rules, which will be introduced in section 2.4.

To study the structure of one particle[1] bound in a potential well, we have to calculate the single-particle eigenvalues and the corresponding wavefunctions. The model potential we use is the one dimensional Woods-Saxon potential[2] $V_{WS}(x)$,

$$V_{WS}(x) = \frac{V_0}{1 + e^{\frac{|x|-R}{\alpha}}} \tag{2.1}$$

with potential parameters chosen for the tests presented in next sections: $V_0 = -50.00$ MeV, $R = 2.00$ fm, $\alpha = 0.40$ fm, and $\mu = 0.975$ amu. This particular set of parameters has been chosen to set up a 1D toy model representative of a light-mass weakly-bound nucleus. With this choice of parameters the system has in fact three single-particle bound states whose energies are presented in figure 2.1, with a weakly-bound third energy level (-0.51 MeV binding energy). A potential like the Woods-Saxon mean field

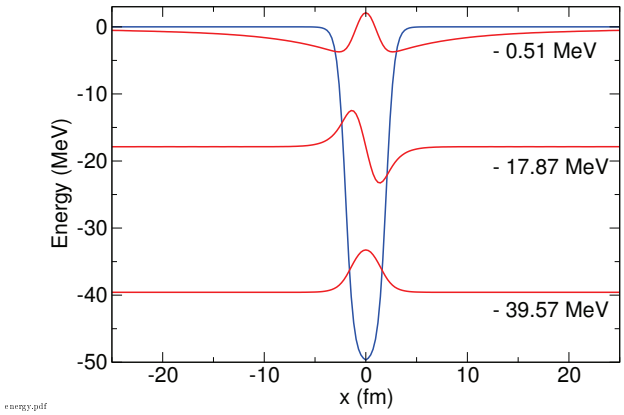

Figure 2.1: The Woods-Saxon 1D potential with the bound states. They have been computed diagonalizing the Hamiltonian in a HO basis with N=50 functions.

of equation (2.1), will give two kinds of results: a set of bound levels with negative energy and a continuum associeted to the positive part of the spectrum. The bound states are square-integrable wavefunctions, which decay

[1] Note that, since we do not simulate Coulomb barriers, we assume the valence particle to be a neutron.

[2] In this thesis only the results obtained with a Woods-Saxon potential are presented, but other potentials have also been tested in order to check the developed computational tools for the resonant states: Woods-Saxon with different parameters and with barriers, Hazi-Taylor, and Ginocchio potentials. See Appendix B.1 for further details.

exponentially to zero. In one dimension, the ground state does not present nodes and is a even function, while the excited states present an increasing number of nodes (e.g. the first excited state has one node and is an odd function, the second excited state has two nodes and is even function, etc.). The continuum functions are asympthotically oscillating to infinity, and for each positive energy, in one dimension, there are two associated functions: one incoming from the left and one from the right. To properly describe the case of a weakly-bound system close to neutron drip-line, it is mandatory to include continuum effects in the system description, therefore our model must include the positive energy part of the spectrum. To treat the continuum consistently we should discretize it by choosing only certain energies and convert this set into square-integrable functions.
To solve this problem we will apply different methods. We can calculate numerically the bound levels energies and wavefunctions by applying a finite-difference method (we employ the so-called Numerov method [45] in section 2.1.1); and we can also construct a discretized continuum spectrum using a large rigid wall box (BOX), as we do in section 2.1.2. Otherwise, we can apply an approximate method as we show in section 2.2: the pseudostate methods in wich continuum wave functions are obtained as eigenstates of the system Hamiltonian matrix in a truncated basis of square-integrable wave functions, such as Harmonic Oscillator (HO, section 2.2.1) and Transformed Harmonic Oscillator (THO, section 2.2.2) bases. In addition, since we use a one dimensional model space, we can also calculate and treat the "exact" continuum wavefunctions and use their combination to build a basis of normalized bin functions, as presented in section 2.1.3.

2.1 Numerical calculation of stationary states

The problem of a neutron moving in a 1D Woods-Saxon mean field can be solved exactly, by direct integration of the 1D time-independent Schroedinger equation (TISE)

$$\hat{H}_{1b}\psi(x) = E\psi(x) \rightarrow \left[-\frac{\hbar^2}{2\mu}\frac{d^2}{dx^2} + V_{WS}(x)\right]\psi(x) = E\psi(x). \tag{2.2}$$

Let us show in the next sections different ways to obtain numerically bound and continuum states.

2.1.1 Bound states: the Numerov method

In this section we follow the solution of the eigenvalue problem of equation (2.2) for the bound levels of Woods-Saxon potential, according to the Numerov method presented in [45].
An acceptable solution $\Psi_E(x)$ of the eigenvalue problem must be a continuous bounded functions of x, conditions that generally occur only for special values of the particle energy E. The eigenvalues are these allowed energies E. For simplicity, by defining $y(x) = \Psi_E(x)$ and $g(x) = 2m\left[E - V_{WS}(x)\right]/\hbar^2$, we can recast the problem as

$$\frac{d^2y}{dx^2} + g(x)y(x) = 0. \tag{2.3}$$

The discrete version of this equation follows by writing $x \to x_n \equiv nh$ and $f(x) \to f(x_n) \equiv f_n$ for any function $f(x)$, where n is an integer and h is the size of the spatial grid. The procedure would be straightforward except for the second derivative, which requires some approximations. If we start with the simple definition of second derivative

$$\Delta^2 f_{n-1} = f(x_n + h) + f(x_n - h) - 2f(x_n), \tag{2.4}$$

and expand the first two terms on the right in a Taylor series, we obtain

$$\Delta^2 f_{n-1} = h^2 f''(x_n) + \frac{h^4}{12} f^{(iv)}(x_n) + O(h^6). \tag{2.5}$$

The simplest approximation $\Delta^2 f_{n-1} \approx h^2 f''(x_n)$ gives the central difference approximation to the second derivative and yields a discrete version of equation (2.3) that is accurate to $O(h^3)$:

$$\Delta^2 y_{n-1} + h^2 g_n y_n = 0. \tag{2.6}$$

The Numerov method improves on this by using the original differential equation for $y(x)$ to write $h^2 f^{(iv)}(x_n) = -h^2(gy)'' \approx -\Delta^2(g_{n-1}y_{n-1})$. This gives the Numerov discretization of equation (2.3)

$$\Delta^2 \left[\left(1 + \frac{h^2}{12} g_{n-1}\right) y_{n-1}\right] + h^2 g_n y_n = 0, \tag{2.7}$$

which is accurate to $O(h^5)$.
Interestingly, the Numerov version is identical to equation (2.6), with the replacements

$$y_n \to \left(1 + \frac{h^2}{12} g_n\right) y_n, \; g_n \to \frac{g_n}{1 + \frac{h^2}{12} g_n}, \tag{2.8}$$

so the Numerov method improved accuracy comes at negligible computational cost. In the following, we will adopt equation (2.6) as the discrete equation of interest, with the assurance that the results apply equally well to the Numerov version after suitably redefining the terms.
If the computational domain corresponds to $N_1 \leq n \leq N_2$, then $-\infty < n < N_1$ and $N_2 < n < \infty$ define the exterior regions. Our task is to find suitable analytic solutions to equation (2.6) in these exterior regions, from which we will infer the proper boundary conditions to be imposed at the limits of the actual (finite) computational interval. Because the exterior regions include the asymptotic realm $n \to \pm\infty$, solutions here can not diverge for large $|n|$ if they're to be physically acceptable.
If we define $\mu_n \equiv \Delta y_n / y_{n+1}$ the logarithmic derivative of $y(x)$, whose derivative is $\Delta\mu_{n-1} = \mu_n - \mu_{n-1}$, equation (2.6) becomes

$$\mu_n^2 + \left(h^2 g_n + \Delta\mu_{n-1}\right)\left(1 - \mu_n\right) = 0. \tag{2.9}$$

Throughout each exterior region, according to our definition, g_n is unchanged from its value at the inner boundary, g_{N_1} or g_{N_2}. But if g_n does not change, then neither does μ_n, so $\Delta\mu_{n-1}$ vanishes identically, and equation (2.9) reduces to a quadratic form that we can solve to give the root pair

$$\mu_n^{\pm} = \frac{1}{2}\left(h^2 g_n \pm \sqrt{h^4 g_n^2 - 4h^2 g_n}\right) \tag{2.10}$$

with the property

$$\left(1 - \mu_n^{+}\right)\left(1 - \mu_n^{-}\right) = 1. \tag{2.11}$$

For $g_n < 0$ (or $h^2 g_n > 4$), both roots of equation (2.10) are real. Because $(1 - \mu_n) y_{n+1} = y_n$, we must select the root that makes $|y_{n+1}| > |y_n|$ over the left exterior region ($-\infty < n < N_1$) and $|y_{n+1}| < |y_n|$ on the right ($N_2 < n < \infty$) to generate solutions that approach zero as $n \to \pm\infty$, i.e. the bound states of the potential. If $0 < h^2 g_n < 4$, then $\mu_n^{\pm}$ are complex conjugates, and equation (2.11) implies $|1 - \mu_n^{\pm}| = 1$. It follows that the

exterior solutions have constant modulus, $|y_{n+1}| = |y_n|$, and are oscillatory; these solutions correspond to the continuum.
Now, we select[3] different values of negative energy E and construct the corresponding stationary state $y(x) = \Psi_E(x)$, following this algorithm:

- If $g_{N_1} < 0$, take $y_{N_1+1} = (1-\mu_{N_1})^{-1} y_{N_1}$ and calculate y_{N_1+2}, y_{N_1+3}, ... recursively from equation (2.6). Calculate μ_{N_1} as the root of equation (2.10) for which $|1 - \mu_{N_1}| < 1$.

- If $g_{N_2} < 0$, take $y_{N_2-1} = (1 - \mu_{N_2-1}) y_{N_2}$ and calculate y_{N_2-2}, y_{N_2-3}, ... recursively from equation (2.6). With g assumed constant in the right exterior region, μ_{N_2-1} is indistinguishable from μ_{N_2} and can be found from equation (2.10) as the root for which $|1 - \mu_{N_2}| > 1$.

If $g_{N_2} > 0$, the solution corresponds to a continuum wave and we should follow a different prescription (see section 2.1.3).

In all cases, the values for y_{N_1} and y_{N_2} are arbitrary, reflecting an overall choice of normalization, and we can set them equal to unity. If the two steps both apply, the recursive solutions we obtain must be joined at some intermediate point[4], say, $n = M$. We first match the slopes at y_M by adjusting the start value y_{N_2}. Then, whenever the corresponding energy E of the wavefunction under study is an eigenvalue, both recursions will also give identical values for y_M. Otherwise, the solution is discontinuous at y_M and physically unacceptable. We can find slopes at y_M accurate to $O(h^3)$ using the centered difference

$$y(x_M + h) - y(x_M - h) = 2hy'(x_M) + O(h^3). \tag{2.12}$$

However, the Numerov implementation is more demanding and requires two steps to calculate the slopes $y'(x_M)$ to the desired accuracy:

$$y(x_M+h) - y(x_M-h) - \frac{1}{8}y(x_M+2h) + \frac{1}{8}y(x_M-2h) = \frac{3}{2}hy'(x_M) + O(h^5). \tag{2.13}$$

At the end of this calculation we obtain a set of bound state wavefunctions $\Psi_E(x)$ with the corresponding energies E.

[3] To choose the energy values we should care to fix a small energy interval not to loose precision. For our calculations we used a $\Delta E = 0.4MeV$.

[4] The matching point x_M should not be close to the possible nodes of the wavefunctions, but on their tails.

2.1.2 Bound and unbound states: Woods-Saxon in a BOX

A procedure to authomatically calculate bound and continuum square-integrable discretized states is the so-called BOX method, which consists in confining the system in a box defined by a radius x_b

$$V_b(x) = \begin{cases} V_{WS} & if\ |x| < x_b, \\ \infty & if\ |x| \geq x_b. \end{cases} \tag{2.14}$$

With x_b chosen large enough compared to the potential range. This problem can be solved using standard numerical techniques for the solution of differential equations, as for example the Numerov approach we have just shown in section 2.1.1. Once the 1D TISE for the mean field Woods-Saxon potential (2.1) is solved, we obtain the eigenenergies E_i^{BOX} and the corresponding eigenfunctions $\psi_i^{BOX}(x)$.

2.1.3 Unbound states: the "exact" continuum

In a one-body problem it is rather easy to construct "exact" continuum states. Let us consider, therefore, the problem of the scattering in a Woods-Saxon symmetric 1D potential $V(X)$ (2.1). We divide the real axes in two asymptotic regions labeled (I) and (III) and the potential region (II), as shown schematically in figure 2.2.

The continuum wave functions are those solutions of the Schroedinger

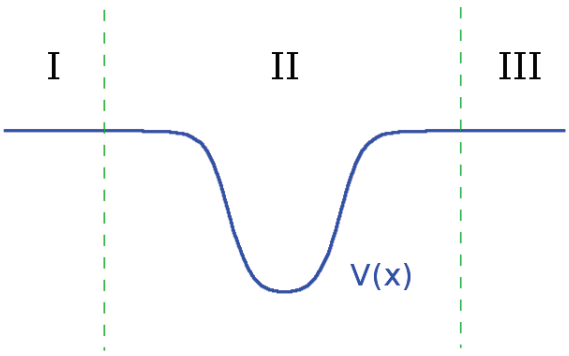

Figure 2.2: A potential V(x) divided in three regions, the one above the potential (II) and the asymptotic regions (I and III).

equation (3.4) with positive energy ($E > 0$). In this case all energies are allowed and levels are doubly degenerate. We compute the "exact" wave-function for a chosen mesh of continuum energies, each one corresponding to two degenerate solutions. A possible choice for these degenerate solutions are the scattering states calculated as an incident plane wave coming either from the right (region I) or from the left (region III) of the well. In the asymptotic region the solutions are

$$\phi_{\pm k}(x) = \frac{e^{\pm ikx}}{\sqrt{2\pi}}. \tag{2.15}$$

These continuum waves $\phi_k(x)$ are momentum–normalized, thus

$$\langle \phi_k | \phi_{k'} \rangle = \frac{1}{2\pi} \int_{-\infty}^{+\infty} e^{ix(k-k')} dx = \delta(k - k'). \tag{2.16}$$

Since $p = \hbar k$ and $E = \dfrac{\hbar^2 k^2}{2\mu}$ we can define also energy normalized states

$$\langle \phi_k(E) | \phi_{k'}(E') \rangle = \delta(E - E') \tag{2.17}$$

and

$$\phi_{\pm k}(E) = \left(\frac{m}{2\pi\hbar^2 |k|} \right)^{1/2} e^{\pm ikx}. \tag{2.18}$$

The left incoming wave will have the asymptotic behaviors

$$\phi_k^I(x) = \frac{1}{\sqrt{2\pi}} \left(e^{ikx} + re^{-ikx} \right) \qquad \rightarrow \ incident \ + \ reflected \tag{2.19a}$$

$$\phi_k^{III}(x) = \frac{1}{\sqrt{2\pi}} te^{ikx} \qquad \rightarrow \ transmitted \tag{2.19b}$$

where, in general, $t, r \in \mathbb{C}$ and $|t|^2 + |r|^2 = 1$.
We define α_k as the logarithmic derivative of the numerical solution $\phi_k(x)$ with initial conditions (2.19)

$$\alpha = \frac{\phi'(x_m)}{\phi(x_m)} \tag{2.20}$$

and A as a complex normalization constant

$$A\phi_k(x_m) = \frac{1}{\sqrt{2\pi}} \left(e^{ikx_m} + re^{-ikx_m} \right) \quad and \quad A\phi(x_M) = \frac{1}{\sqrt{2\pi}} te^{ikx_M} \tag{2.21}$$

where x_m and x_M are the minimum and maximum x values. Using equations (2.20) and (2.21) we obtain

$$r = \frac{1 + i\frac{\alpha}{k}}{1 - i\frac{\alpha}{k}} e^{2ikx_m}, \tag{2.22a}$$

$$A = \frac{1}{\sqrt{2\pi}} \frac{1}{\phi(x_m)} \left(e^{ikx_m} + re^{-ikx_m} \right), \tag{2.22b}$$

$$t = \sqrt{2\pi} A \phi(x_M) e^{-ikx_M}. \tag{2.22c}$$

The degenerate partner is obtained imposing the asymptotic behavior

$$\phi^I_{-k}(x) = \frac{1}{\sqrt{2\pi}} t e^{-ikx}, \tag{2.23a}$$

$$\phi^{III}_{-k}(x) = \frac{1}{\sqrt{2\pi}} \left(e^{-ikx} + re^{ikx} \right), \tag{2.23b}$$

and in this case

$$r = \frac{1 - i\frac{\alpha}{k}}{1 + i\frac{\alpha}{k}} e^{-2ikx_m}, \tag{2.24a}$$

$$A = \frac{1}{\sqrt{2\pi}} \frac{1}{\phi(x_M)} \left(e^{-ikx_M} + re^{ikx_M} \right), \tag{2.24b}$$

$$t = \sqrt{2\pi} A \phi(x_m) e^{ikx_m}. \tag{2.24c}$$

Now we consider as independent degenerate solutions at a given momentum the symmetric and antisymmetric combinations

$$\phi^s_{\pm k}(x) = \frac{1}{\sqrt{2\pi}} \left[\phi_{+k}(x) + \phi_{-k}(x) \right] \tag{2.25a}$$

$$\phi^a_{\pm k}(x) = \frac{1}{\sqrt{2\pi}} \left[\phi_{+k}(x) - \phi_{-k}(x) \right] \tag{2.25b}$$

such that

$$\langle \phi^\Gamma_k | \phi^{\Gamma'}_{k'} \rangle = \delta_{\Gamma\Gamma'} \delta(k - k'), \tag{2.26}$$

where $\Gamma = s, a$, and the solutions are still momentum-normalized. So, for each momentum $k = \sqrt{\frac{2\mu|E|}{\hbar^2}}$ we obtain a set of exact wavefunctions for the continuum

$$\varphi(k, x) = \phi^s_{\pm k}(x) + \phi^a_{\pm k}(x). \tag{2.27}$$

2.2 Approximate description of stationary states

As we have mentioned at the beginning of this chapter, to deal with weakly-bound systems it is mandatory to include the continuum. The positive part of the spectrum is represented by a continuous of solutions, whose associated wave functions are oscillatory at large distances, reflecting the unbound character of these states. Consequently, these functions are not square-integrable. These properties make these functions unsuitable for some applications, such as the study of dynamics with coupled-channels calculation. In these situations, it is convenient to resort to an approximate description of the continuum in terms of a finite set of square-integrable functions, usually referred to as pseudostates (PS).
We can construct a set of PS by diagonalizing the Hamiltonian

$$\mathcal{H}_{1b} = \left[-\frac{\hbar^2}{2\mu}\frac{d^2}{dx^2} + V_{WS}(x) \right] \tag{2.28}$$

in a chosen basis of normalizable functions. The negative eigenvalues obtained upon diagonalization represent the bound states of the systems, whereas the positive ones can be regarded as a discrete representation of the continuum spectrum. The pseudostates will have an oscillatory trend up to a certain spatial region in which they asympthotically decay at zero. They will also be associated to certain positive energies, therefore we will not treat anymore with a continuum, but with a discrete set of functions.
As the number of basis functions grows, the density of PS's increases and their corresponding wavefunctions extend to larger distances, thus recovering the structure of the continuum. So, from a computational point of view, we should take care of defining a proper spatial range which includes the whole potential region, and of including an adequate number of basis states in order to obtain the convergence of the main feature of the system (such as energy of bound levels and sum rules for electric transitions between bound and continuum states).

In the next sections we present the different bases considered here for continuum discretization.
We will compare the results of these methods, also with the other calculation previously presented, in sections 2.3 and 2.4. In addition, in appendix A we study a more detailed comparison between the two pseudostates approaches.

2.2.1 The pseudostates method with a Harmonic Oscillator basis

The most popular approach in Quantum Mechanics to construct a basis of pseudostates is provided by the Harmonic Oscillator [46]. To solve the TISE (2.2) in a 1D HO basis, the starting point is to generate a truncated N dimensional basis set of 1D HO wave functions

$$\phi_i^{HO}(x) = M_i\sqrt{a}H_i(ax)e^{-a^2x^2/2}; \quad i = 0, \ \ldots, \ N-1. \tag{2.29}$$

The parameter

$$a = \sqrt[4]{\frac{\mu K}{\hbar^2}} \tag{2.30}$$

is the inverse of the oscillator length, with K equal to the force constant of the Harmonic Oscillator. The inverse oscillator length determination is described in appendix D.1. $H_i(ax)$ is the i-th Hermite polynomial, and M_i is a normalization constant

$$M_i = \frac{1}{\sqrt{2^i i!\sqrt{\pi}}}. \tag{2.31}$$

The HO basis can be easily constructed and the necessary integral calculations are simplified making use of the Hermite polynomial recurrence relation [47].

$$\begin{aligned}
\frac{d}{dx}H_n(x) &= 2nH_{n-1}(x) \ , \\
H_{n+1}(x) &= 2xH_n(x) - 2nH_{n-1}(x) \ , \\
xH_j(x) &= \frac{1}{2}H_{j+1}(x) + jH_{j-1}(x) \ , \\
x^2H_j(x) &= \frac{1}{4}H_{j+2}(x) + \frac{2j+1}{2}H_j(x) + j(j-1)H_{j-2}(x).
\end{aligned} \tag{2.32}$$

The resulting basis is

$$\begin{aligned}
\phi_0^{HO}(x) &= \sqrt{\frac{a}{\sqrt{\pi}}} e^{(-a^2x^2/2)} \ , \\
\phi_1^{HO}(x) &= \sqrt{\frac{a}{2\sqrt{\pi}}} (2ax) e^{(-a^2x^2/2)} \ , \\
&\dots \\
\phi_n^{HO}(x) &= \sqrt{\frac{a}{2^n n! \sqrt{\pi}}} \frac{1}{\sqrt{2}} H_n(ax) e^{(-a^2x^2/2)} \ , \\
\phi_{n+1}^{HO}(x) &= \sqrt{\frac{a}{2^{n+1}(n+1)!\sqrt{\pi}}} [2ax H_n(ax) - 2n H_{n-1}(ax)] e^{(-a^2x^2/2)} \ , \\
&\dots \\
\phi_k^{HO}(x) &= \sqrt{\frac{2}{k}}\, a\, x\, \phi_{k-1}^{HO}(ax) - \sqrt{\frac{k-1}{k}} \phi_{k-2}^{HO}(ax). \qquad (2.33)
\end{aligned}$$

The 1D TISE for Harmonic Oscillator states is

$$\left[-\frac{\hbar^2}{2\mu} \frac{d}{dx^2} + V_{HO}(x) \right] \phi_n^{HO}(x) = \hbar\omega (n + \frac{1}{2}) \phi_n^{HO}(x), \qquad (2.34)$$

where a is the inverse oscillator length (2.30) and

$$V_{HO}(x) = \frac{1}{2} K x^2, \qquad (2.35)$$

$$\hbar\omega = \hbar \sqrt{\frac{K}{\mu}} = \frac{\hbar^2 a^2}{\mu}. \qquad (2.36)$$

In order to obtain solutions of equation (2.28) for V_{WS} (2.1) the first step is to compute the matrix elements of the kinetic energy in the HO basis. This part is common to any potential.

$$\begin{aligned}
\langle \phi_i^{HO} | \hat{T} | \phi_j^{HO} \rangle &= -\frac{\hbar^2}{2\mu} a N_i N_j \int_{-\infty}^{+\infty} dx\, e^{(-a^2x^2/2)} H_i(ax) \frac{d^2}{dx^2} H_j(ax) e^{(-a^2x^2/2)} \\
&= -\frac{\hbar^2}{2\mu} a^2 N_i N_j \int_{-\infty}^{+\infty} dy\, e^{(-y^2/2)} H_i(y) \frac{d^2}{dy^2} H_j(y) e^{(-y^2/2)},
\end{aligned}$$

with $y = ax$.

Making use of the relations (2.32)

$$\frac{d^2}{dy^2} H_j(y) e^{(-y^2/2)} = \left[\frac{1}{4} H_{j+2}(y) + j(j-1) H_{j-2}(y) - \frac{2j+1}{2} H_j(y) \right] e^{(-y^2/2)}.$$

Inserting this expression in the integral and taking into account the orthogonality properties of the Hermite polynomials, one gets:

$$\begin{aligned}\langle\phi_i^{HO}|\hat{T}|\phi_j^{HO}\rangle = &-\frac{\hbar^2}{2\mu}a^2\frac{\sqrt{(j+1)(j+2)}}{2}\,\delta_{i,j+2}\\ &-\frac{\hbar^2}{2\mu}a^2\frac{\sqrt{j(j-1)}}{2}\,\delta_{i,j-2}\\ &+\frac{\hbar^2}{2\mu}a^2\frac{2j+1}{2}\,\delta_{i,j}.\end{aligned}$$

Note that an identical result is obtained taking into account that $\hat{T} = \hat{H} - \hat{V}_{HO}$ and thus $\langle\phi_i^{HO}|\hat{T}|\phi_j^{HO}\rangle = \left(j+\frac{1}{2}\right)\frac{\hbar^2a^2}{\mu}\,\delta_{i,j} - \frac{K}{2}\langle i|x^2|j\rangle$.

The second step is the calculation of the potential matrix elements in the HO basis

$$\langle\phi_i^{HO}|\hat{V}|\phi_j^{HO}\rangle = \int_{-\infty}^{+\infty} dx\ \phi_i^{(HO)*}\ V_{WS}\ \phi_j^{(HO)}. \tag{2.37}$$

Due to symmetry reasons $\langle\phi_i^{HO}|\hat{V}|\phi_j^{HO}\rangle = 0$ if the basis wave functions have opposite parity (symmetric or antisymmetric).

Once the matrix is diagonalized, we obtain a set of one-body eigenvalues, E_i^{HO}, and eigenfunctions, $\psi_i^{HO}(x)$. The eigenstates are linear combinations of the basis elements

$$\psi_i^{HO}(x) = \sum_{k=0}^{N-1}\alpha_{ik}^{HO}\phi_k^{HO}(x);\quad i = 0,\ \ldots,\ N-1. \tag{2.38}$$

2.2.2 The pseudostates method with a Transformed Harmonic Oscillator basis

A disadvantage of the HO basis when used as a basis in variational methods to model bound states is the Gaussian asymptotic behavior, compared to the exponential behavior of the bound states of a finite potential. This can be avoided only using a huge number of basis states, thus increasing the computational power required. This fact explains the success of the THO basis.

A Transformed HO (THO) basis consists of a HO basis to which a local scale transformation (LST) $s(x)$ has been applied. The aim of this transformation is to correct the HO wave functions asymptotic behavior. See, e. g., references

[48–50].
To solve the problem in a 1D THO basis the starting point is a truncated N dimensional basis set $\phi_i^{HO}(x)$ of 1D HO wave functions (see section 2.2.1), which has to be transformed into the new basis as follows

$$\phi_i^{THO}(x) = \sqrt{\frac{ds(x)}{dx}}\ \phi_i^{HO}(s(x))\ i = 0, \ldots, N-1\ , \tag{2.39}$$

according to the analytical LST function (see [50, 51])

$$s(x) = (x^{-m} + (\gamma\sqrt{x})^{-m})^{-\frac{1}{m}} \tag{2.40}$$

that is valid for $x > 0$; for negative x values we impose that $s(x)$ is an odd function: $s(-x) = -s(x)$. The quantity γ is an adjustable parameter of the LST, b is the oscillator length determined using the algorithm presented in appendix D.1, and the power m, according to [49], is set to $m = 4$, although the results depend very weakly on this parameter.

The matrix elements of the kinetic energy operator in this THO basis can be computed as

$$\langle\phi_i^{THO}|\hat{T}|\phi_j^{THO}\rangle = -\frac{\hbar^2}{2\mu}\ \int_{-\infty}^{+\infty} dx\ \sqrt{s'(x)}\ \phi_i^{HO}[s(x)]\ \frac{d^2}{dx^2}\sqrt{s'(x)}\ \phi_j^{HO}[s(x)]. \tag{2.41}$$

Making use of the relations

$$s'(x) = \frac{ds(x)}{dx} = \frac{s(x)}{2x}\ \left[1 + \left(\frac{s(x)}{x}\right)^m\right], \tag{2.42}$$

and

$$s''(x) = \frac{d^2s(x)}{dx^2} = -\frac{s(x)}{4x}\ \frac{x^{\frac{m}{2}-1}}{\gamma^m + x^{\frac{m}{2}}}\ \left[1 + (m+1)\left(\frac{s(x)}{x}\right)^m\right], \tag{2.43}$$

it can be finally evaluated as

$$\begin{aligned}
\langle\phi_i^{THO}|\hat{T}|\phi_j^{THO}\rangle = \\
\frac{1}{4}\frac{\hbar^2}{2\mu}\int_{-\infty}^{+\infty} dx\ s''(x)^2\ \left(s'(x)\right)^{-1}\ \phi_i^{HO}(s(x))\phi_j^{HO}(s(x)) \\
+\frac{1}{2}\frac{\hbar^2}{2\mu}a\int_{-\infty}^{+\infty} dx\ s''(x)\ s'(x)\ \phi_i^{HO}(s(x))\ \left[\sqrt{\frac{j}{2}}\phi_{j-1}^{HO}(s(x)) - \sqrt{\frac{j+1}{2}}\phi_{j+1}^{HO}(s(x))\right] \\
+\frac{1}{2}\frac{\hbar^2}{2\mu}a\int_{-\infty}^{+\infty} dx\ s''(x)\ s'(x)\ \phi_j^{HO}(s(x))\ \left[\sqrt{\frac{i}{2}}\phi_{i-1}^{HO}(s(x)) - \sqrt{\frac{i+1}{2}}\phi_{i+1}^{HO}(s(x))\right] \\
+\frac{\hbar^2}{2\mu}a^2\int_{-\infty}^{+\infty} dx\ s'(x)^3\ \left[\sqrt{\frac{i}{2}}\phi_{i-1}^{HO}(s(x)) - \sqrt{\frac{i+1}{2}}\phi_{i+1}^{HO}(s(x))\right] \\
+\frac{\hbar^2}{2\mu}a^2\int_{-\infty}^{+\infty} dx\ s'(x)^3\ \left[\sqrt{\frac{j}{2}}\phi_{j-1}^{HO}(s(x)) - \sqrt{\frac{j+1}{2}}\phi_{j+1}^{HO}(s(x))\right],
\end{aligned}$$

where, following the notation of the previous subsection, $a = b^{-1}$ is the inverse oscillator length. The second step is the calculation of the potential matrix elements $\langle\phi_i^{THO}|\hat{V}|\phi_j^{THO}\rangle$.
Once the TISE for the 1D mean field Woods–Saxon potential (2.1) is solved using the basis (2.39), we obtain a set of discrete eigenvalues $E_i^{(THO)}$ and eigenfunctions $\psi_i^{(THO)}(x)$ that can be written as a linear combinations of the THO basis states

$$\psi_i^{THO}(x) = \sum_{k=0}^{N-1} \alpha_{ik}^{THO}\phi_k^{THO}(x);\quad i = 0,\ \ldots,\ N-1. \tag{2.44}$$

2.3 Convergence of eigenvalues and eigenfunctions

We now show the results obtained by applying the methods explained in the previous sections. In particular we study the convergence of bound states energies and the behaviour of the wavefunctions.
The obtained results of the differernt methods depend on the basis dimension for HO and THO methods, and on the box radius x_b for the BOX method. We proceed to study the convergence of eigenvalues and eigenfunctions when these parameters are varied. We focus not only on the energies, but also on the wavefunctions, paying particular attention to their asymptotic behavior.

A proper description of the wave functions at large distances, well beyond the range of the potential, is, in fact, crucial to reasonably describe the reaction properties of our system. This is even more important when, as in our chosen specific case, the Woods-Saxon potential has a very weakly-bound state ($E_2 = -0.51$ MeV), as shown in figure 2.3. In the HO case the

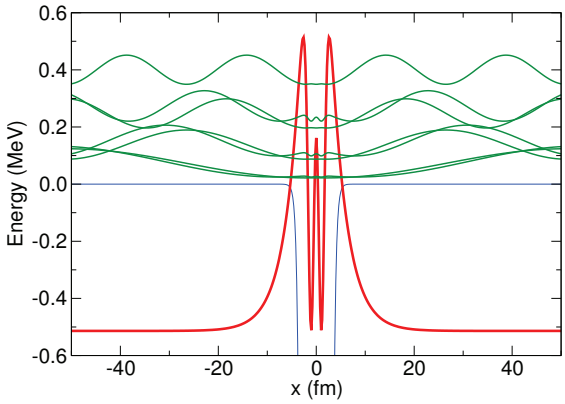

Figure 2.3: The Woods-Saxon model potential (thin blue), the square of the least bound state wave function (thick red) and the first squared continuum PSs (green) obtained with the Hamiltonian matrix diagonalization (in particular BOX with $x_b = 100$ fm).

key parameter is the basis dimension N; so we check the results convergence with a varying basis size. In addition to the value of N, a second model parameter is the inverse oscillator length a. The inverse oscillator length determines the curvature of the HO potential at the origin and thus how wide the potential is (see appendix D.1).
In the THO case the results depend mainly on the basis dimension N and the ratio γ/b, where $b = 1/a$ is the oscillator length. The ratio $\gamma/b = \left(\frac{8\mu\varepsilon}{\hbar^2}\right)^{1/4}$ gives an extra degree of freedom compared to the HO case. As discussed in [48, 50], the value of $\frac{\gamma^2}{2b^2}$ can be considered as an effective momentum value, k_{eff}, and the asymptotic value of the basis functions is $e^{-\frac{\gamma^2}{2b^2}|x|}$. As γ/b increases (decreases) the basis spatial extension decreases (increases). Also, this ratio dictates the density of PS's as a function of the excitation energy. For small values of γ/b, the positive eigenvalues tend to concentrate at lower energies. This useful property of THO basis makes this approach an appealing alternative to HO [50]. For large γ/b values the THO reaches the HO limit. The improved asymptotic wavefunction behavior is ascertained

computing the bound states energy convergence. If we fix the value of 5 keV as the energy convergence goal, a basis with $N = 50$ functions is needed for $\gamma/b = 2.4$ fm$^{-1/2}$ (as in the HO case) while it is enough with $N = 20$ for $\gamma/b = 1.2$ fm$^{-1/2}$. All THO results have been calculated for $\gamma/b = 1.2$ fm$^{-1/2}$.
The third option considered for obtaining pseudostates is enclosing the system in a rigid wall box (see section 2.1.2). The main parameter in this case is the box width, x_b.

In the left panels of figure 2.4 we depict the eigenvalues of the adopted Woods-Saxon potential as a function of the basis dimension N or the box radius x_b, depending on the method. Negative energy levels converge to the bound state energies quite fast. We consider that an energy level is converged when $\Delta E \leq 5$ keV for a dimension increment $\Delta N = 10$. As expected, the convergence is much faster for the ground and first excited states than for the weakly-bound second excited state.

In the right panels of figure 2.4 we show for different parameter values the weakly-bound state wave function tails, where the major differences can be found. Large N values (in HO and THO cases) are required to extend towards large x values, reproducing the exponential behaviour. Note that the THO approach leads to a faster convergence than the original HO approach. For the BOX case we show the wave function tail for different box sizes.

As an example, we show the convergence of the bound level energy with a small number of basis states in figure 2.5. In this example we used the HO calculation applied to a Woods-Saxon potential 2.1 of parameters $V_0 = -2.5$ MeV, $R = 3.0$ fm, $\alpha = 0.6$ fm, and a reduced mass of $\mu = 0.975$ amu.

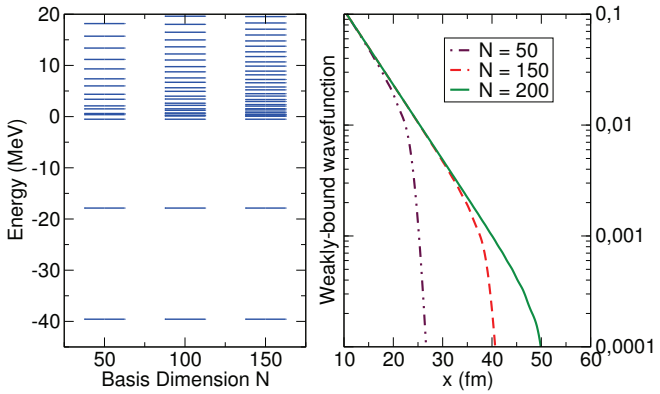

(a) HO

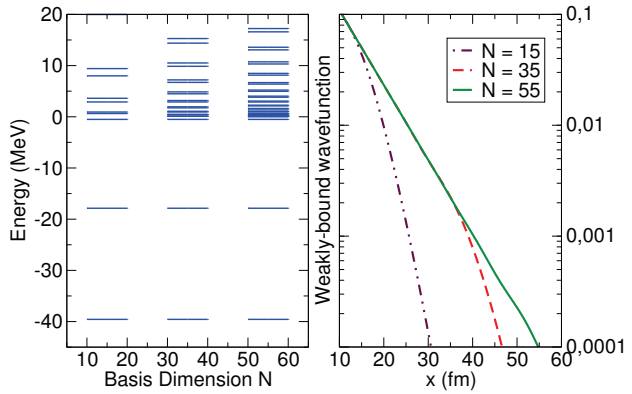

(b) THO

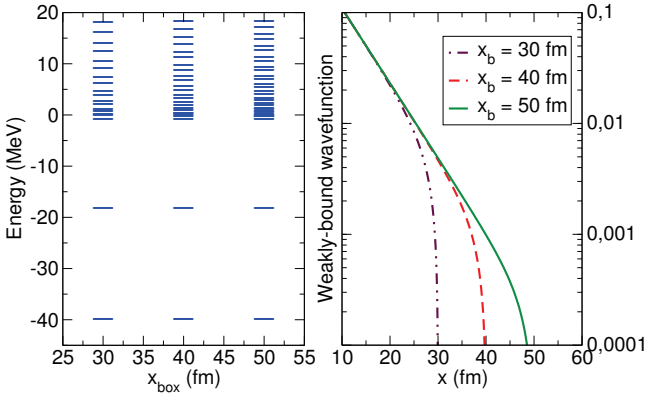

(c) BOX

Figure 2.4: Left panels: Eigenvalues of the Woods-Saxon model potential as a function of the number of basis states (in the HO and THO case) and as a function of the box radius (in the BOX case). Right panels: asymptotic spatial dependence of the weakly-bound state wave function (in logarithmic scale) as a function of x for different parameters values.

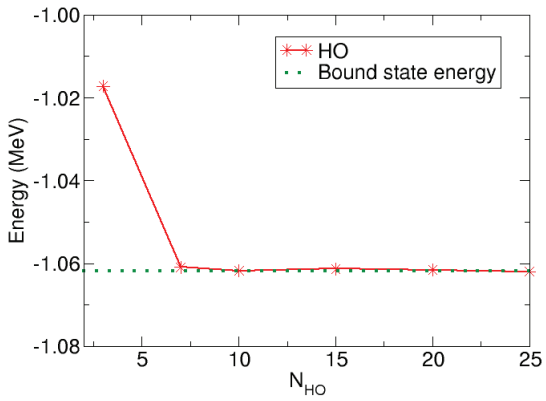

Figure 2.5: Example of the convergence of the bound energy for a HO calculation (red starred line), including a small numebr of basis states N_{HO}. The value of the bound state energy for this case is indicated by the green dotted line. This calculation has been made with a potential 2.1 of parameters $V_0 = -2.5$ MeV, $R = 3.0$ fm, $\alpha = 0.6$ fm, and a reduced mass of $\mu = 0.975$ amu.

2.4 Matrix elements between ground state and continuum states

In this section we present results for the transition probabilities for the x and x^2 operators from a bound state to excited states at positive energies. To enhance the value of this matrix element, we choose the least bound state of our Woods-Saxon well. These are the 1D equivalent of the dipole and quadrupole transition strengths to the continuum in 3D. As it is well known, the low binding energy of weakly-bound systems strongly affects the response to the continuum and, therefore, the convergence of these matrix elements is a crucial test for the discretization procedures.

The transition probability between bound states or between a bound state and a continuum pseudostate (see the discussion in [52]) can be written as

$$B_n(b \to i) = |\langle \Psi_b | \mathcal{O}_n(x) | \Psi_i \rangle|^2. \tag{2.45}$$

with $\mathcal{O}_n(x) = x$ and x^2 for n= 1 and 2, respectively. Therefore we need to

compute the integrals

$$\langle \Psi_b | \mathcal{O}_n(x) | \Psi_i \rangle = \int_{-\infty}^{+\infty} dx \Psi_b^*(x) \mathcal{O}_n(x) \Psi_i(x). \tag{2.46}$$

By changing the parameters N or x_b we expect a difference in the density of continuum levels (as previously shown in the left panels of figure 2.4). For example, in figure 2.6 we present the different distributions of B_1 intensities obtained with the THO procedure for N = 35 and N = 85, where this effect can be clearly appreciated.

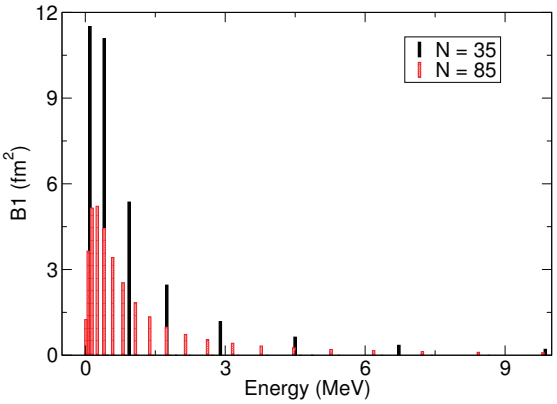

Figure 2.6: B_1 transition intensities calculated for the first excited ($b = 2$) of the Woods-Saxon potential of Figure 2.1, using a THO basis with N=35 (dark bars) and N = 85 (red light bars).

The B_1 and B_2 distributions for HO, THO, and BOX cases are shown in figure 2.7 for the calculations starting from the weakly-bound second excited state $\Psi_2(x)$. For a better comparison of the convergence properties, in the last row of panels of figure 2.7 we also display the summed $Tot(B_1)_{2\to i} = \sum_{i=1}^{N} \mid \langle \Psi_2 | x | \Psi_i \rangle \mid^2$ and $Tot(B_2)_{2\to i} = \sum_{i=1}^{N} \mid \langle \Psi_2 | x^2 | \Psi_i \rangle \mid^2$ transition intensities as a function of the excitation energy. These should be calculated including in the $\{\Psi_i\}$ set only those states above the initial state Ψ_2, i.e. only the continuum states in our case. However, in the calculation of the summed strength we have included also the transition to lower energy bound states, which in principle are occupied by the core particles and thus Pauli forbidden. In this way we can compare the results with the sum rules, that encompass all the states.

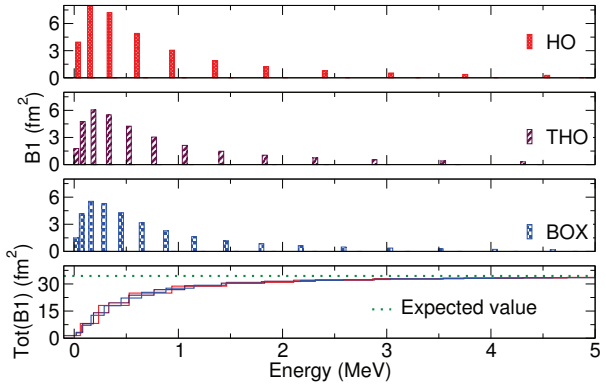

(a) B1

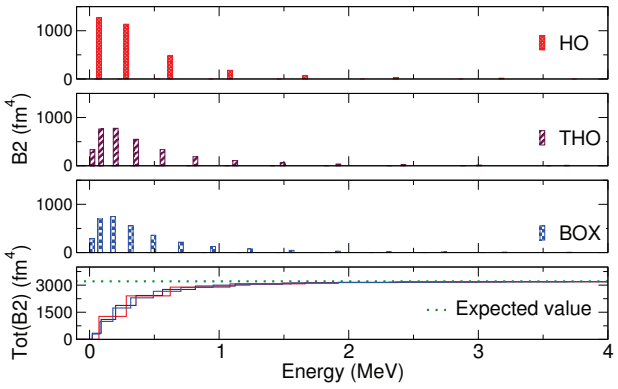

(b) B2

Figure 2.7: B_1 (upper four panels) and B_2 (lower four panels) energy distributions calculated starting from the third bound state with the HO, THO and BOX methods (using $N_{HO} = 250$, $N_{THO} = 85$, and $x_b = 100$ fm). In the last rows the cumulative strengths ($Tot(B_1)$ and $Tot(B_2)$) for each case are shown as a function of the excitation energy and compared to the sum rule expected value (green dotted lines).

For our one-body problem, the Total Strength Sum Rule (TSSR) for a operator $\mathcal{O}$ is

$$\mathcal{S}_T^{(b)}(\mathcal{O}, N) = \sum_{i=0}^{N-1} \mid \langle \Psi_b | \mathcal{O}(x) | \Psi_i \rangle \mid^2, \tag{2.47}$$

where $|\Psi_b\rangle$ is the bound state wave function ($|\Psi_2\rangle$ in our case) and $\{|\Psi_i\rangle\}_{i=1}^N$ is the set of bound states plus pseudostates. This quantity can be written in closed-form, making use of the completeness of the basis. This yields

$$\lim_{N\to\infty} \mathcal{S}_T^{(b)}(\mathcal{O}, N) = \langle \Psi_b | \mathcal{O}^2(x) | \Psi_b \rangle \tag{2.48}$$

and can be easily calculated numerically from the bound state wave functions. These values are depicted in figure 2.7 as green horizontal dotted lines and, as one can see, we find a good agreement for all discretization procedures.

Another useful quantity to assess the goodness of a continuum discretization is the Energy Weighted Sum Rule (EWSR)

$$\mathcal{E}_W^{(b)}(\mathcal{O}, N) = \sum_{i=0}^{N-1} (E_i - E_b) \mid \langle \Psi_b | \mathcal{O}(x) | \Psi_i \rangle \mid^2, \tag{2.49}$$

where, again, $|\Psi_b\rangle$ is the bound state wave function and $\{|\Psi_i\rangle\}_{i=1}^N$ is the set of bound states plus pseudostates. The EWSR can be also written in closed-form, making use again of the completeness of the intermediate states. This gives

$$\lim_{N\to\infty} \mathcal{E}_W^{(b)}(\mathcal{O}_n, N) = \frac{1}{2}\frac{\hbar^2}{\mu} \langle \Psi_b | \left(\frac{d\mathcal{O}_n(x)}{dx} \right)^2 | \Psi_b \rangle. \tag{2.50}$$

Thus in the case of $\mathcal{O}_1 = x$, as demonstrated in appendix D.2, it results

$$\mathcal{E}_W^{(b)}(x, N \to \infty) = \frac{1}{2}\frac{\hbar^2}{\mu}, \tag{2.51}$$

while for $\mathcal{O}_2 = x^2$

$$\mathcal{E}_W^{(b)}(x^2, N \to \infty) = 2\frac{\hbar^2}{\mu} \langle \Psi_b | x^2 | \Psi_b \rangle. \tag{2.52}$$

These values are compared in table 2.1 with those calculated for different values of N for the HO and THO discretization procedures and in table 2.2 for different values of x_b for the BOX procedure, summing the contributions

of the different pseudostates. As one can see from the convergence of the different sum rules, smaller N values are required in the THO than in the HO case. In the BOX case a rather large value of x_b is necessary.

	HO			THO	
N	TSSR (fm^2)	EWSR ($\frac{\hbar^2}{\mu}$)	N	TSSR (fm^2)	EWSR ($\frac{\hbar^2}{\mu}$)
15	16.26	0.500	8	15.34	0.508
100	34.38	0.500	20	33.43	0.500
150	34.44	0.499	35	34.42	0.500
200	34.44	0.500	55	34.44	0.500
250	34.44	0.500	85	34.44	0.500
	34.44	**0.500**		**34.44**	**0.500**

(a) B_1

	HO			THO	
N	TSSR (fm^4)	EWSR ($\frac{\hbar^2}{\mu}$)	N	TSSR (fm^4)	EWSR ($\frac{\hbar^2}{\mu}$)
15	242.7	31.59	8	200.3	-1.592
100	3137	68.80	20	2576	72.11
150	3205	68.89	35	3187	68.85
200	3212	68.90	55	3212	68.95
250	3213	68.91	85	3212	68.91
	3213	**68.91**		**3213**	**68.91**

(b) B_2

Table 2.1: The $B_1(\mathcal{O} = x)$ (a) and $B_2(\mathcal{O} = x^2)$ (b) expected sum rules values in bold are compared with those calculated for different values of N for the HO and THO bases summing the contributions of the different pseudostates.

As it is apparent from figure 2.7 the distribution of transition matrix elements to continuum states follows the expected threshold shape of the multipole strength for weakly-bound systems.

We can provide a comparison of excitation matrix elements results presented in panel a of figure 2.7 with an "exact" calculation.
As we have seen in the previous section, for each positive energy there are two degenerate continuum wave functions with momentum $k = \pm\sqrt{\frac{2\mu E}{\hbar^2}}$, one of them corresponding to a wave incident from the left, and the other to a

	B1		B2	
x_b	TSSR	EWSR	TSSR	EWSR
(fm)	(fm^2)	($\frac{\hbar^2}{\mu}$)	(fm^4)	($\frac{\hbar^2}{\mu}$)
15.00	23.61	0.499	733.3	67.23
35.00	34.18	0.500	2990	68.37
55.00	34.45	0.500	3211	68.91
85.00	34.45	0.499	3214	68.90
100.0	34.44	0.499	3213	68.90
	34.44	**0.500**	**3213**	**68.91**

Table 2.2: The $B_1(\mathcal{O} = x)$ (left) and $B_2(\mathcal{O} = x^2)$ (right) "exact" sum rules values in bold are compared with those calculated for different values of x_b for the BOX procedure, summing the contributions of the different pseudostates.

wave incident from the right. For each energy one could take the symmetric and antysimmetric combinations of the momentum normalized continuum wave functions

$$\begin{aligned} \Psi^s_{\pm k} &= \frac{1}{\sqrt{2}} \left[\Psi_{+k}(x) + \Psi_{-k}(x)\right], \\ \Psi^a_{\pm k} &= \frac{1}{\sqrt{2}} \left[\Psi_{+k}(x) - \Psi_{-k}(x)\right], \\ \langle \Psi^\rho_k | \Psi^{\rho'}_{k'} \rangle &= \delta_{\rho\rho'} \delta(k - k'), \end{aligned} \tag{2.53}$$

where $\rho = s, a$. Since our weakly-bound state is symmetric, only antisymmetric states are connected by the x operator. So the B_1 distribution for the "exact" case is given by

$$\frac{dB_1}{dk} \propto \left| \int_{-\infty}^{+\infty} dx \; \Psi^*_b(x) \; x \; \Psi^a_{\pm k}(x) \right|^2 . \tag{2.54}$$

To emphasize this point it is interesting to compare the result obtained using the discretized pseudostates and exact continuum with an analytic expression. This formula is obtained by approximating the weakly-bound wave function by a decaying exponential and the continuum state by a free plane wave. In this case, in fact, aside from a normalization factor and as a

function of the momentum k, the result is

$$\frac{dB_1}{dk} \propto \left| \int_{-\infty}^{+\infty} dx\ e^{-k_b|x|}\ x\ e^{ikx} \right|^2 \propto \frac{k_b^2 k^2}{(k^2+k_b^2)^4}, \tag{2.55}$$

where k is the momentum in the continuum and $k_b = \sqrt{\frac{2\mu|E_b|}{\hbar^2}}$ is the momentum associated to the weakly-bound second state.

The comparison (in the BOX case) between analytical, exact, and pseudostates results for dB_1/dk is shown in figure (2.8). In particular, for the pseudostates calculation

$$\frac{dB_1}{dk}|_i = \frac{B_1(k_i)}{k_{i+1} - k_{i-1}}. \tag{2.56}$$

The alternative methods are in good agreement.

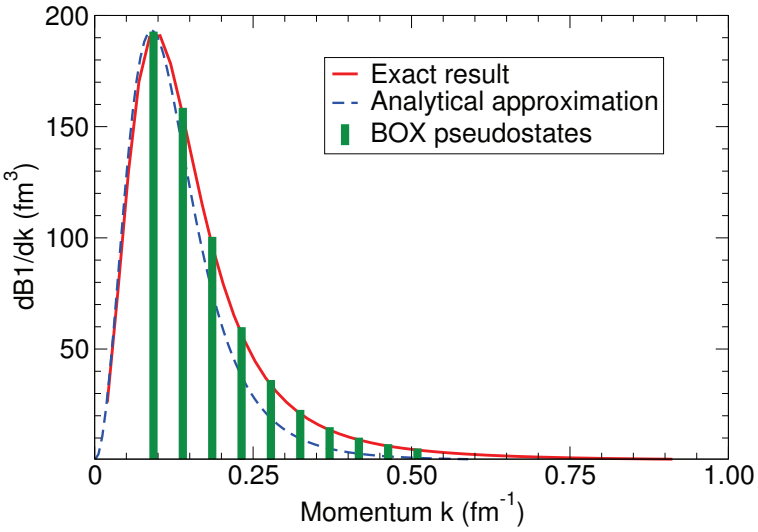

Figure 2.8: $\frac{dB_1}{dk}$, as a function of momentum, calculated in the BOX case (with $x_b = 120$ fm, green bars) compared with analytical (dashed blue line) and "exact" results (solid red line).

Chapter 3

Scattering of one-particle in the field of two potential wells

In this chapter we study the collision of the system investigated in chapter 2 by another well, which can be regarded as a toy model for the problem of the scattering of a halo nucleus by another nucleus. This constitutes an effective three-body problem, whose solution in three dimensions is extremely complicated, particularly when breakup and rearrangement channels are to be considered. Our one-dimensional model provides the essential three-body nature of this problem, and allows for a much simpler application and assessment of different methods of solution. To simplify further the problem, we assume that the potential well representing the projectile moves according to a predetermined classical trajectory, although the internal motion of the "valence" particle is treated fully quantum-mechanically. This corresponds to a semiclassical approach of the scattering problem.

Different approaches are investigated for the dynamics involving one-body systems: the "exact" time-dependent solution is presented in section 3.1, while two aproximate solutions (the coupled-channels method and a perturbative calculation) are presented in sections 3.2 and 3.3. We then study the dependence of our results on the distance of closest approach and the influence of the Q-value in section 3.4. Finally, in section 3.5 we compare exact and approximate methods presenting various model cases including different reaction channels. The role of continuum is also discussed.

We consider the problem of one particle[1], initially bound in a one-dimensional potential well (the "target"), subject to an external field, which is also represented by a potential well (the "projectile"), and which moves in one dimension according to a predetermined classical equations of motion. This situation describes schematically the collision between two nuclei, each one modeled by a potential well, and it permits to understand the mechanisms which govern a nuclear reaction by following the evolution of the wavefunction associated to the particle. In particular, we intend to simulate direct reactions, which are characterized by grazing collisions with a small overlap between the projectile and target. To simulate this situation in our one-dimensional model, the distance of closest approach is chosen in such a way that the two well only barely overlap. Initially, since we assume the particle to be a target valence nucleon, it coincides with an eigenstate of the target potential well. During the reaction the particle will feel the interaction with the colliding nucleus, i.e. the projectile potential well. Depending on the initial parameters of the reaction, the particle will more likely remain in its initial state (elastic scattering), jump to an excited bound level of the target (inelastic scattering), transfer to a bound level of the other nucleus, or it could leave the initial nucleus and escape to the continuum (breakup). As a consequence, the particle wavefunction will change, according to the probability to excite the different reaction channels.

Let us start the model description by specifying the Hamiltonian and the initial conditions. The system is described with the Hamiltonian

$$\mathcal{H}(x,t) = -\frac{\hbar^2}{2\mu}\frac{\partial^2}{\partial x^2} + V_T(x) + V_P(x - x_p(t), t), \tag{3.1}$$

where we include two potentials V_T and V_P, chosen with a Woods-Saxons shape (2.1) and associated to target and to projectile respectively. In our "semiclassical" model the target is at rest and only the projectile potential moves according to a classical trajectory. We can use the classical uniformly accelerated motion

$$x_p(t) = x_0 + vt + \frac{1}{2}at^2, \tag{3.2}$$

where $x_p(t)$ is the position of the center of the projectile well at each instant

[1] Note that, since we do not simulate Coulomb barriers, we assume the valence particle to be a neutron.

t, x_0 is the projectile position at $t = 0$ ps which corresponds to the moment of distance of closest approach, v is the asymptotic velocity of the projectile, assumed to be constant until $t = t_{initial}$ in which it starts to feel the interaction with the target and accelerates with constant acceleration a. In this case we choose the spatial grid interval $dx = 0.2$ fm and the time interval dt. Alternatively, we use the trajectory proposed in [35]

$$x_p(t) = x_0 + \sqrt{\rho^2 + (vt)^2} - \rho, \tag{3.3}$$

that accounts for the projectile motion with fixed asymptotic velocity v at large distance, corresponding to an asymptotic energy $E_P = 1/2mv^2$, which regulates the effective duration of the reaction (the higher the asymptotic energy, the faster is the reaction), and a distance of closest approach x_0 between the two centers of the potentials. This trajectory differs from the previous one in the fact that the projectile is changing its acceleration over the distance ρ, thus simulating the nuclear interaction with the target; in fact at $t = \pm\infty$ the trajectory tends to a uniform motion with zero acceleration. It is also more intuitive, because it allows the use of standard parameters of the scattering theory. Fixing a grid size equal to that in previous case, here we determine the time interval as $dt = dx/4v$. The turning point of the collision corresponds to $t = 0$, as well.

Upon variation of these parameters, one can simulate different kinematical conditions due to different bombarding energies and impact parameters (corresponding to partial waves in a quantum-mechanical description), while the choice of the parameters of the two potentials accounts for the different masses of the colliding nuclei, the Q-values of the different final channels as well as the possibility of simulating weak binding conditions.

By solving separately the time independent Schroedinger equation for each well

$$\mathcal{H}_J \Phi_J(x) = E_J \Phi_J(x), \tag{3.4}$$

with the Hamiltonian

$$\mathcal{H}_J = \left[-\frac{\hbar^2}{2\mu} \frac{d^2}{dx^2} + V_J(x) \right], \tag{3.5}$$

we obtain two sets of bound levels $\Phi_J(x)$; depending to the kind of reaction under study we will select one of these levels as the initial state of our single-

particle wave function. For example, to describe a pick-up reaction we will choose as initial state a single-particle level in the target. In the simulations presented here we will always choose a target wavefunction as initial one. In figure 3.1 we present the initial situation with the target and projectile potentials in their initial positions on the spatial grid.

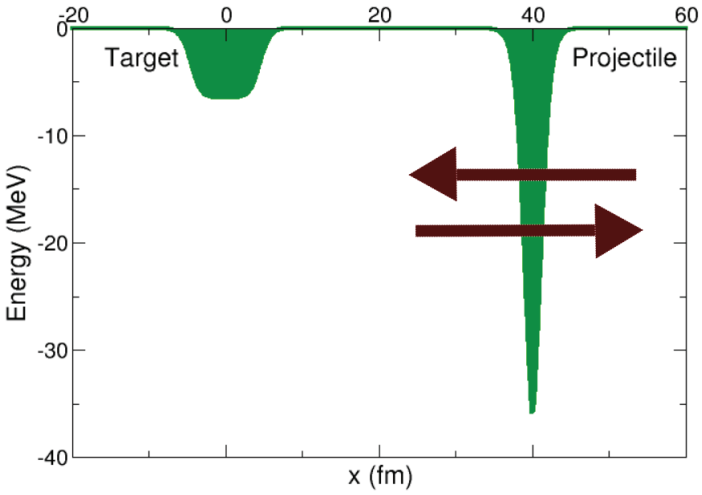

Figure 3.1: Target and projectile potentials in their initial positions on the spatial grid. The arrows schematically indicate the potential motion.

The problem can be solved in many different ways. On one hand, we can get the exact solution of the problem by numerically solving the corresponding time-dependent Schroedinger equation (section 3.1). On the other hand, we can obtain an approximate solution using the methods usually applied in solving three-dimensional scattering problems (sections 3.3 and 3.2).

3.1 Exact time-dependent solution

In the case of "exact" solution, we proceed to compute the time evolution of the valence neutron wavefunction $\Psi(x,t)$ by numerically solving the time dependent Schroedinger equation

$$i\hbar\frac{\partial}{\partial t}\Psi(x,t) = \mathcal{H}(x,t)\Psi(x,t), \tag{3.6}$$

with the Hamiltonian (3.1).
The wavefunction Ψ is confined within an interval containing the two wells. It is calculated at fixed points with coordinates x_μ separated by dx. According to [53], one can solve the problem by representing the system Hamiltonian by a tridiagonal matrix

$$\mathcal{H}_{\mu\nu} = -\frac{\hbar^2}{2mdx^2}\left(\delta_{\mu\nu+1} + \delta_{\mu\nu-1} - 2\delta_{\mu\nu}\right) + \delta_{\mu\nu}\left[V_T(x_\mu) + V_P(x_\mu - x_p(t))\right], \tag{3.7}$$

and the time evolution of the wavefunction is governed by the so-called Padé approximation of the evolution operator:

$$\Psi(t+dt) = \left(1 + \frac{idt}{2\hbar}\mathcal{H}\right)^{-1}\left(1 - \frac{idt}{2\hbar}\mathcal{H}\right)\Psi(t), \tag{3.8}$$

where dt is a finite time step, and $\mathcal{H}$ is the matrix in equation (3.7) at the intermediate time $t + dt/2$. Note that this evolution operator is unitary.
An alternative approach is to integrate the differential equation using a finite-diference method, such as the Runge-Kutta method. For that, in this work we make use of the routines *D02PVF* and *D02PCF* of the NAG library[2]. Although this solution prevents us from a complete control of the code, it was found to be faster than the Padé method. We have also verified that both methods lead to identical results.
At the end of the time evolution, we can compute the final probabilities for each reaction channel by projecting the final wavefunction $|\Psi(x,t_f)\rangle$ onto the corresponding eigenstates of each well obtained by solving equation (3.5) for each potential (target bound states $\Phi_i^T(x)$ for elastic and inelastic, projectile bound states $\Phi_i^P(x)$ for transfer channels)

$$\mathcal{P}_{elastic} = |\langle\Phi^T_{g.s.}(x)|\Psi(x,t_f)\rangle|^2, \tag{3.9}$$

$$\mathcal{P}_{inelastic} = |\langle\Phi^T_{i\neq g.s.}(x)|\Psi(x,t_f)\rangle|^2, \tag{3.10}$$

$$\mathcal{P}_{transfer} = |\langle\Phi^P_{i}(x)|\Psi(x,t_f)\rangle|^2. \tag{3.11}$$

We can also evaluate the breakup probability either by direct subtraction

$$\mathcal{P}_{breakup} = 1 - \mathcal{P}_{elastic} - \mathcal{P}_{inelastic} - \mathcal{P}_{transfer}, \tag{3.12}$$

[2]We are also imposing vanishing boundary conditions.

or by overlapping with the apropriate continuum states

$$\mathcal{P}_{breakup} = \left| \int dk \langle \Phi_{\pm k}(x) | \Psi(x, t_f) \rangle \right|^2 , \tag{3.13}$$

as we will show later in section 3.3.1.

3.2 Perturbative solution: first order approximation

The magnitude of the transition probability from $|\Phi_i\rangle$ to $|\Phi_f\rangle$ depends on the strength of the interaction $V(x - x_P(t))$. A measure of this stregth is given by the form factor [54]

$$\begin{aligned} F_{if}^{inelastic}(x_p(t)) &= \langle \Phi_i^T(x) | V_P(x - x_P(t)) | \Phi_f^T(x) \rangle, \\ F_{if}^{transfer}(x_p(t)) &= \langle \Phi_i^T(x) | V_P(x - x_P(t)) | \Phi_f^P(x - x_P(t)) \rangle. \end{aligned} \tag{3.14}$$

As an example, we show in figure 3.2 the form factor for transfer and inelastic processes. We simulate a transition from the target ground state to the first and second excited states of the same potential well (blue dotted Inelastic 1 and dotted/dashed violet Inelastic 2), and the trasfer to the projectile ground and first excited states (red dahed Transfer g.s. and solid orange Transfer 1). Note that the transfer form factor has a longer tail as compared to the form factor of an inelastic scattering. This is due to the overlap between the projectile wavefunction and the potential. Moreover, the transition to states with the same parity as the initial state are favoured (Inelastic 2 with respect to Inelastic 1 and Transfer g.s. with respect to Transfer 1).
The form factor measures the number of quanta which are exchanged during the collision in the transition to the state $|\Phi_f\rangle$. If it is a small number there is only a small chance that a quantum is exchanged, and one may treat the excitation of the state by first order perturbation theory [35, 55]. This means assuming that the valence particle evolves from the initial to final state in a single step. This solution is reliable only when the main channel of the reaction is the elastic scattering (if this is not the case, as we will see later in section 3.5, the resultant probabilities might also exceed 100%).
In first order, the probability $P_j^I(t_{final})$ for the population of the j-th state

(with energy E_j) of the potential $I = T, P$ is given by

$$\mathcal{P}_j^T(t_f) = \left| \frac{1}{i\hbar} \int_{t_i}^{t_f} dt \langle \Phi_i^T(x) | V_P(x - x_p(t)) | \Phi_j^T(x) \rangle e^{\frac{i(E_j - E_i)t}{\hbar}} \right|^2,$$
$$\mathcal{P}_j^P(t_f) = \left| \frac{1}{i\hbar} \int_{t_i}^{t_f} dt \langle \Phi_i^T(x) | V_P(x - x_p(t)) | \Phi_j^P(x - x_p(t)) \rangle e^{\frac{i(E_j - E_i)t}{\hbar}} \right|^2. \quad (3.15)$$

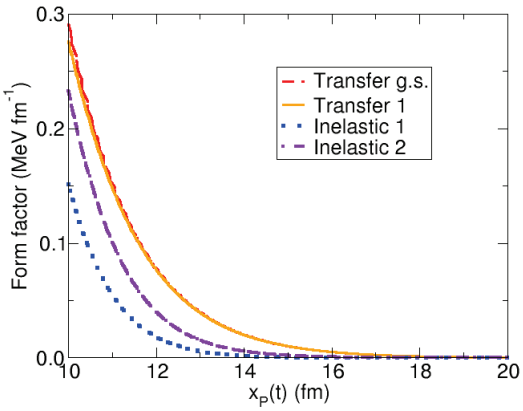

Figure 3.2: An example of form factor for transfer (red dahed and solid orange lines) and inelastic ((blue dotted and dotted/dashed violet lines) processes as defined by equations (3.14), as a function of the relative distance between target and projectile during the collision.
For this calculation we used a target Woods-Saxons potential well (2.1) with $V_0 = -10.5$ MeV, $R = 6.0$ fm, and $\alpha = 0.6$ fm, and bound levels of energy $E_{g.s.} = -9.41$, $E_1 = -6.43$, and $E_2 = -2.44$ MeV. We have chosen a projectile potential with parameters $V_0 = -8.50$ MeV, $R = 3.5$ fm, and $\alpha = 0.6$ fm, and bound states of energy $E_{g.s.} = -5.74$ and $E_1 = -1.14$ MeV. The target ground state is the initial state. The projectile potential moves according the trajectory (3.3) with an asymptotic energy of $E = 5$ MeV.

In first order approximation the probability to remain in the initial state $\mathcal{P}_0$, i.e. elastic scattering probability, corresponds to 100%. Since this does not conserve the total flux, one often prefers to define the elastic probability as

$$\mathcal{P}_0 = 1 - \sum_{j \neq 0} \mathcal{P}_j. \quad (3.16)$$

However, in the case of strong couplings and great excitation probabilities, this definition could lead to negative values of $\mathcal{P}_0$. For this reason we have preferred here to stick to the first option, and so we just indicate a 100% probability for the elastic scattering in first order approximation in the results section 3.5.

3.3 Approximate solution within the coupled-channels method

The same problem can be solved with the so-called coupled-channels method, which is a popular framework used to describe quantum collision problems in atomic, molecular and nuclear physics. For this calculation we follow the formulation of reference [35], and we take into account two finite sets of wavefunctions, related to the target and the projectile potentials: $\Phi_j^T(x)$ and $\Phi_j^P(x)$, of N_T and N_P states respectively. For collisions among tighly-bound systems, the basis expansion is usually restricted to bound states of the projectile and target systems. However, when one of them is weakly-bound, it is important to include also continuum states. For that, it is convenient to use a discrete representation of square-integrable functions, as those discussed in chapter 2 (we will discuss in more detail the inclusion of continuum in coupled-channels method in section 3.3.1). Moreover, they are defined in a one-dimensional spatial grid, whose origin corresponds to the center of the target potential, which also corresponds to the laboratory frame. A different choice, like the center of mass frame of reference in which the two potentials are moving, would have implied a careful treatment of target and projectile wavefunctions due to the non-covariance of Schoedinger equation (see Appendix C). In addition, these two bases are non-orthogonal so we will solve this problem introducing a dual basis, as explained below.
The wavefunction describing the entire system is expressed as a combination of target and projectile states

$$\Psi(x,t) = \sum_{j=1}^{N_T} c_j^T(t)\Phi_j^T(x) + \sum_{j=1}^{N_P} c_j^P(t)\Phi_j^P(x), \tag{3.17}$$

and the solution of the problem is reduced to the determination of the time evolution of the coefficients $c_j^{(T,P)}(t)$ from the finite set of coupled differential

equations

$$i\hbar\frac{\partial c_j^T}{\partial t} = \sum c_k^T \langle \omega_j^T | V^P | \Phi_k^T \rangle + \sum c_k^P \langle \omega_j^T | V^T | \Phi_k^P \rangle,$$
$$i\hbar\frac{\partial c_j^P}{\partial t} = \sum c_k^T \langle \omega_j^P | V^P | \Phi_k^T \rangle + \sum c_k^P \langle \omega_j^P | V^T | \Phi_k^P \rangle. \tag{3.18}$$

These equations are solved with the initial conditions $c_j^P(t=-\infty)=0$ and $c_j^T(t=-\infty)=\delta_{i,j}$, where i indicates one of the bound states in the target potential well.

To derive equations (3.18), we first insert the equation (3.17) of the system wavefunction $\Psi(x,t)$ into the time-dependent Schroedinger equation (3.6), thus obtaining

$$\sum_j i\hbar\frac{\partial c_j^T}{\partial t}\Phi_j^T + \sum_j i\hbar\frac{\partial c_j^P}{\partial t}\Phi_j^P = \sum_j c_j^T(\mathcal{H}-\mathcal{H}_T)\Phi_j^T + \sum_j c_j^P(\mathcal{H}-\mathcal{H}_P)\Phi_j^P \tag{3.19}$$

where $\mathcal{H}_J$ is the Hamiltonian corresponding to the potential well $J=T,P$ of equation (3.5), and $\mathcal{H}$ is the Hamiltonian of the full system presented in equation (3.1).

In order to isolate the time derivatives and to solve the non-orthonormal problem, we introduce a dual basis associated to each well $\omega_j^{(T,P)}(x,t)$, conjugate to the channel wavefunctions of each potential, through the definition

$$\langle \Psi_m^I | \omega_n^J \rangle = \delta_{I,J}\delta_{n,m}, \tag{3.20}$$

where $I,J=T,P$ and $n,m=1,2,...N_{(T,P)}$. A projection of equation (3.19) on the dual wavefunctions yields the coupled equations (3.18).

According to [56–58], the dual basis is time dependent and is a combination of the overlaps between target and projectile bases states. One can construct the dual basis within the space of channel wavefunctions as follows

$$|\omega_n^T\rangle = (1-P_P)\sum_{k=1}^{N_T} |\Phi_k^T\rangle \beta_{kn}^T, \tag{3.21}$$

where P_P is the projection operator

$$P_P = \sum_{q=1}^{N_P} |\Phi_q^P\rangle\langle\Phi_q^P|, \tag{3.22}$$

and similarly for ω_n^P. From the definition (3.21) we see that equation (3.20) is automatically fulfilled for $I = T$ and $J = P$. Inserting equation (3.21) into (3.20) for $I = J = T$ we get

$$\beta_{mn}^T - \sum_{q=1}^{N_P}\sum_{k=1}^{N_T}\langle\Phi_m^T|\Phi_q^P\rangle\langle\Phi_q^P|\Phi_k^T\rangle\beta_{kn}^T = \delta_{mn}, \tag{3.23}$$

thus, β^T is the inverse of the matrix

$$M_{mn}^T = \delta_{mn} - \sum_{q=1}^{N_P}\langle\Phi_n^T|\Phi_q^P\rangle\langle\Phi_q^P|\Phi_m^T\rangle. \tag{3.24}$$

Since M^T is an Hermitian matrix, β^T is also Hermitian. An alternative derivation of the dual basis is given in [35].

In problems involving different mass partitions, one may use the so-called prior and post representations of the Hamiltonian, depending on whether one considers the projectile-target combination of the initial or final states; by definition they have to give the same results. Equations (3.17) and (3.18) are constructed in prior representation. In post representation we can expand the system wavefunction on the dual basis

$$\Psi(x,t) = \sum_n \tilde{c}_n^T\omega_n^T + \sum_n \tilde{c}_n^P\omega_n^P, \tag{3.25}$$

and, following a derivation similar to the one given for the prior representation, we obtain the set of coupled-equations

$$\begin{aligned} i\hbar\frac{\partial\tilde{c}_n^T}{\partial t} &= \sum\tilde{c}_m^T\langle\Phi_n^T|V^P|\omega_m^T\rangle + \sum\tilde{c}_m^P\langle\Phi_n^T|V^P|\omega_m^P\rangle, \\ i\hbar\frac{\partial\tilde{c}_n^P}{\partial t} &= \sum\tilde{c}_m^T\langle\Phi_n^P|V^T|\omega_m^T\rangle + \sum\tilde{c}_m^P\langle\Phi_n^P|V^T|\omega_m^P\rangle. \end{aligned} \tag{3.26}$$

From the system wavefunction $\Psi(x,t)$, we can also extract amplitudes for excitation and transfer in post and prior representations through the expressions

$$\begin{aligned} \tilde{c}_n^I &= \langle\omega_n^I|\Psi\rangle, \\ c_n^I &= \langle\Phi_n^I|\Psi\rangle. \end{aligned} \tag{3.27}$$

Due to post-prior symmetry, the amplitudes in the two representations are related by

$$\tilde{c}_n^T = c_n^T + \sum_m \langle \Phi_n^T | \Phi_m^P \rangle c_m^P,$$
$$\tilde{c}_n^P = c_n^P + \sum_m \langle \Phi_n^P | \Phi_m^T \rangle c_m^T. \tag{3.28}$$

The probabilities to populate the different final channels are defined as

$$\mathcal{P}_j^{(T,P)} = |c_j^{(T,P)}|^2 \tag{3.29}$$

in the prior representation, or as

$$\tilde{\mathcal{P}}_j^{(T,P)} = |\tilde{c}_j^{(T,P)}|^2 \tag{3.30}$$

in the post representation. The label j denotes the quantum number of the final state in one of the two wells.

Because of the non-orthogonality of the basis states, the sum of these "probabilities" is not conserved during the collision. If we instead define the "probabilities" by

$$\mathcal{P}_j^{(T,P)} = Re\left[(c_j^{(T,P)})^* \tilde{c}_j^{(T,P)}\right], \tag{3.31}$$

conservation of total probability is always fulfilled within the coupled-channel formalism. This follows from the fact that the matrix governing the time evolution of the amplitudes in the post representation is minus the hermitian conjugate of the matrix that determines the time evolution of the amplitudes in the prior representation. We shall therefore call equation (3.31) the *unitary representation* of probabilities. However, we can not be sure that these quantities are always non-negative during the collision.

After the collision, when all overlaps between the basis states in the two wells vanish, the amplitudes for a given transition are the same in the post and prior representation, as evident from equation (3.28). This so-called post-prior symmetry implies that the total probability is conserved once the collision is over, also in a truncated coupled-channel treatment.

3.3.1 Inclusion of continuum in the coupled-channels method

In reference [35] only bound states were included in the bases and, hence, breakup channels were omitted. This is possibly justified for tighly bound systems, but not for weakly bound ones, for which the coupling to these channels can be very important.

In a coupled-channels scheme, as we use here, but also for the calculation of breakup probabilities presented for the exact model in equation (3.13), one can not include the full continuum spectrum, since these states form a continuum of energies. Moreover, the fact that these states are not square-integrable poses numerical problems since the coupling potentials become of infinity range. To overcome these difficulties, it is customary to resort to an approximate, discrete description of the continuum. For that, we may use the pseudostates introduced in chapter 2. We remind here that bound states are obtained by solving the finite-difference method on the whole grid [45], as presented in section 2.1.1.

In the case of coupled-channels and first order approximation methods, we should be careful that at the end of the time evolution there is no overlap between target and projectile bases. This is due to the fact that the two bases are not mutually orthogonal, so while they overlap the problem loses unitarity, as we mentioned in section 3.3. After the reaction, when the projectile is far enough for these overlaps to vanish, the problem has restored its unitarity and we can evaluate the final probabilities. Thus, if we include the continuum we need to restrict it to a small range $[-x_b^J, +x_b^J]$ centered in the corresponding potential $J = target, projectile$, in order that $x_b^T + x_b^P > x_P(t_{max})$. A limitation of this method is that the choice of x_b^J is done *a posteriori* to include the breakup component into the continuum interval. In situations in which the breakup channel is dominant, the wavefunction component related to the excitation to the continuum escapes far away from the potentials, and it becomes impossible to apply the method just described. What we suggest and apply in the case in which all the reaction channels are relevant is to include in the bases few continuum pseudostates defined along the entire spatial grid. In this way the calculation does not diverge and the total probability exceedes by only a few percent the unity limit, but we are able to reproduce quite well the exact results.

In the case of one-particle systems, as we have seen in section 2.1.3, we can also construct the "exact" positive energies states. In this case we compute the breakup probability as a function of momentum k

$$\mathcal{P}(k) = |\langle\varphi(k,x)|\Psi(x,t_f)\rangle|^2, \tag{3.32}$$

where $\Psi(x,t_f)$ represents the final wavefunction obtained by solving the problem with either the exact method (3.6) or constructed after applying the coupled channels-method (3.17). Changing variables and introducing the Jacobian factor, we can express the probability as a function of the energy $E = \dfrac{\hbar^2 k^2}{2\mu}$

$$\mathcal{P}(E) = \frac{dk}{dE}\mathcal{P}(k) = \sqrt{\frac{\mu}{2E\hbar^2}}\mathcal{P}(k). \tag{3.33}$$

Of course, the total probability is conserved

$$\int_0^{+\infty} \mathcal{P}(E)dE = 1 - \sum_{i=1}^{N_b^T} \mathcal{P}(E_i) - \sum_{j=1}^{N_b^P} \mathcal{P}(E_j). \tag{3.34}$$

3.4 Numerical results: dependence on the distance of closest approach and on the Q-value

In this section, we test the exact method results to understand their dependence on the distance of closest approach and on the Q-value. For simplicity, in this example, the motion of the projectile well is assumed to follow the uniformly accelerated motion (3.2). The choice of the depths of the two wells, as well as the choice of the initial single-particle state, determine the characteristics of the two colliding objects, for example the situation of weak binding in a halo-like system. In particular, we have chosen two model cases to show the different behaviour of well-bound and weakly-bound systems.
In the case of the bound system, whose exact result is depicted in figure 3.3, the fixed well is chosen in such a way that the single particle is moving in the only bound state (with binding energy $E_{g.s.} = -3.10$ MeV), while the moving well admits two initially unoccupied bound levels (of energy $E_{g.s.} = -16.3$ and $E_1 = 3.21$ MeV). In this model case the projectile is moving following a fixed classical trajectory, like that presented in equation (3.2). The parameters chosen to define the trajectory[3] of the example in figure 3.3 are $x_0 = 10$ fm and $a = 0.3/\hbar^2$ fm/ps^2. The different frames refer to different times (the total collision time is divided in 210 steps and the corresponding time is quoted in each frame) and in each frame the upper part gives the square of the one-particle wave function while the lower frame gives the actual position of the two potentials at the same time. As apparent from the figure, when the tail of the moving well starts to overlap with the fixed well (frame c) part of the wave function enters in the moving well and then follows its motion (frames d-f). At the end of the process, by projecting the final wave function onto the target and projectile eigenstates one can determine the elastic and transfer probabilities, respectively. The final probabilities for this case are 60% for elastic scattering, and 40% for transfer. The presence of a node in the part of wave function inside the moving well clearly indicates that the transfer takes place mostly to the second single particle state. Note that the breakup probability is practicably negligible in this case.

[3] For this case the time is expressed in unit of $\hbar$.

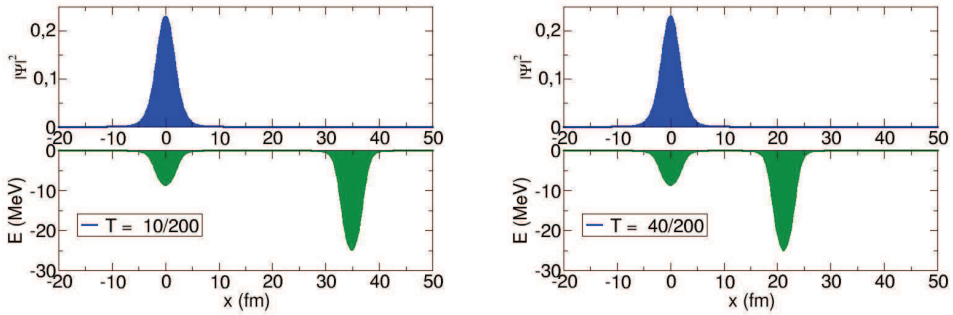

(a)

(b)

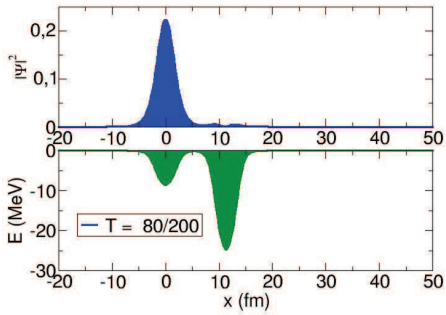

(c)

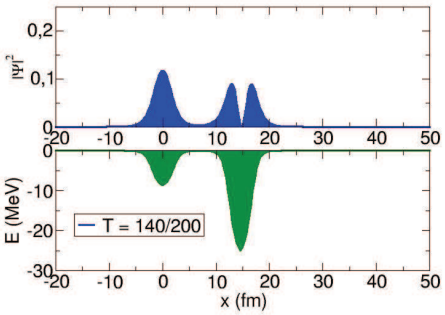

(d)

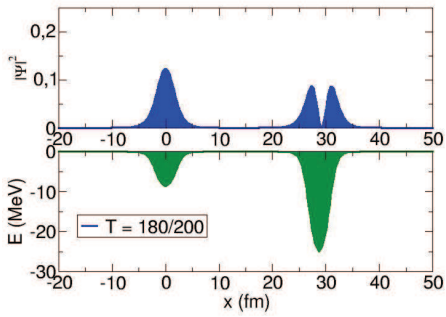

(e)

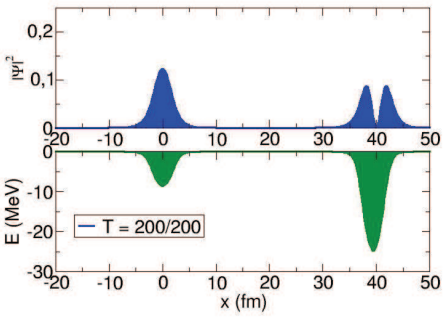

(f)

Figure 3.3: Time evolution of the exact wavefunction for the well bound model case. In all frames, corresponding to different times, the upper part gives the square of the wavefunction at that time and the lower part the actual position of the two potentials at the same time.

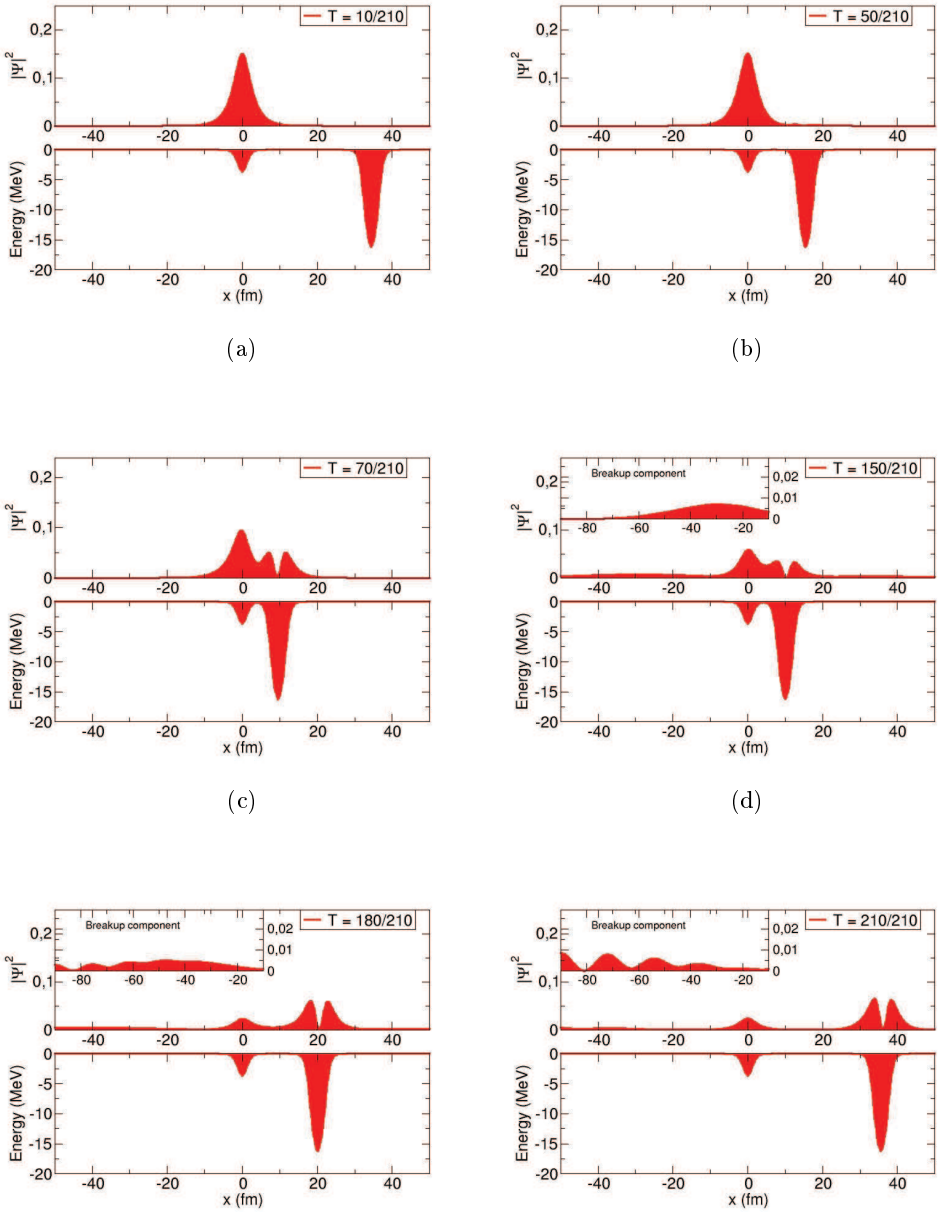

(a) (b) (c) (d) (e) (f)

Figure 3.4: Time evolution of the exact wavefunction for the weakly-bound model case. In all frames, corresponding to different times, the upper part gives the square of the one-particle wave function at that time and the lower part the actual position of the two potentials at the same time. The wave function is amplified in the insets, to highlight the continuum (breakup) part of the wave function.

To simulate the case of weakly-bound systems, shown in figure 3.4, we modify the depth of the potentials in order to obtain a weakly-bound eigenstate of the target ($E_{g.s.} = -0.91$ MeV) and projectile ($E_{g.s.} = -10.0$ and $E_1 = -0.89$ MeV) potentials. As in the previous case, the projectile is assumed to move according to the trajectory[4] (3.2) with distance of closest approach $x_0 = 10$ fm and acceleration $a = 0.3/\hbar^2$ fm/ps^2. The initial state is the target ground state. As a consequence of the weak binding the initial wave function displays a longer tail, which results on a larger overlaps between the two wells. The corresponding time evolution of the wave function is shown, at different stages of the reaction, in figure 3.4. The final probabilities for this case are 16% for elastic scattering, 36% for transfer, and 48% for breakup. The weak binding situation is also responsible for larger break-up probabilities. To emphasize the continuum part of the wave function, which is distributed over a large interval, we also show in the insets a zoom of the wave function in a region far from the two wells.

By varying the kinematical and/or potential parameters, the present models permits to simulate different physical situations. As an example, we discuss in the next subsections the influence of the distance of closest approach and the Q-value.

3.4.1 Distance of closest approach

We study here the influence on the calculated probabilities of the variation of the distance of closest approach. In our model this variable is defined as the minimum distance reached by the center of the projectile potential with respect to the center of the target potential well. According to our time definition, this position corresponds to $t = 0$. In figure 3.5 we show the result of transfer (blue), breakup (red) and elastic/inelastic (orange) channels probabilites as a function of the distance of closest approach. The lower panel of figure 3.5 corresponds to a bound system, while the upper panel refers to weakly-bound system results.

As we can see from figure 3.5, the probabilities display the expected exponentially decaying behavior arising from the combination of the tail properties of the two wells and of their eigenfunction. This trend is observed also experimentally [59, 60] and confirms that, despite the one-dimentional restric-

[4]For this case the time is expressed in unit of $\hbar$.

tion, our model encompasses physical features found in three-dimensions. It is therefore not surprising that, in the case of the initial weakly-bound system characterized by the long tail, the transfer probability survives to larger distances with a lower decaying rate. Note also that below a certain critical distance (approximately below 10 fm for the well-bound case and 12 fm for the weakly-bound one) the transfer probability becomes so large that in a perturbative picture we will have back and forth transfer, with resulting oscillatory behavior.

We can also observe that, in the weakly-bound case, the breakup probability is higher than in the well-bound case. This is, of course, consequence of the smaller binding energy of the initial state.

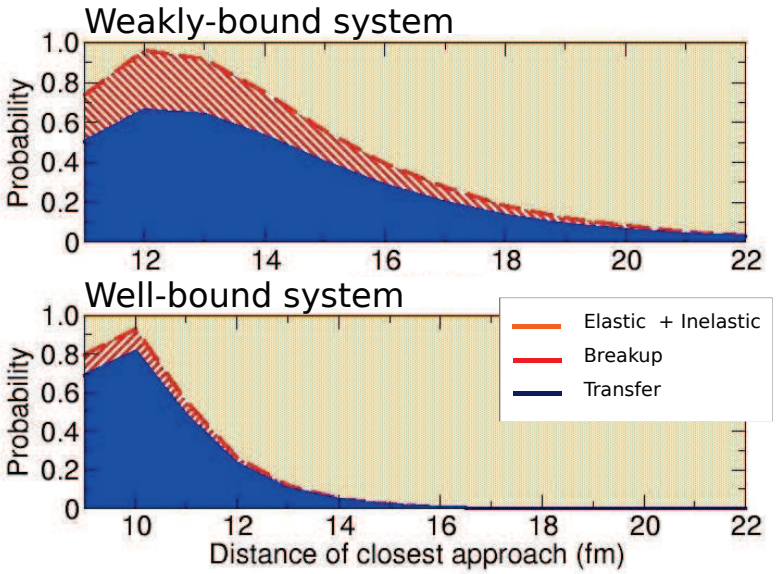

Figure 3.5: Elastic, transfer and breakup probabilities as a function of the distance of closest approach x_0 between the two colliding wells. The lower frame refers to the case of a well-bound initial single-particle state, whereas the upper frame corresponds to the case of a weakly-bound state. See text for details.

3.4.2 Influence of the Q-value

Another interesting test is the optimum Q-value [61]. The Q-value for a reaction is defined as the amount of energy released by that reaction; the optimum Q-value, Q_{opt}, is the value at which the reaction occurs with maximum probability. The Q-value defines a window, described by the adiabatic cut-off function $g(Q)$, in which the transition has more chances to occur. Therefore, the adiabatic cut-off function defines the actual value of the transition probability for the reaction channel i, given the probability expected by the model $\mathcal{P}_i$

$$P_i = \mathcal{P}_i g(Q_i). \tag{3.35}$$

The one-dimensional $g(Q)$ is defined as

$$g(Q) = e^{-\frac{(Q-Q_{opt})^2}{\hbar^2 a_0}}, \tag{3.36}$$

where a_0 is the projectile acceleration at the turning point. In one dimension the Q-value is simply defined as the difference between initial and final levels energy, and it is optimum when it approaches zero

$$Q_{opt} = E_f - E_i = 0. \tag{3.37}$$

Thus, just varying the energies of the corresponding bound states, i.e. the potential depth, we can study the transfer process as a function of the Q-value associated to the transfer process. In figure 3.6 we can see the results obtained for a well bound (panel a) and a weakly-bound (panel b) system.

As we can see from figure 3.6, the model reproduces the expected gaussian behavior due to the cut-off function (3.36) and it is peaked around the "optimal Q-value", which in our specific case of transfer of a neutral particle is close to zero. The width of the probability distribution depends on the projectile acceleration. As was already noted in figure 3.5, in the weakly-bound case there is a large contribution from breakup, which is strongly favored by the initial weak binding of the particle, and which shows a smoother dependence on the value of the single-particle energies in the moving well.

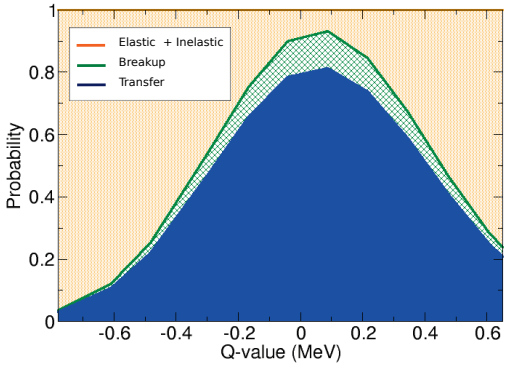

(a) Well-bound system.

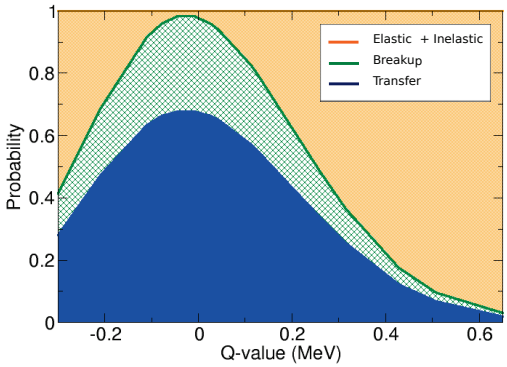

(b) Weakly-bound system.

Figure 3.6: Elastic, transfer, and breakup probabilities as a function of the difference between the energies of the single-particle states in the fixed and moving wells (Q-value). Results are shown for a well bound (a) and weakly-bound (b) systems.

3.5 Comparison of exact and approximate methods

In addition to the cases already presented, we have performed further calculations, aimed at exploring different kinematical situations. In each case, we present the exact time-dependent solution (section 3.1) and, whenever possible, we compare this result with the approximate solutions obtained with the coupled-channels and first order perturbative theory presented in sections 3.2 and 3.3. The chosen model cases have been selected to illustrate several physical situations in which different reactions channels are favoured; they are summarized in table 3.1.

Model case	Dominant channels	section
Case A	Elastic and inelastic	3.5.1
Case B	Elastic and breakup	3.5.2
Case C	Elastic, inelastic and breakup	3.5.3
Case D	Elastic, transfer and breakup	3.5.4
Case E	Elastic, inelastic, transfer and breakup	3.5.5

Table 3.1: Model cases presented in section 3.5 and the respective dominant channels.

3.5.1 Case A

We start with the simplest case in which we observe a dominance of elastic and inelastic channels.

The target and projectile potentials are depicted in figure 3.7 with their respective bound states wavefunctions, the target ground state is the initial state for this reaction and it corresponds to the dashed red curve in figure 3.7. This projectile follows the trajectory (3.3) with an asymtotic velocity of $0.1 \times c$, which corresponds to an asymptotic energy of 5.0 MeV. The reduced mass for this systems is 1.001 amu.

In figure 3.8 we present the potentials and the exact wavefunction at different moments of the time evolution. In each frame the upper panel shows the exact wavefunction and the lower displays the target and projectiles potentials.

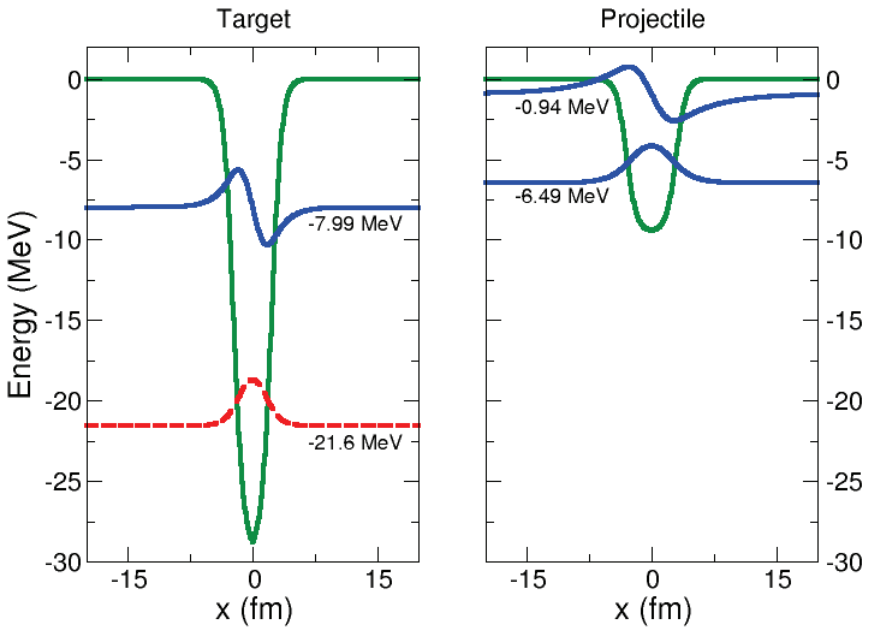

Figure 3.7: Target (left) and projectile (right) Woods-Saxon potential and corresponding bound states for the case A. The initial state, in this case the target ground state, is the dashed red curve.

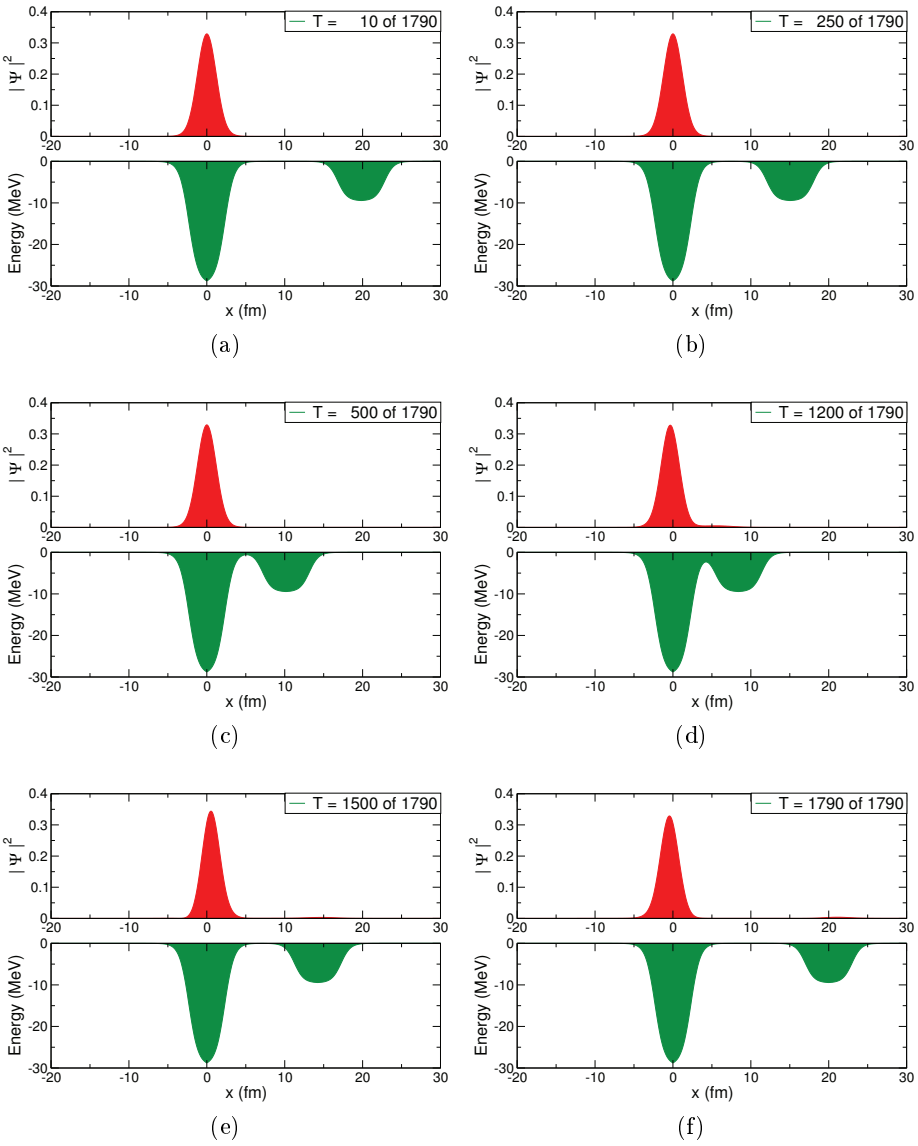

Figure 3.8: Results for the test case A (see Table 3.1). Upper panel: the squared total wavefunction at different times computed with the exact method. Lower panel: the target and projectile potential wells. In the legends the elapsed time is indicated for each frame.

In table 3.2 we present the results obtained by solving the problem using different approaches and different bases.

	Exact	1^{st} o.a.	$CC^{(1)}$	$CC^{(2)}$	$CC^{(3)}$	$CC^{(4)}$	$CC^{(5)(6)}$
Elastic	91 %	100 %	93 %	92.8 %	91 %	91 %	91 %
In. 1	7 %	5.6 %	7 %	7.0 %	8.7 %	8.7 %	7 %
Tr. g.s.	0.7 %	3 %	-	-	0.3 %	0.3 %	0.2 %
Tr. 1	0.5 %	0.3 %	-	-	0.08 %	0.08 %	0.8 %
Breakup	0.7 %	0.02 %	-	0.2 %	-	10^{-6}%	1 %

Table 3.2: Final probabilities for the model case A with exact method, coupled-channels method or first order approximation, with different bases choices.

In particular, they correspond to:

- **Exact** Calculation done by solving numerically the time dependent Schroedinger equation (3.6). The different results represent the probability for the valence neutron to remain in the ground state (Elastic) or to directly excite the corresponding bound states of the two potential wells (In. and Tr.) or to excite continuum states (Breakup).

- **1^{st} o.a.** Calculation done by applying the first order approximation in a perturbaive approach. In this case Breakup corresponds to the sum of the probability to excite the first 10 continuum pseudostates obtained with the BOX method using a radius equal to the maximum radius of the grid.

- **$CC^{(1)}$** Coupled-channels calculation in which only the two target bound states are included.

- **$CC^{(2)}$** Coupled-channels calculation using target bound levels plus the first 10 continuum pseudostates obtained with the BOX method with a radius equal to the maximum radius of the grid.

- **$CC^{(3)}$** Coupled-channels calculation including only target and projectile bound states.

- **$CC^{(4)}$** Coupled-channels calculation using the target and projectile bound states plus the first 5 pseudostates of the projectile continuum

obtained with the BOX method with a radius of 20 fm. It corresponds to an energy cutoff in the continuum of 4 MeV.

- **CC**$^{(5)}$ Coupled-channels calculation using the target and projectile bound states plus the first 5 pseudostates of the target continuum obtained with the BOX method with a radius of 20 fm. It corresponds to an energy cutoff in the continuum analogue to that of **CC**$^{(4)}$.

- **CC**$^{(6)}$ Coupled-channels calculation including target and projectile bases composed by bound and 5 continuum pseudostates calculated with BOX method in a $[-20; 20]$ fm range centered in the respective potential. This result is equal to the previous one CC$^{(5)}$. It corresponds to an energy cutoff in the continuum analogue to that of **CC**$^{(4)}$.

By comparing the results of table 3.2, we note that the first order approximation works reasonably well because the systems is in the perturbative regime in which most of the flux remains in the elastic channel.

The coupled-channels calcuation without transfer and continum channels, i.e. **CC**$^{(1)}$, reproduces rather well the elastic and inelastic probabilities. This is a consequence of the dominance of the elastic channel and, to a lesser extent, the inelastic channel in this case. We also observe that the coupled-channels method reproduces better the exact results when including some continuum states in the calculation. This could be surprising considering that the dominant channels in this model case are elastic and inelastic scattering, and the breakup component is very small. In particular, since **CC**$^{(5)}$ and **CC**$^{(6)}$ results are equal, we understand that the target continuum plays a crucial role in this case, even if the target potential is a well bound system. This could be expained considering that the potential which plays the principal role in this reaction is actually the target, because the valence particle is basically being excited from the ground state to the first excited state, and there are no favorable conditions for the transfer. So we conclude that in this case the inelastic scattering occurs involving also the target continuum during the reaction.

In figure 3.9 we show how the probability changes with time during the reaction. We present the elastic (blue) and inelastic (red) probabilities, comparing the Exact result (solid lines) with the **CC**$^{(6)}$ result (dotted lines). In the case of elastic channel the results of the two methods match quite well, while for the inelastic channel the coupled-channels results present

an oscillatory trend respect to the exact result. This might be due to the influence of continuum wavefunctions chosen for the $\mathbf{CC}^{(6)}$ calculation, or could be of numerical nature.

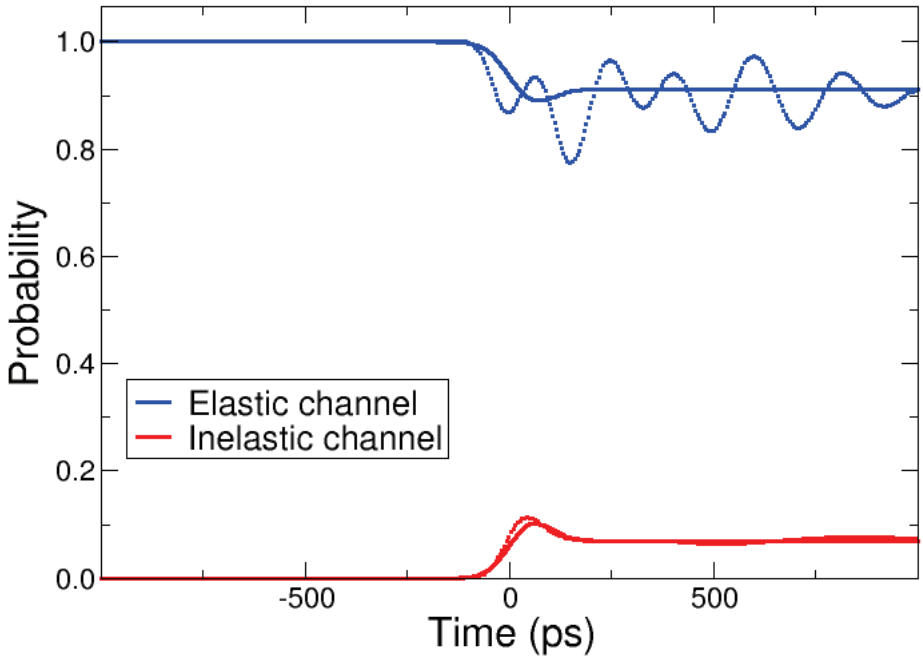

Figure 3.9: Evolution of probability as a function of time: the blue curves correspond to elastic scattering, while the red ones represent the inelastic scattering probability. Solid lines indicate results of the exact method, whereas the dotted lines correspond to results obtained with coupled-channels calculation $\mathrm{CC}^{(6)}$ which are listed in the last column of table 3.2.

3.5.2 Case B

We consider now a physical situation in which the excitation to the continuum (breakup) plays a more significant role. This is achieved considering as initial state a weakly-bound state of the target well, as illustrated with the dashed red curve in figure 3.10, where the target and projectile potentials are depicted with their respective bound states wavefunctions. This projectile follows the trajectory (3.3) with the same initial parameters of case A: asymtotic velocity of $0.1 \times c$ (0.5 MeV incident energy), and reduced mass of 1.001 amu.

The evolution of the exact wavefunction during the collision is presented in figure 3.11, where in each frame the central panel shows the exact wavefunction and the lower displays the target and projectiles potentials. In the upper panels of figure 3.11 appears the current of the "exact" wavefunction calculated according to the expressions derived in Appendix D.3.

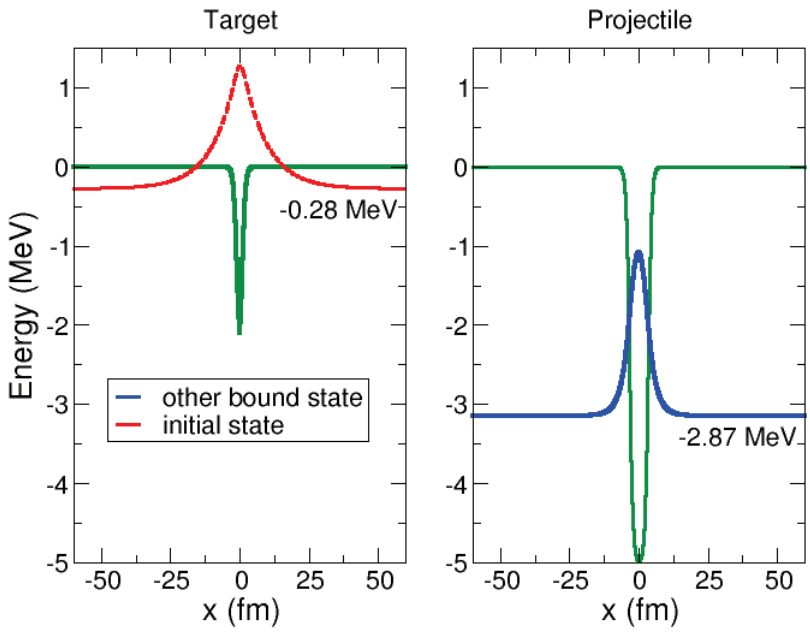

Figure 3.10: Taget (left) and projectile (right) Woods-Saxon potential and corresponding bound states for the model case B. The initial state, in this case the target ground state, is the dashed red curve.

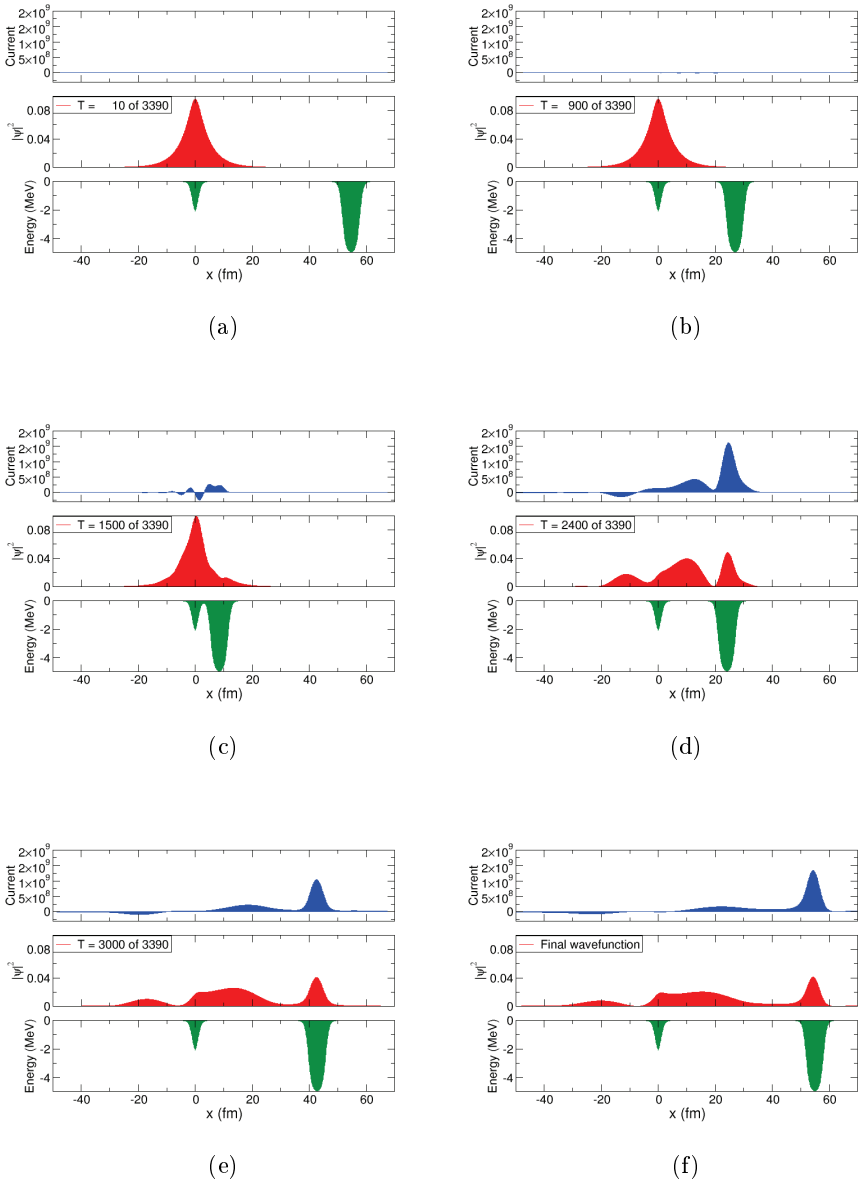

Figure 3.11: Model case B. Upper panel: the current of the wavefunction. Middle panel: the squared total wavefunction at different times obtained with the exact method. Lower panel: the target and projectile potential wells. In the legends the elapsed time is indicated for each frame.

The results for case B, obtained applying different methods, are presented in table 3.3.

	Exact	1^{st} o.a.	$CC^{(1)}$	$CC^{(2)}$	$CC^{(3)}$
Elastic	20.7 %	100 %	21.4 %	95 %	21 %
Transfer	0.3 %	101 %	-	5 %	0.04%
Breakup	79 %	116 %	78.6 %	-	79 %

Table 3.3: Final probabilities for the model case B using exact method, the coupled-channels method and the first order approximation, with different basis choices.

These results correspond to different calculations:

- **Exact** Calculation done by solving numerically the time dependent Schroedinger equation (3.6). The different results represent the probability for the valence neutron to remain in the ground state (Elastic) or to directly excite the projectile bound state (Transfer) or to excite continuum states (Breakup).
- **1^{st} o.a.** Calculation done by applying the first order approximation in a perturbaive approach. In this case Breakup calculation corresponds to the sum of the probability to excite the first 100 continuum pseudostates obtained with the BOX method using a radius equal to the maximum radius of the grid.
- **$CC^{(1)}$** Coupled-channels calculation using the target bound levels plus the first 50 continuum pseudostates obtained with the BOX method with a radius equal to the maximum radius of the grid. It corresponds to an energy cutoff in the continuum of 0.5 MeV.
- **$CC^{(2)}$** Coupled-channels calculation including only target and projectile bound states.
- **$CC^{(3)}$** Coupled-channels calculation using the target and projectile bound states plus the first 100 pseudostates of target continuum obtained with the BOX method with a radius of 40 fm. It corresponds to an energy cutoff in the continuum of 300 MeV.

By comparing the results of table 3.3, we can observe that the first order approximation (**$CC^{(3)}$**) fails because the system is not in the perturbative

regime. Then, as can be noticed in figure 3.11f, the component corresponding to breakup is almost completely contained within the range of $[-40, 40]$ fm at the end of the calculation, so these results can be well reproduced by the coupled-channels formalism if one defines the target continuum in that interval, as it is clear from the $\mathbf{CC}^{(3)}$ column in table 3.3. The choice of target continuum, instead of projectile continuum, is also due to the kind of reaction: the target is very weakly-bound and the transfer Q-value is not optimum, thus we expect the system to excite to low positive energy states with respect to the target.

In figure 3.12 we show how the probability changes with time during the reaction. We present the elastic (blue) and breakup (green) probabilities, comparing the Exact result (solid lines) with the $\mathbf{CC}^{(3)}$ result (dotted lines). In this case the two results agree satisfactorily during the whole time evolution for both the channels considered.

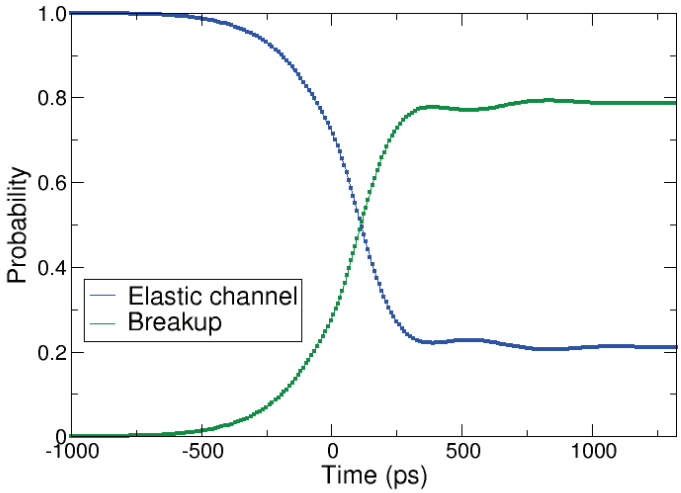

Figure 3.12: Evolution of probability as a function of time: the blue curves correspond to elastic scattering, while the green ones represent the breakup probability. Solid lines indicate the exact results, dotted lines correspond to results obtained with the coupled-channels calculation $\mathbf{CC}^{(3)}$ which are reported in the last column of table 3.3.

After comparing the results obtained applying the different methods in table 3.3, we next examine in more detail the excitation to the continuum (breakup) probabilities. We construct the "exact" continuum wavefunction following the prescription in section 2.1.3 for the two potentials, thus obtaining two sets of continuum wavefunctions. We then apply equations (3.32) and (3.33) to calculate the probability as a function of the positive energies. The results are displayed in figures 3.13 at low positive energies: the exact (solid lines) and coupled-channels (dashed lines) final wavefunctions have been projected onto the target (lower panel) and the projectile (upper panel) "exact" continuum. In figure 3.14 we show the same results extended to higher energies.

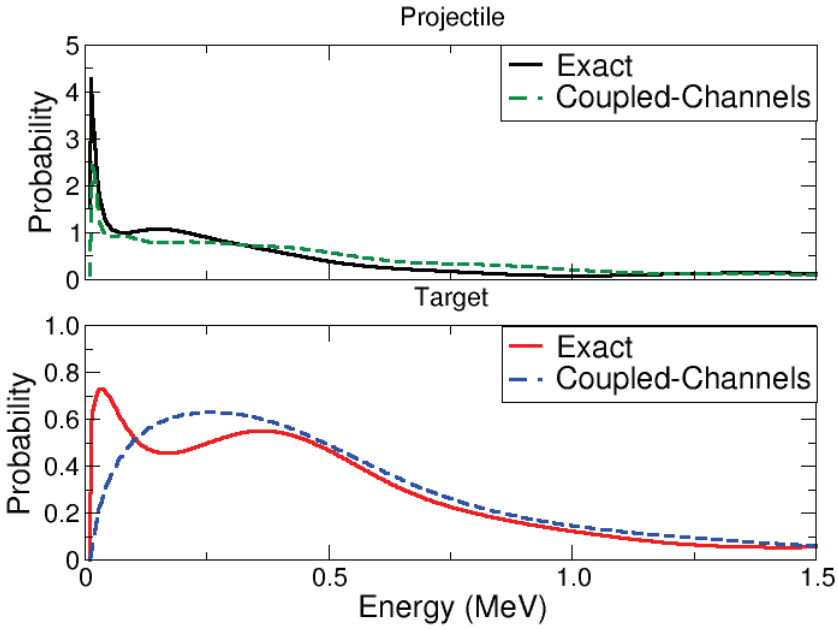

Figure 3.13: Breakup probabilities as a function of the excitation energy in the continuum. The upper and lower panels correspond to the projection on the projectile and target eigenstates, respectively. Solid lines use the exact total wave function, whereas the dashed lines are for the coupled-channels solution.

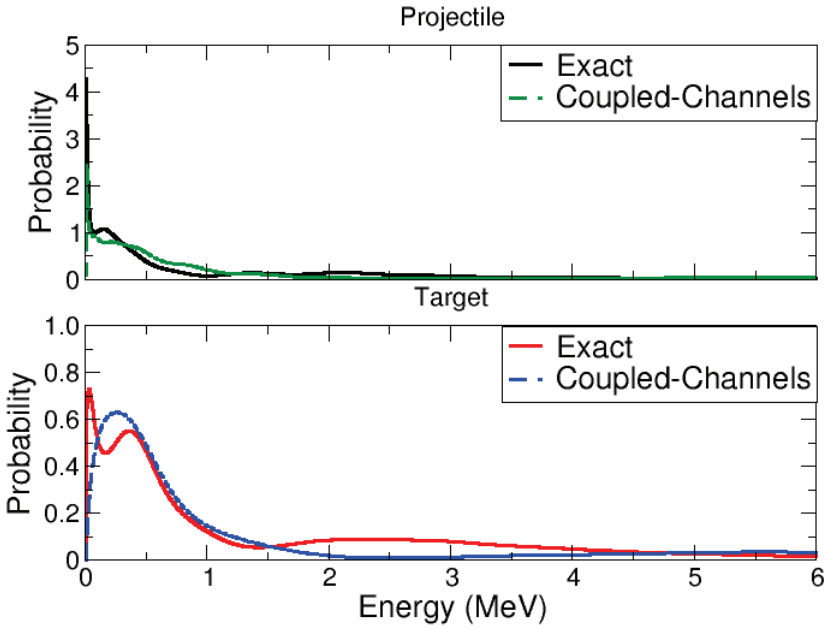

Figure 3.14: Same as in figure 3.13, but extended to higher excitation energies. The difference between exact and coupled-channels results around 2–3 MeV could depend on the handful number of continuum pseudostates included in the $\mathbf{CC}^{(3)}$ calculation and on the restricted range in which they are confined.

For high excitation energies (around $5 \div 6$ MeV) all the results follow the same trend, while for small energies they differ considerably. This could be the signature that the continuum reflects the structure of the corresponding potential well, for energies approching zero, thus indicating the importance to consider, if feasible, the continuum of all the possible subsystems of the outgoing particles.

To explain the sharp peak at low energy in the curves corresponding to the projectile, since for this model case we do not expect resonances[5], we suggest the presence of a virtual state in the projectile potential. We suppose that this virtual state influences also the exact wavefunction corresponding to breakup: looking at the exact wavefunction in figure 3.11f, one could claim that the part which follows the projectile during the evolution corresponds to

[5]See Appendix B.1 for further details.

transfer. Therefore, we think it is part of the breakup component due to the virtual state. As further check, we show in figure 3.15 a zoom of the central panel of figure 3.11f focusing on the exact wavefunction component above the projectile potential (green solid curve). The red dotted line is the result of the calculation presented in this section, in which we suggest the presence of the virtual state for the projectile. The blue dashed line is the result of a calculation in which the projectile potential well is made deep enough for the virtual state to become bound. As a final result, in this case, we obtain a total transfer probability of 17% (almost 12% to the ground state and 5% to the projectile first excited state). The wavefunction in the latter case is completely different respect to the one resulting from the former calculation (in which we suppose a transfer to a virtual state), and its shape reflects the combination of the transfer to the two projectile bound states. We refer to Appendix B.2 for more information about the virtual state.

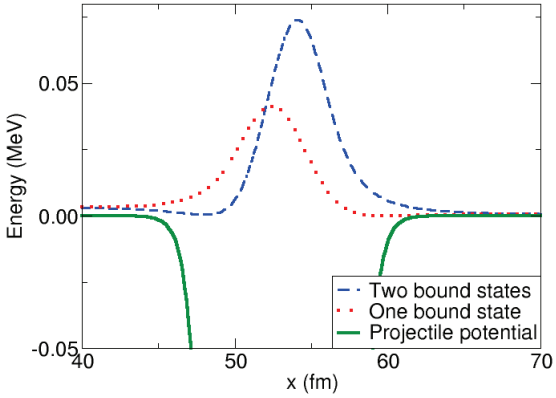

Figure 3.15: Comparison between the exact wavefunction of the central panel of figure 3.11f (red dotted line) and the one (blue dashed line) obtained with a deeper projectile well in order to get a second bound level. The green solid curve corrsponds to the projectile potential.

Finally, in table 3.4 we present the total breakup probability for the distributions presented in figure 3.13. As one can see, the exact and coupled-channels calculations for each well are in reasonable agreement. The fact that each well itself approaches the total breakup probability expected for this process could indicate that it is not appropriate to sum the distributions related to

the different wells to obtain the total breakup probability.

	Target	Projectile
Exact	66%	82%
Coupled-channels	56%	73%

Table 3.4: Probabilities of the breakup distributions presented in figure 3.13 for the model case B.

3.5.3 Case C

In the test case considered here, both the target and the projectile potential wells have two bound levels, as shown in figure 3.16. In this model case the projectile is moving following a fixed classical trajectory, like that presented in equation (3.2). Initially, the particle is sitting in the target ground state, and the projectile has a constant acceleration[6] of $4500/\hbar^2$ fm/ps^2. The reduced mass is 0.975 amu. The different configurations of the potentials during the time evolution and the squared wavefunction, are presented in figure 3.17.

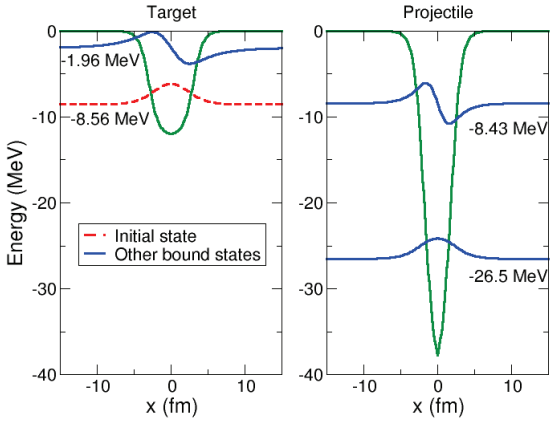

Figure 3.16: Taget (left) and projectile (right) Woods-Saxon potential and corresponding bound states for the model case C. The initial state, in this case the target ground state, is the dashed red curve.

[6]For this case the time is expressed in unit of $\hbar$.

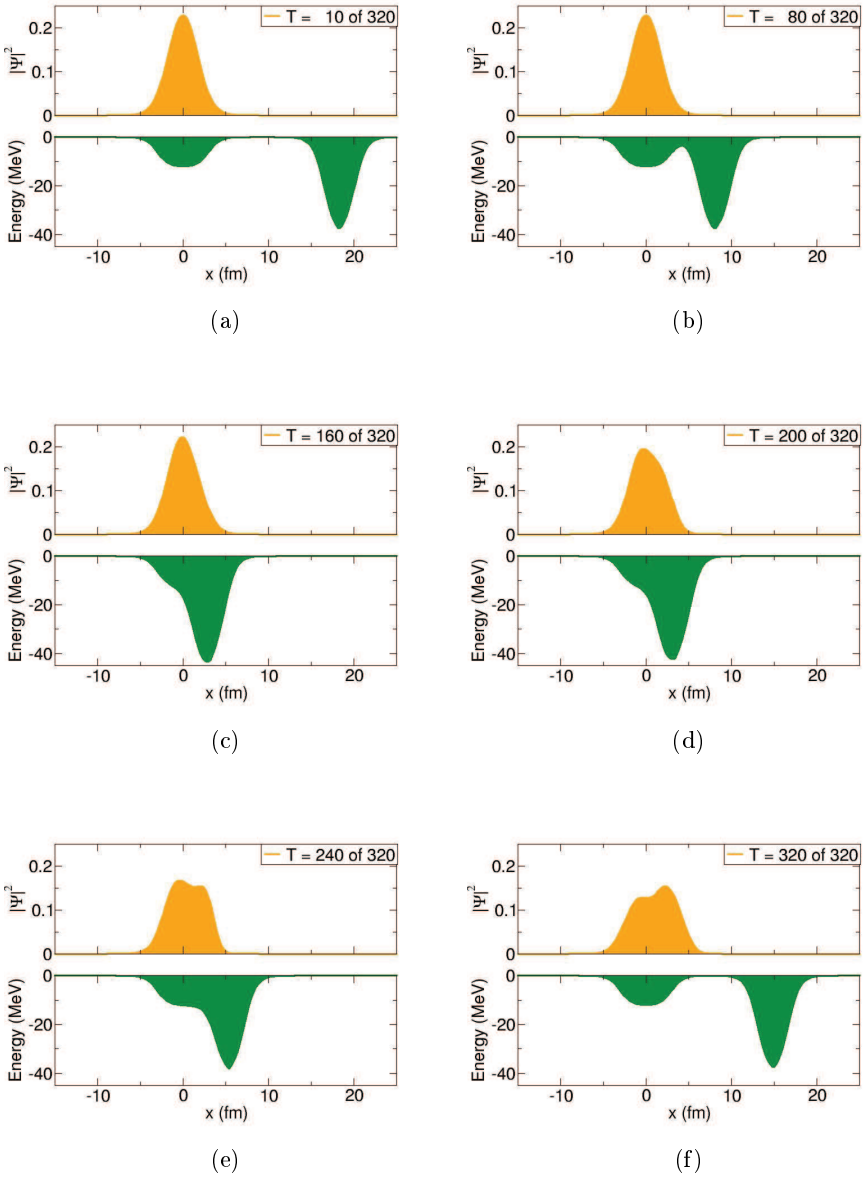

Figure 3.17: Model case C. Upper panels: the squared exact wavefunction at different times. Lower panels: the target and projectile potential wells. In the legends the time step is indicated for each frame.

As one can notice, the wavefunction changes clearly from the ground state (there are no nodes in the function in panel a) to a combination of the ground and first excited states. So we expect the system to scatter inelastically during this reaction. As can be seen from the results presented in table 3.5, there is also an important breakup component, which manifests as an asymmetric longer tail on the right side of the exact final wavefunction in figure 3.17f (around 8 fm).

	Exact	1^{st} o.a.	$CC^{(1)}$	$CC^{(2)}$
Elastic	65%	100%	73%	65%
Inelastic	22%	29%	27%	22%
Transfer g.s.	10^{-10}%	60%	-	-
Transfer 1	10^{-8}%	18%	-	-
Breakup	13%	-	-	13%

Table 3.5: Final probabilities for the model case C with the exact solution, coupled-channels method or first order approximation.

These results correspond to different calculations:

- **Exact** Calculation done by solving numerically the time dependent Schroedinger equation. The different results represent the probability for the valence neutron to remain in the ground state (Elastic) or to directly excite the target first excited state (Inelastic) or the projectile states (Transfer), or to excite continuum states (Breakup).
- **1^{st} o.a.** Calculation done by applying the first order approximation in a perturbaive approach.
- **$CC^{(1)}$** Coupled-channels calculation including only the target bound states.
- **$CC^{(2)}$** Coupled-channels calculation using the target bound levels plus the first 50 continuum pseudostates obtained with the BOX method with a radius equal to the maximum radius of the grid. It corresponds to an energy cutoff in the continuum of 17 MeV.

What one could expect from optimum Q-value considerations is a strong probability to transfer the neutron to the first excited state of projectile potential well $|\Phi_1^P\rangle$. Despite the fact that the Q-value for the transfer process

is optimum (i.e. $E_1^P - E_{g.s.}^T \sim 0$), this channel is not dominant for the exact result. Looking at the comparable form factors for transfer and inelastic processes presented in figure 3.18, we can have an explication of the first order approximation (**1st o.a.**) results for the transfer. To understand why the trasfer channel is suppressed, let us compare the caracteristic times of the process: if the collision time is of the same order of excitation time of a certain transition, that process is more likely to occur. The collision time for this reaction results to be of the order of $\tau_{collision} \sim 10^{-10}$ ps. The excitation time for a transition from the state $|\Phi_i\rangle$ to $|\Phi_f\rangle$ is $\tau = \hbar/(E_f - E_i)$. For the inelastic scattering the excitation time for this case is $\tau_{inelastic} \sim 10^{-10}$ ps, while for the transfer it results $\tau_{transfer} \sim 6 \cdot 10^{-9}$ ps. These results could explain why the excitation to the target first level state $|\Phi_1^T\rangle$ is favoured.

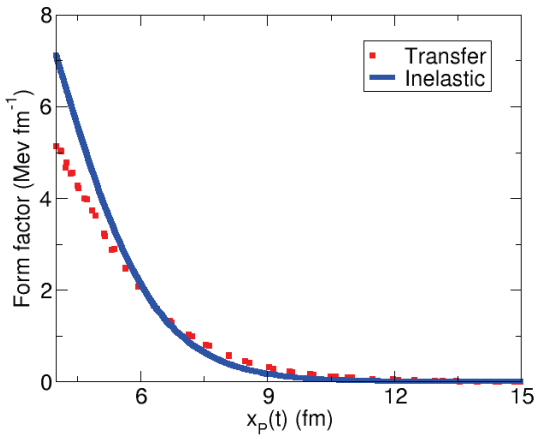

Figure 3.18: Form factors of the transfer (red dotted lines) to the projectile first excited state and inelastic (blu solid line) processes for model case C.

As one can see from table 3.5, the use of target bound states in the first order approximation (**1st o.a.**) or in the coupled-channels calculation (**CC**$^{(1)}$) is not enough to simulate properly the exact result. Only the inclusion of the target continuum in the calculation permits to describe perfectly the reaction (**CC**$^{(2)}$). In conclusion, by comparing approximate approaches with exact models, it emerges again how fundamental the inclusion of the continuum is to obtain the proper result expected from the "exact" calculation, even if the system is not so weakly bound.

3.5.4 Case D

Now we consider a case in which the dominat channels are elastic, transfer and breakup.

The target and projectile potentials are depicted in figure 3.19 with their respective bound states wavefunctions, the initial state is the dashed red curve corresponding to target ground state. In this case the projectile follows again the trajectory (3.3) with asymtotic velocity of $0.1 \times c$ corresponding to an incindet energy of 5.0 MeV, and with a reduced mass of 0.975 amu.

The evolution of the exact wavefunction during the collision is presented in figure 3.20, where in each frame the central panel shows the exact wavefunction and the lower displays the target and projectiles potentials. In the upper panels of figure 3.20 appears the current of the "exact" wavefunction calculated according to the expressions derived in Appendix D.3.

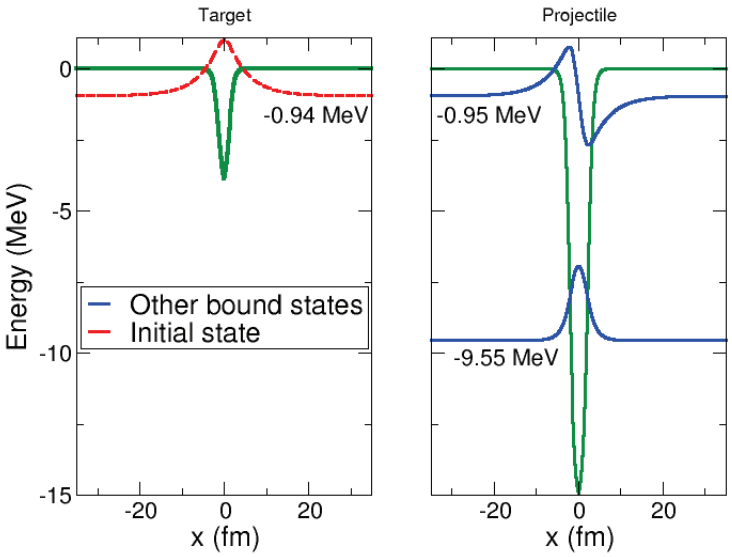

Figure 3.19: Taget (left) and projectile (right) Woods-Saxon potential and corresponding bound states for the model case D. The initial state, in this case the target ground state, is the dashed red curve.

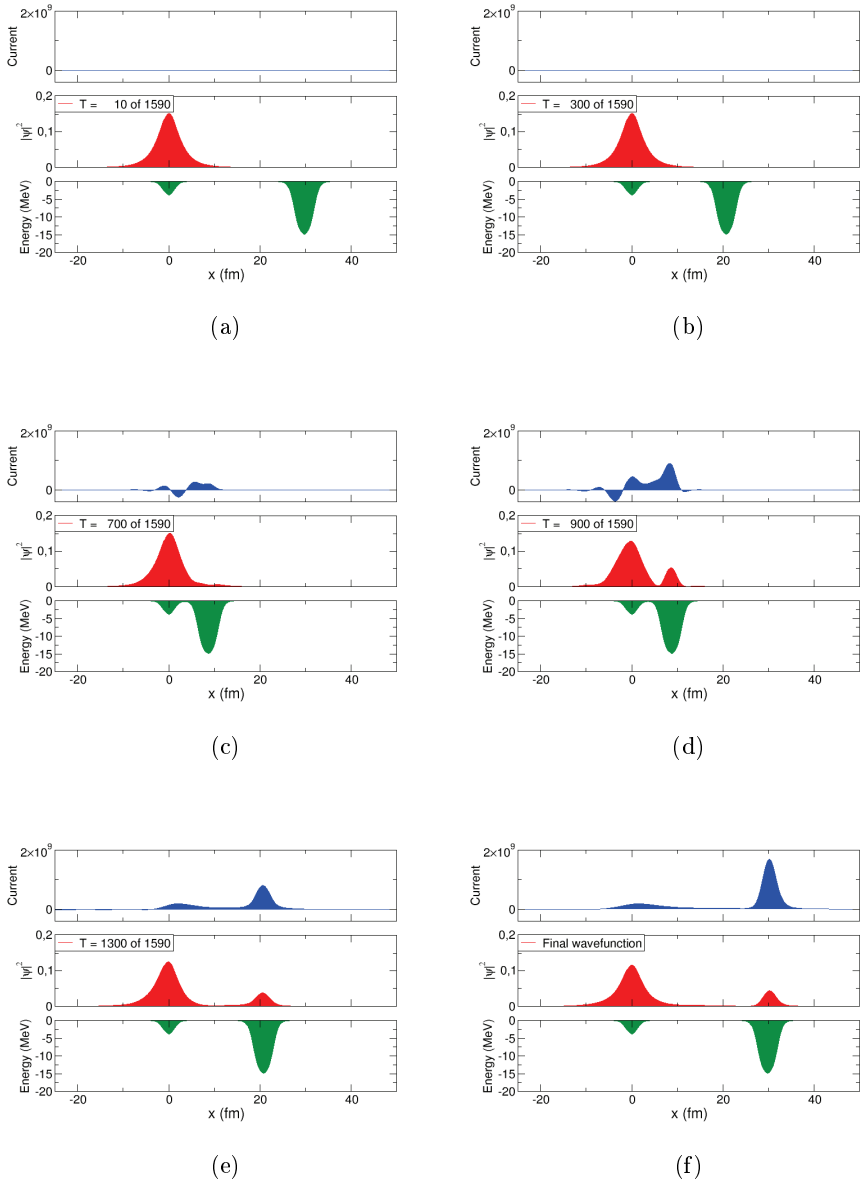

Figure 3.20: Model case D. Upper panels: the current of the wavefunction. Central panels: the squared total wavefunction at different times with exact method. Lower panel: the target and projectile potential wells. In the legends the elapsed time is indicated for each frame.

The results for this case are reported in table 3.6.

	Exact	1^{st} o.a.	$CC^{(1)}$	$CC^{(2)}$
Elastic	76.6%	100%	95.6%	78%
Transfer g.s.	7%	7.83%	4%	7.7%
Transfer 1	3.4%	15.2%	0.4%	2.7%
Breakup	13%	-	-	$\gtrsim 12\%$

Table 3.6: Final probabilities for the model case D with the exact method, the coupled-channels method and the first order approximation.

These results correspond to different calculations:

- **Exact** Calculation done by solving numerically the time dependent Schroedinger equation.
- **1^{st} o.a.** Calculation done by applying the first order approximation in a perturbaive approach.
- **$CC^{(1)}$** Coupled-channels calculation including only the target and projectile bound states.
- **$CC^{(2)}$** Coupled-channels calculation using the target and projectile bound levels plus the first 5 target continuum pseudostates obtained with the BOX method within a radius of 25 fm. It corresponds to an energy cutoff in the continuum of 3 MeV.

Note that the first order approximation (**1^{st} o.a.**) works quite well since we are almost in the perturbative regime (most of the flux remains in the elastic channel). The application of the coupled-channels method, retaining only the bound states of the two potentials (**$CC^{(1)}$**), is not enough to reproduce the exact results. By including five states of the target continuum (**$CC^{(2)}$**) we manage to reproduce quite well elastic and transfer channels. Breakup channel exceeds the expected value, thus bringing the total probability to more than 100%. This meens that the projectile has not gone sufficiently far from the target at the end of the calculation. Unfortunately, to let the projectile go further or to consider any other configuration for the continuum do not solve the unitary problem, since the calculation becomes numerically unstable. Anyway, from the "exact" wavefunction and above all the current evolution presented in figure 3.20, we can deduce that the breakup continuum

is not so significant, because it is almost negligible with respect to the other components.

3.5.5 Case E

We treat now a case in which all the possible channels are relevant: elastic and inelastic scattering, transfer and breakup. The target and projectile potentials are depicted in figure 3.21 with their respective bound states wavefunctions. The initial state is the dashed red curve corresponding to target first excited state. In this case the projectile follows again the trajectory (3.3) with asymtotic velocity of $0.05 \times c$ corresponding to an incident energy of 1.0 MeV, and with a reduced mass of 0.975 amu.
The evolution of the exact wavefunction during the collision is presented in figure 3.22, where in each frame the central panel shows the exact wavefunction and the lower displays the target and projectiles potentials. In the upper panels of figure 3.22 appears the current of the "exact" wavefunction calculated according to the expressions derived in Appendix D.3.

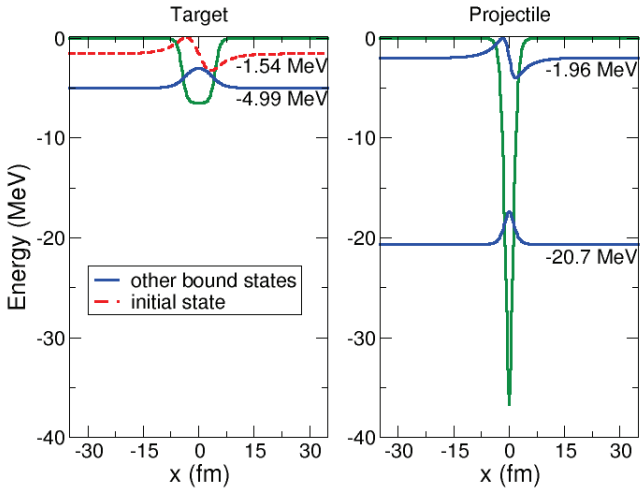

Figure 3.21: Taget (left) and projectile (right) Woods-Saxon potential and corresponding bound states for the model case E. The initial state, in this case the target ground state, is the dashed red curve.

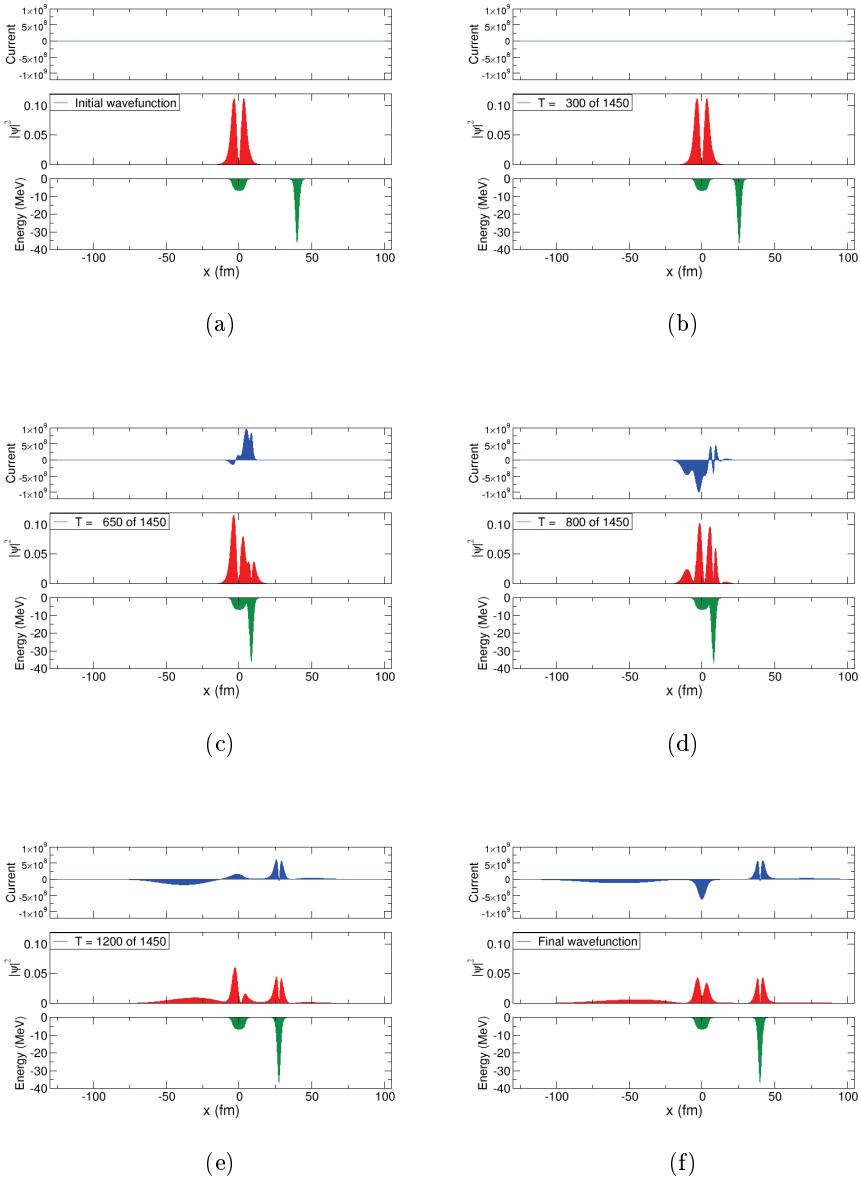

Figure 3.22: Model case E. Upper panels: the current of the wavefunction. Central panels: the squared total wavefunction at different times with exact method. Lower panels: the target and projectile potential wells. In the legends the elapsed time is indicated for each frame.

The results for this case are reported in table 3.7.

	Exact	1^{st} o.a.	$CC^{(1)}$	$CC^{(2)}$
Inelastic	6.7%	103%	16%	3%
Elastic	29%	100%	10%	84%
Transfer g.s.	1.2%	10^{-4}%	0.6%	0.04%
Transfer 1	15.6%	$\gg$100%	36%	0.2%
Breakup	47.5%	-	44%	20%

Table 3.7: Final probabilities for the model case E obtained with the exact method, the coupled-channels method and the first order approximation. Note that $CC^{(1)}$ and $CC^{(2)}$ total probability exceeds 100%, as expected.

These results correspond to different calculations:

- **Exact** Calculation done by solving numerically the time dependent Schroedinger equation.
- **1^{st} o.a.** Calculation done by applying the first order approximation in a perturbaive approach.
- **$CC^{(1)}$** Coupled-channels calculation using the target and projectile bound levels plus the first 10 continuum pseudostates of the target potential, obtained with the BOX method with a radius equal to the maximum radius of the grid. It corresponds to an energy cutoff in the continuum of 0.3 MeV.
- **$CC^{(2)}$** Coupled-channels calculation using the target and projectile bound levels plus the first 10 continuum pseudostates of the projectile potential, obtained with the BOX method with a radius equal to the maximum radius of the grid. It corresponds to an energy cutoff in the continuum of 0.3 MeV.

In this case in which all the reaction channels are relevant, we expect the first order perturbative approach (**1^{st} o.a.**) to fail. We also have difficulties to apply the same method for the inclusion of continuum in coupled-channels calculation, as in previous cases. In case B the breakup component did not escaped quickly from the collision area, so at the end of the time evolution it was localized around the target in an interval that did not overlap with the projectile potential. This fact allowed us to construct two bases, for

target and projectile respectively, which did not overlap at the end of the calculation, thus restoring the probability unitarity. In case C the initial parameters were set in order to give a very small transfer probability to the projectile states, thus the inclusion of target states was enough to reproduce the exact results. Case D is more similar to case E under study, because all channels are rather relevant to the reaction. The difference of case D is that breakup had a smaller influence and so we were able to describe quite well all the other channels even with a result which slightly exceeded unitarity. In the case under study, the breakup channel has a strong influence and its component is not easily localizable onto the space grid, because it is travelling faster than the projectile. What we propose here is to use continuum states which are defined along all the spatial range. This is certainly closer to what the real continuum is, but surely will led to a not unitary solution, because of overlap between bound states of a potential well and continuum pseudostates of the other. By including few target continuum states ($\mathbf{CC}^{(1)}$), e.g. 10 pseudostates, the deviation of unitarity is not so big, and we are still able to reproduce all the reaction channels. The fact that the inclusion of projectile pseudostates ($\mathbf{CC}^{(2)}$) does not reproduce the exact results tells us that the breakup component is mostly influenced by the target potential. In fact from the wavefunction current in upper panels of figure 3.22 it is apparent that the breakup component is traveling towards the left of the target.

Since the projectile well is moving, the overlap between pseudostates and bound states is changing, so we do not expect the coefficients associated to continuum pseudostates to converge to a fixed value. What we find is that those coefficients tend to oscillate around the exact result.

In figure 3.23 we show how the probability for the $\mathbf{CC}^{(1)}$ calculation changes with time during the reaction. Each panel corresponds to a given reaction channel; from the lowest: inelastic (green), elastic (blue), transfer to projectile ground state (red), transfer to projectile first excited state (orange), and breakup to continuum (black). The comparison of the exact result (solid lines) with the $\mathbf{CC}^{(1)}$ result (dotted lines) are presented. Note how the coupled-channels results clearly lose unitarity close to the turning point at $t = 0$ ps.

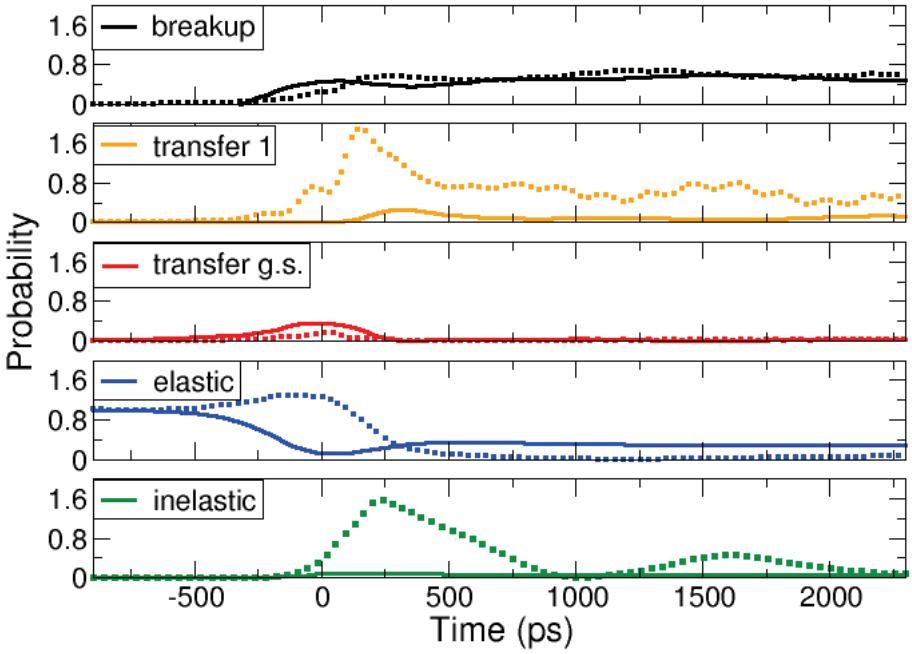

Figure 3.23: Evolution of probability as a function of time for the model case E. Each panel corresponds to a reaction channel indicated in the corresponding legend. Solid lines represent the exact results, dotted lines correspond to the results obtained with coupled-channels calculation $CC^{(1)}$ which are reported in table 3.7.

Chapter 4

Two-neutron halo systems: structure and dynamics

After having investigated the one-body problem, we proceed to a more complicated, and physically more enlightening, two-body halo system. Our schematic model in this case consists of a fully occupied Woods-Saxon core plus two particles outside the core interacting via a matter density-dependent point contact residual interaction. As anticipated in the introduction of this memory, our goal with this choice is to model a simplified (1D) Borromean nucleus, i.e. a system with a two-particle halo which is bound notwithstanding the possible core plus one particle subsystem is unbound.
The two-body structure model is summarized in section 4.1, where we also present the results for the system eigenvalues and eigenvectors and the role of the pairing interaction between the two nucleons in binding the system (4.1.1), and other quantities of physical interest such as anomalous density and electric transitions (4.1.2 and 4.1.3). We then describe scattering process of the two-body system in the field of two potential wells in section 4.2, and we study the influence of the binding energy and pairing interaction in the reaction mechanism (4.2.1 and 4.2.2).

4.1 Bound and unbound states of two particles in a mean field

We describe here the structure of the two-body system composed by an inert core and a two-body halo. This problem consists of two valence particles moving in a one-dimensional Woods-Saxon potential (2.1) representing the mean field generated by the other nucleons, i.e. the core, whose bound levels are assumed to be completely filled. The two valece particles, which we assume to be neutrons, interact via a density-dependent short-range attractive residual interaction

$$V_{int}(x_1, x_2) = V_0\delta(x_1 - x_2) - V_{RI}\left[\frac{\rho[(x_1 + x_2)/2]}{\rho_0}\right]^p \delta(x_1 - x_2), \qquad (4.1)$$

where V_0, V_{RI}, p, and ρ_0 are parameters, and $\rho(x)$ is the core matter density[1]

$$\rho(x) = \sum_{i=0}^{N_b-1} \psi_i^*(x)\psi_i(x), \qquad (4.2)$$

where N_b is the number of occupied bound states. The residual interaction parameter values selected for the structure results are as follows

$$V_0 = 0.0 \text{ MeV}, \qquad V_{RI} = -38.0 \text{ MeV}, \qquad (4.3)$$
$$\rho_0 = 0.15 \text{ fm}^{-1}, \qquad p = 1.$$

So, we assume that the volume term V_0 is zero and we only deal with the matter density weighted term.

Since we model a drip line system, we have chosen the Fermi surface in such a way that there are no available bound states, so the two valence particles must lie in the continuum. The final two-body state becomes bound due to the action of the residual interaction between the two particles, akin to a 1D "Borromean" system. Thus, the two-body Hamiltonian H_{2b} is built combining the one-body Hamiltonian[2] (2.1) with the residual interaction

[1] The formulation of this problem has been introduced and presented in [62] for the 3D case. Note that in our 1D reduction for a symmetric potential the core density (4.2) is a symmetric function of x.

[2] We use a reduced mass of $\mu = 0.975$ amu and the same Woods-Saxon potential (2.1) parameters used for the model case of chapter 2: $V_0 = -50.00$ MeV, $R = 2.00$ fm, and $\alpha = 0.40$ fm.

(4.1)

$$H_{2b}(x_1, x_2) = H_{1b}(x_1) + H_{1b}(x_2) + V_{int}(x_1, x_2). \tag{4.4}$$

Our strategy is to diagonalize the two-body Hamiltonian (4.4) in a two-body basis built with states that are above the Fermi energy surface. We proceed to detail the basis construction following [62]. The full 1D one-body wave function has two components, a spatial part and a spinor part

$$\Psi^{(1b)}_{n,m_s}(x) = \psi_n(x)\chi^{(s)}_{m_s}, \tag{4.5}$$

where the one-body spatial component has been previously obtained using any of the methods presented in Chapter 2.

The two-body basis can be constructed involving products of one-body wave functions to obtain

$$\Psi^{(2b)}_{n_1,n_2,S,m_S}(x_1, x_2) = \psi_{n_1}(x_1)\psi_{n_2}(x_2) \times \sum_{m_{s_1},m_{s_2}} \langle s_1 m_{s_1} s_2 m_{s_2} | s_1 s_2 S m_S\rangle \chi^{(s_1)}_{m_{s_1}} \chi^{(s_2)}_{m_{s_2}}. \tag{4.6}$$

Assuming that we are dealing with fermions, the full wave function (4.6) should be antisymmetric under the interchange of the labels 1 and 2. Thus, if we consider the singlet $S = 0$ wavefunction, the spin wave functions are antisymmetric[3]

$$\Psi^{(2b)}_{n_1,n_2,0,0}(x_1, x_2) = \psi_{n_1}(x_1)\psi_{n_2}(x_2)\left[\frac{1}{\sqrt{2}}\left(\chi^{(1/2)}_{1/2}\chi^{(1/2)}_{-1/2} - \chi^{(1/2)}_{-1/2}\chi^{(1/2)}_{1/2}\right)\right]. \tag{4.7}$$

The spatial part should be symmetrized, and the dimension of the problem for N one-body spatial wave functions goes down from N^2 to $N(N+1)/2$ for the symmetric two-body spatial wave functions $\psi^{(2b)}_{n_1,n_2}(x_1, x_2)$,

$$\psi^{(2b)}_{n_1,n_2}(x_1, x_2) = \frac{\sqrt{2 - \delta_{n_1,n_2}}}{2}\left[\psi_{n_1}(x_1)\psi_{n_2}(x_2) + \psi_{n_2}(x_1)\psi_{n_1}(x_2)\right], \tag{4.8}$$

or, using the ket notation,

$$\psi^{(2b)}_{n_1,n_2}(x_1, x_2) \to |(s)n_1 n_2\rangle = \frac{\sqrt{2 - \delta_{n_1,n_2}}}{2}\left(|n_1 n_2\rangle + |n_2 n_1\rangle\right). \tag{4.9}$$

[3]The triplet contribution of the spin can be considered when the spatial part can be antisymmetrized, thus the interaction should not be of a contact type and $x_1 \neq x_2$.

The matrix elements of the Hamiltonian (4.4) in the symmetrized basis are

$$\langle (s)n_1'n_2'|H_{2b}|(s)n_1n_2\rangle = \frac{\sqrt{(2-\delta_{n_1,n_2})(2-\delta_{n_1',n_2'})}}{2}(E_{n_1}+E_{n_2}) \times(\delta_{n_1,n_1'}\delta_{n_2,n_2'}+\delta_{n_1,n_2'}\delta_{n_2,n_1'})+\langle (s)n_1'n_2'|V_{int}|(s)n_1n_2\rangle, \tag{4.10}$$

where the matrix element of the residual interaction is

$$\langle (s)n_1'n_2'|V_{int}|(s)n_1n_2\rangle = -V_{RI}\sqrt{(2-\delta_{n_1',n_2'})(2-\delta_{n_1,n_2})} \times\int_{-\infty}^{+\infty} dx\,\psi^*_{n_1'}(x)\psi^*_{n_2'}(x)\left[\frac{\rho(x)}{\rho_0}\right]^p\psi_{n_1}(x)\psi_{n_2}(x). \tag{4.11}$$

As the core density (4.2) is symmetric, the integrand has to be a symmetric function too, which implies the selection rule

$$n_1+n_2+n_1'+n_2'=2n; \quad n=0,1,2,\ldots \tag{4.12}$$

As we are dealing with a contact interaction, it is important to define an energy threshold, $E_{th} = 50.0$ MeV, beyond which the two-body basis components are not taken into account. Thus, only basis states $|(s)n_1n_2\rangle$ such that $E_{n_1}+E_{n_2} \leq E_{th}$ will enter into the calculation. This energy cutoff is due to the special characteristics of the point contact interaction that forbid convergence when the full space is considered [62].

For each of the considered discretized bases (HO, THO, BOX) we solve the one-body problem (2.28) to obtain a set of bound states and a set of pseudostates representing the continuum. Then, using the positive-energy pseudostates, the Fermi-allowed two-body basis is built and the two-body Hamiltonian (4.4) is diagonalized, computing the matrix elements (4.10). This second part is common to all methods. As a result of the two-body structure model we study the eigenenergies and the eigenfunctions resulting from this diagonalization method.

4.1.1 Energies and wavefunctions of the two-body model

As in the one-body case, we investigate the convergence of the bound state eigenvalues and their corresponding wave functions. A proper behavior in the tail region is essential in the description of two-particle transfer processes in connection with the pairing field. We should emphasize that, in comparison

with the one-body case, the treatment of this case is a more complicated task, since it implies much larger bases. In order to give an idea of the increased complexity of the problem we plot in figure 4.1 the dependence of the two-body symmetrized basis dimension as a function of the one-body basis dimension. As discussed in chapter 2, the $\gamma/b = 2.4$ fm$^{-1/2}$ THO case behaves in a similar way to the HO, and variation of γ/b gives us an extra degree of freedom in the investigation of the system.

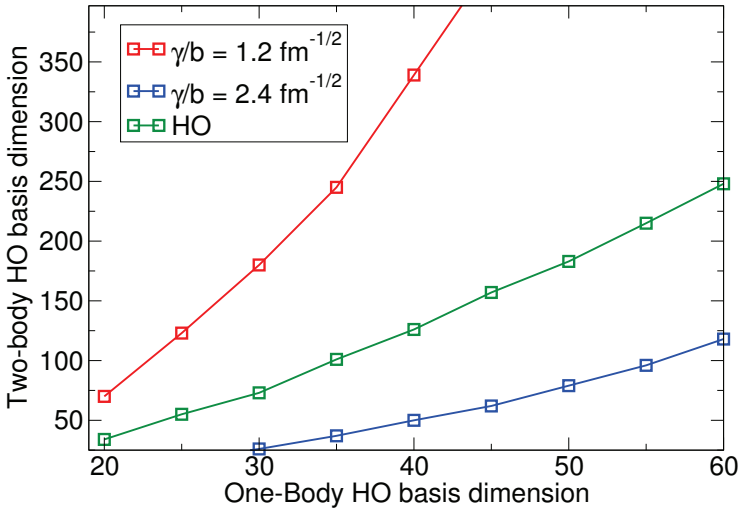

Figure 4.1: Two-body basis dimension as a function of the one-body basis dimension for the HO (green) and THO methods (using $\gamma/b = 2.4$ fm$^{-1/2}$, blue, and $\gamma/b = 2.4$ fm$^{-1/2}$, red).

Despite that, the description of the one-body bound states obtained in chapter 2 is quite accurate even for a small basis dimension. Therefore the residual interaction is not expected to vary with N. This can be checked in figure 4.2 where the resulting residual interaction $-V_{RI}[\rho(x)/\rho_0]^p$ is plotted for the HO, THO and BOX cases: there are some differences between the three cases, which can be significant for large values of x, in the tail region.

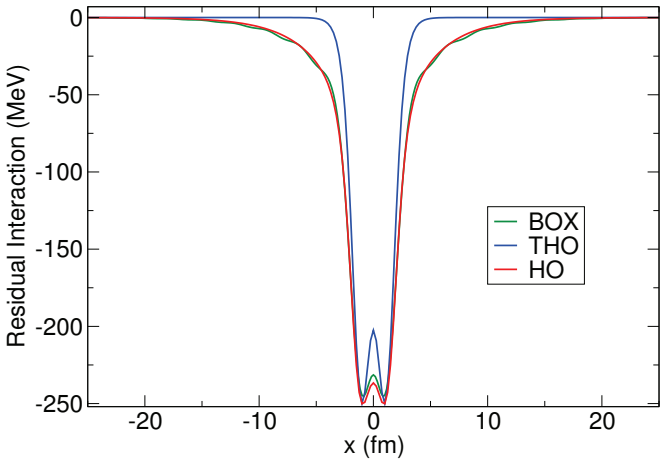

Figure 4.2: Spatial dependence of the residual interaction for parameters in Eq. 4.4 for the HO ($N = 70$), THO($\gamma/b = 1.2fm^{-1/2}$ and $N = 50$), and BOX ($x_b = 50fm$) cases.

In the first place we check the dependence of the resulting two-body Hamiltonian eigenvalues with the dimension of the truncated 1D basis. This is depicted in figures 4.3a and 4.3b for the HO and THO methods, respectively, while for the BOX method the dependence on the box radius is shown in figure 4.3c. As can be seen from those figures, the energy of the bound state (red solid line) is converging, with residual minor oscillations, to a limiting value $E_b = -0.5$ MeV. Note that without the residual interaction the two-body system is unbound, and it is the attractive residual interaction between the two valence neutrons that makes the system bound. To show the quantitative effect of the residual interaction, we also depict in figure 4.3, as a dashed green line, the energy of the lowest unperturbed two-particle state for each value of the parameter N or x_b. The dotted blue lines are the energies of the lower two-particle pseudostates in the continuum arising from the diagonalization. As in the one-body case, the convergence is faster with respect to N for the THO case as compared to the simpler HO case.
As in the one-body case it is important to check also the radial behavior of the bound eigenstate. To this end the resulting ground-state wave function $\Psi(x, x)$ for $x_1 = x_2 = x$ is plotted in the right panels of figure 4.3 for different N values in the HO and THO cases or x_b for the BOX. In order to display the slow convergence in the tail region, we show in the figure just the asymptotic part of the wave functions in a logarithmic scale.

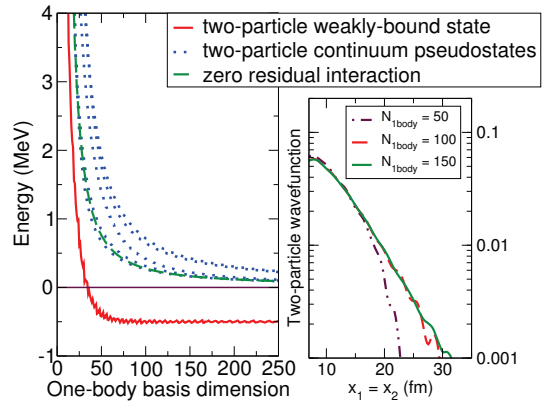

(a) HO

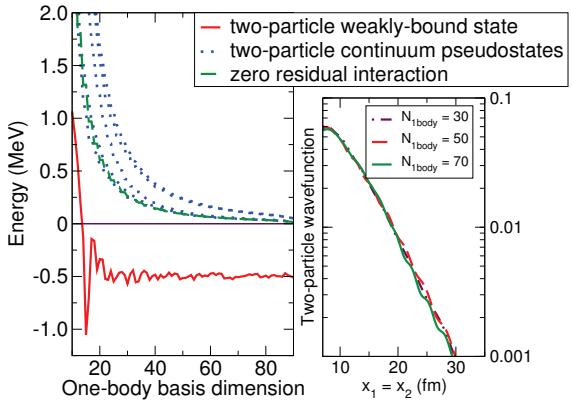

(b) THO

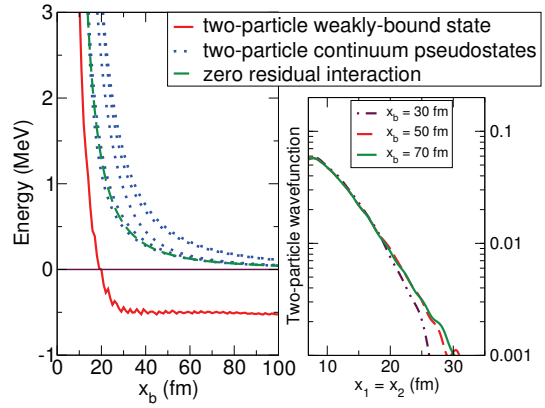

(c) BOX

Figure 4.3: Panel (a): first two-body Hamiltonian energies (solid red and dotted blue lines) as a function of the dimension of the truncated 1D HO basis (left) and ground state wavefunction tail $\Psi(x,x)$ for different values of the one-body basis dimension (right). Panel (b): same for the THO basis. Panel (c): first two-body Hamiltonian energies as a function of the radius x_b of the BOX (left) and ground-state wavefunction tail $\Psi(x,x)$ for different values of the box radius (right). Also shown, as dashed green lines, the energies of the lowest unperturbed two-particle state for each value of the parameter N or x_b.

A further insight on the effect of the residual pairing correlations can be obtained by looking at the features of the wave function (or its modulus squared) as a function of the coordinates x_1 and x_2. The results obtained for the correlated two-particle ground state are displayed in figure 4.4 and should be compared with the uncorrelated case displayed in figure 4.5. In order to better pinpoint the effect of correlations we define an uncorrelated case with zero residual interaction, but with a mean field providing a two-particle uncorrelated wave function with the same total binding energy (-0.5 MeV) as the final correlated one. It is apparent from the comparison of the two figures that the residual interaction has created a spatial correlation between the two particles, proved by an increased probability along the bisector line $x_1 = x_2$, i. e. for small relative distances. On the contrary, the uncorrelated wave functions looks completely symmetric in the four quadrants, implying that the probability is not favoured for small relative distances.

The enhanced spatial correlation in the correlated case can be even better appreciated by cutting the wavefunctions presented in figures 4.4 and 4.5 along the $x_1 = x_2$ bisector. Correlated and uncorrelated sections are compared in figure 4.6, showing the strong enhancement in the correlated case. This enhancement will manifest as an increased probability for two-particle transfer, two-particle breakup or knock-out processes, with strong angular correlation between the two emitted particles in the two latter cases [44]. We can note that all discretization methods provide similar results, although again the number N of shells required to get convergence in THO is smaller than in HO.

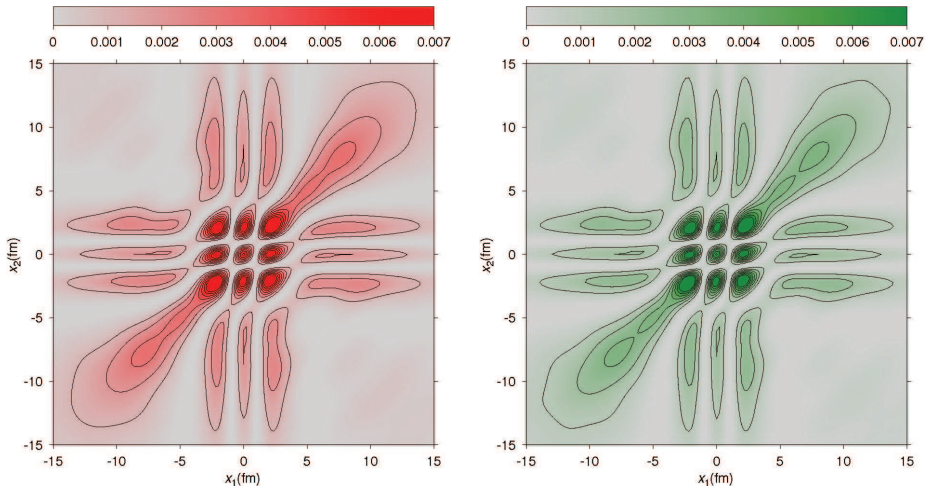

(a) HO (b) THO

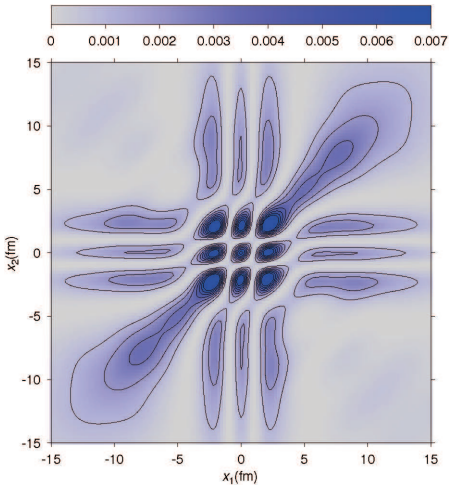

(c) BOX

Figure 4.4: Contour plots of the probability density for the two-body bound state with binding energy $E = -0.5$ MeV using the correlated Hamiltonian (4.4) constructed with different bases: HO with $N = 200$ in panel (a), THO with $\gamma/b = 1.2\,\mathrm{fm}^{-1/2}$ and $N = 75$ in panel (b), and a BOX with $x_b = 100$ fm in panel (c).

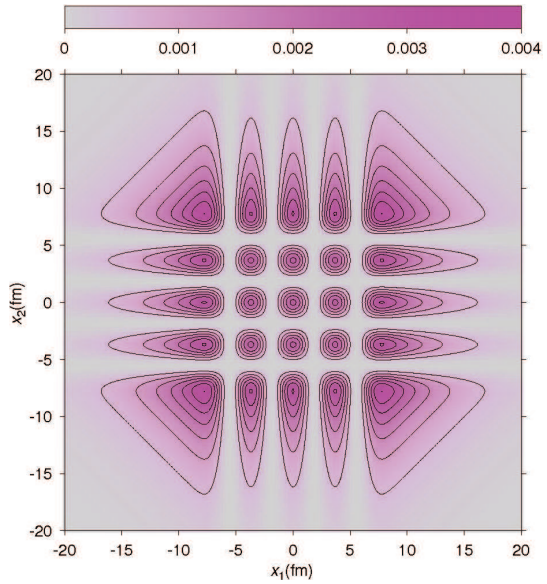

Figure 4.5: Same than figure 4.4, but for the wave function obtained with an uncorrelated Hamiltonian (zero residual interaction), with a single particle potential depth modified to obtain for the two-particle system the same binding energy as in the correlated case ($E = -0.5$ MeV).

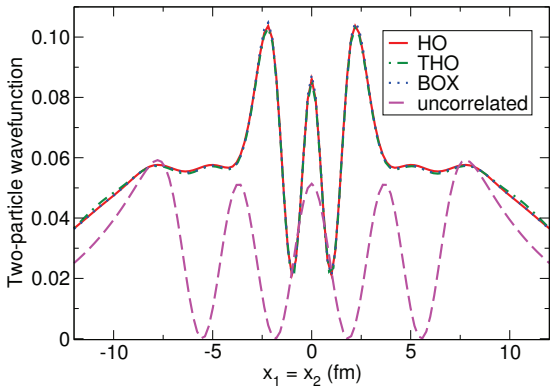

Figure 4.6: Two-body bound state along the $x_1 = x_2$ bisector for the correlated and uncorrelated cases presented in figures 4.4 and 4.5.

4.1.2 Anomalous Density

To test the structure model, as in the one-body case, several quantities of interest can be investigated. We obtain here the anomalous density for the ground two-body state and first continuum states. The anomalous density T_0 is defined as follows [63]

$$T_0 = \left| \int_{-\infty}^{+\infty} dx\, \delta\rho_{pair}(x) \right|^2 , \tag{4.13}$$

where, using the creator operator notation, $\int dx\, \delta\rho_{pair}(x) = \langle A+2|a^\dagger a^\dagger|A\rangle$, and thus

$$\delta\rho_{pair}(x) = \sum_{i_1,i_2} X_{i_1,i_2} \phi_{i_1}(x)\phi_{i_2}(x) \ . \tag{4.14}$$

The coefficients X_{i_1,i_2} are obtained by diagonalization of the Hamiltonian (4.4). Large values of the anomalous density imply a collective character of the state under study, and its evaluation implies the integration of the two-body eigenfunction in points $x_1 = x_2 = x$, depicted in the right panels of figure 4.3.

It is interesting to note that, due to the orthonormality of the one-body basis functions $\phi_i(x)$, the anomalous density can be written as

$$T_0 = \left| \sum_i X_{i,i} \right|^2 , \tag{4.15}$$

which implied that only the eigenvector components associated to the $|(s)nn\rangle$ basis states should be taken into account.

Anomalous density values can also be computed for the excited two-body pseudostates. We will use the notation $T_0^{(i)}$ for the anomalous density for the i-th two-body excited state where equation (4.14) is redefined as

$$\delta\rho^{(i)}_{pair}(x) = \sum_{i_1,i_2} X^{(i)}_{i_1,i_2} \phi_{i_1}(x)\phi_{i_2}(x) \ , \tag{4.16}$$

where $X^{(i)}_{i_1,i_2}$ are the coefficients for the i-th excited state obtained by diagonalization of the Hamiltonian. As in the ground state case, taking into account the basis orthonormality in the integral evaluation the anomalous

density can be rewritten as

$$T_0^{(i)} = \left| \sum_k X_{k,k}^{(i)} \right|^2 . \tag{4.17}$$

Anomalous Density results presented in figure 4.7 for HO, THO, and BOX agree satisfactory. Moreover, the enhanced result associated to the two-body system ground state indicates, as expected, the collective character of this state.

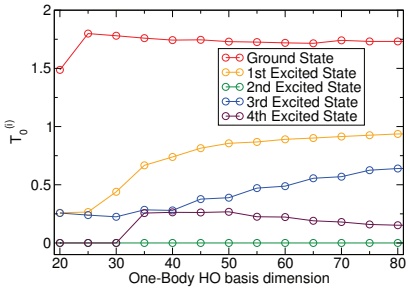

(a) HO

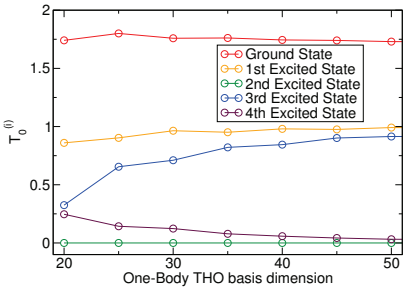

(b) THO

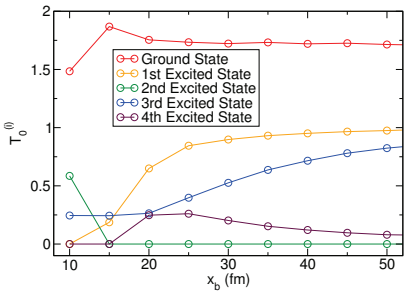

(c) BOX

Figure 4.7: The Anomalous Density result for the HO (a) and THO (b) for $\gamma/b = 1.2$ fm$^{-1/2}$ as a function of the one-body basis dinension N. The BOX method result (c) is presented as a function of the box radius x_b.

4.1.3 Transition matrix elements for x and x^2 operators

The knowledge of the ground and excited two-particle states allows us to calculate matrix elements of different operators, e.g. x and x^2, between the ground state and all "continuum" excited states. Besides checking the different discretization methods, one can compare the energy strength distribution with those obtained within the di-neutron cluster model.

We start by extending the x and x^2 operators to the two-particle case. Defining

$$D_{12} = x_1 + x_2, \tag{4.18}$$

$$Q_{12} = x_1^2 + x_2^2, \tag{4.19}$$

we compute the transition integrals

$$\langle \Psi_b | \mathcal{O}(x_1, x_2) | \Psi_i \rangle = \int_{-\infty}^{+\infty} dx_1 dx_2 \; \Psi_b^*(x_1, x_2) \mathcal{O}(x_1, x_2) \Psi_i(x_1, x_2), \tag{4.20}$$

where $\mathcal{O}(x_1, x_2) = D_{12}$ or Q_{12}, $\Psi_b(x_1, x_2)$ is the two-body ground state, and the set $\{|\Psi_i(x_1, x_2)\rangle\}$ represents the two-body continuum pseudostates.

The resultant distribution of modulus squared matrix elements from the ground state to continuum states is reported in figure 4.8 for the different discretization methods and for different values of N (HO and THO) or x_b (BOX). Upper frames refer to $B_1 = |\langle \Psi_b | D_{12} | \Psi_i \rangle|^2$, and lower frames to $B_2 = |\langle \Psi_b | Q_{12} | \Psi_i \rangle|^2$. Since the different calculations lead to different densities of states, for a better comparison of the convergence properties we also display in the legends of the figure the integrated values.

It would be natural trying to interprete the above results in terms of sum rules. This is more complex in the case of the TSSR, see (2.48), since it would require the evaluation of the expectation value of $x_1 x_2$ operator. It is, on the other hand, easier to evaluate the EWSR: in an A-body system, for one-body operators, it can be calculated as

$$\mathcal{E}_W^{(b)}(x_1, ..., x_A) = \frac{1}{2} \frac{\hbar^2}{\mu} \langle \Psi_b | \sum_{i=1}^{A} \left(\frac{\partial \mathcal{O}(x_i)}{\partial x_i} \right)^2 | \Psi_b \rangle. \tag{4.21}$$

The fulfillment of the EWSR is an indication of the goodness of the dis-

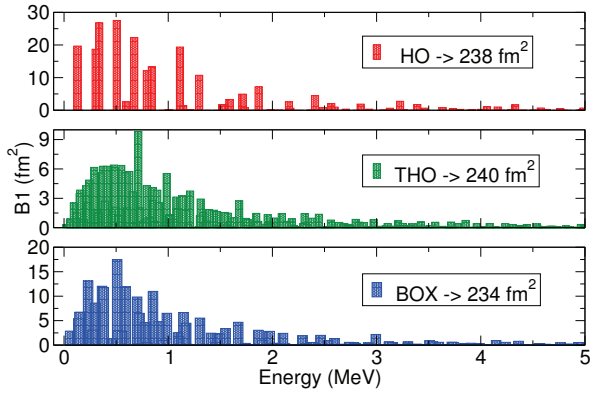

(a) B1

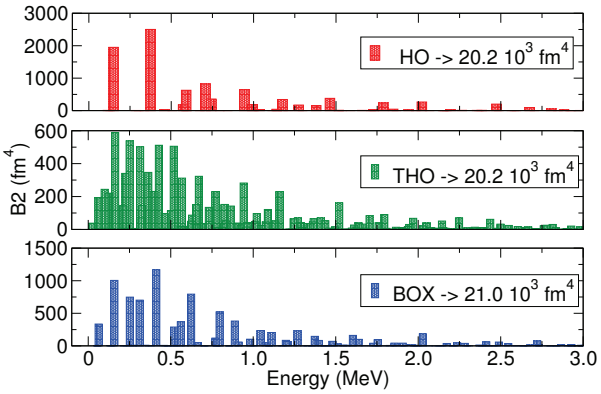

(b) B2

Figure 4.8: Results for the B_1 and B_2 transition intensities in the microscopic two-body approach as a function of the excitation energy, using the different discretization methods. Numbers in each panel legend are the integrated values. In the HO case the basis dimension is N= 200, in the THO case N= 100, and for the BOX case the radius is $x_b = 90$ fm.

cretization method, but also of the completeness of the basis, as stated for the one-body case in chapter 2. The EWSR value is in fact only recovered when a complete basis is used, which is not our case. Since we are dealing with a delta function, we truncate all bases up to a certain energy. Since the values of the transition matrix elements are rapidly decreasing (cf. figure 4.8) we may assume that the cut-off is not so relevant. However, it is much more important that in our model we have assumed a saturated and frozen core: states that correspond to both particles in a "forbidden" bound state or states which represent combinations of one particle in a core state and another in a one-body continuum state have not been included in the two-body basis. For this reason the comparison with the EWSR for the two-body case is beyond our simple approach.

We conclude this section by comparing the results obtained in the two-body model with the corresponding distribution of matrix elements obtained within the di-neutron cluster model [64]. To this end we have considered a 1D cluster of two neutrons with mass $\mu = 1.885$ amu moving in a potential (2.1) defined in such a way to reproduce the same binding energy (E= -0.50 MeV) and quantum numbers of the two-body model case:

$$V_0 = -50.9 \text{ MeV}, \qquad R = 5.0 \text{ fm}, \qquad \alpha = 0.4 \text{ fm}. \tag{4.22}$$

In this case the transition intensities to continuum are calculated with a one-body operator x_{clus}, the c.m. coordinate of the cluster, and the basis states are single-particle bound and pseudo states $\{|\Phi_i\rangle\}$ generated by the "cluster" potential. In the lower panel of figure 4.9 we present the cluster response $B_1 = |\langle\Phi_b|x_{clus}|\Phi_i\rangle|^2$ with the corresponding two-body calculations $B_1 = |\langle\Psi_b|x_1 + x_2|\Psi_i\rangle|^2$. For this comparison we have chosen THO results with N= 100 for the "microscopic" case and N= 200 for the cluster case. The two distributions have the same shape but, apart from a different normalization factor, the maxima are not located at the same energy. This suggests that the position of the peak in the B(E1) distribution could provide a hint on the possible validity of the popularly used "di-neutron cluster" model.

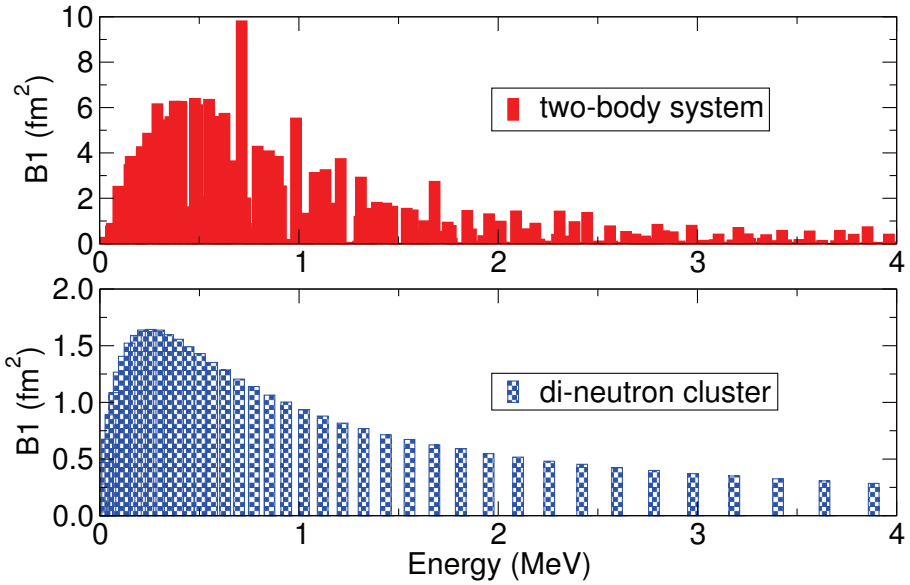

Figure 4.9: Results for the B_1 transition intensities in the microscopic two-body approach (upper panel, THO with N= 100) compared with the di-neutron cluster calculation (lower panel, THO with N= 200).

4.2 Scattering of two particles in the field of two potential wells

The next step is the extension to reaction processes involving the two-particle systems studied in the previous sections.

In this case we have an initial two-particle state $\Psi(x_1, x_2, t_i)$ generated by the fixed well (as explained in section 4.1) and we follow the time evolution of the two-particle wave function due to action of the moving one-body potentials. Since each particle feels the ineraction with each potential independently from the other one, we should include them twice in the Hamiltonian

$$\begin{aligned}\mathcal{H}(x_1, x_2, t) = -\tfrac{\hbar^2}{2\mu}\left[\tfrac{\partial^2}{\partial x_1^2} + \tfrac{\partial^2}{\partial x_2^2}\right] + V_T(x_1) + V_T(x_2) \\ + V_P(x_1 - x_1^p(t), t) + V_P(x_2 - x_2^p(t), t) + V_{int}(x_1, x_2), \end{aligned} \tag{4.23}$$

where $x_1^p(t)$ and $x_2^p(t)$ indicate the projectile well trajectories along the two dimensions in which each particle move (i.e. x_1 and x_2). They move following the classicl trajectory of equation (3.2), and time is expressed in units of Plank's constant . In addition, one can include a residual pairing interaction $V_{int}(x_1, x_2)$ between the two valence particles. The pairing interaction is taken to be a density-dependent zero-range potential as presented in equation (4.1), and hence it acts only when the two particles are both inside the same well. We can set different parameters for the residual interaction of each potential well. The solution is obtained by solving numerically the time-dependent Schroedinger equation

$$i\frac{\partial}{\partial t}\Psi(x_1, x_2, t) = \mathcal{H}(x_1, x_2, t)\Psi(x_1, x_2, t). \tag{4.24}$$

In particular, we integrate the differential equation using a finite-diference method, such as the Runge-Kutta method. As in the single-particle case, we make use of the routines *D02PVF* and *D02PCF* of the NAG library[4] [5].

[4] Those NAG routines provide the solution of a one-dimensional differential equation, but the two-body wavefunction $\Psi(x_1, x_2, t)$ is defined on a squared grid where the two coordinates x_1 and x_2 are the one-dimensional coordinates of the two neutrons respectively. So we just define $\Psi(x_1, x_2, t)$ as a one-dimensional vector composed of each line of the squared grid read sequentially.

[5] We are also imposing vanishing boundary conditions.

At the end of the process one can single out the population of the different final channels, by integrating the final total wavefunction $\Psi(x_1, x_2, t_f)$ over the corresponding areas shown in figure 4.10:

- The elastic and inelastic scattering probability corresponds to the situation in which both particles remain in the initial well. To evaluate this quantity we should integrate the wavefunction inside the area occupied by the initial total wavefunction, above the target potential. This area is highlighted with the big blue squares in panels (a) and (b) of figure 4.10.

- The one-particle transfer occurs when one particle remains in the initial well and the other goes to the moving one. The corresponding probability is computed by integrating the final wavefunction in the areas in which the projectile potentials stop at the end of the time evolution. They are depicted in panel (b) of figure 4.10 as green rectangles.

- The two-particle transfer probability, which corresponds to the probability that both particles transfer to the moving well, is evaluated as the integral over the region along the $x_1 = x_2$ bisector which corresponds to the final projectile position. This area is marked with the small magenta square in panel (b) of figure 4.10.

- The one-particle breakup (one particle in the continuum outside the wells and one in the target or projectile well), and the two-particle breakup (both particles outside the wells) probability corresponds to the remaining probability (the problem is unitary). We expect to find this components outside the previous areas, and, in particular, we suppose that the two-neutron breakup component concentrates in the area inside the black circle in panel (b) of figure 4.10.

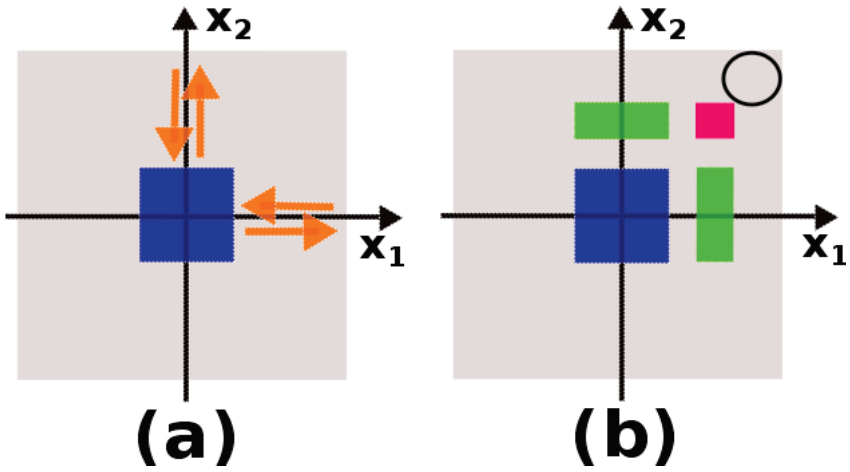

Figure 4.10: The big gray area of coordinates x_1 and x_2 is the space in which the two neutrons move in our model. Panel a: schematic representation of the area corresponding to the initial two-body wavefunction (blue square) above the target potential well, and the direction in which the projectile potentials move (indicated by the arrows). Panel b: schematic representation of the areas corresponding to the final wavefunction components, i.e. Elastic/inelastic (blue big square) scattering, one-neutron transfer (green rectangles, each one corresponding to the transfer of one of the two neutrons), and two-neutron transfer (small magenta square). The breakup component is expected to be outside the previous areas, in particular we expect the two-neutron breakup to concentrate in the area inside the black circle.

4.2.1 Influence of the pairing interaction on the reaction process

It is interesting to study the reaction mechanism by switching on or off the pairing interaction.

We first consider the case in which the pairing interaction is switched off (uncorrelated case). In this case both particles initially sit in an uncorrelated way in one single-particle state of the target potential well. As initial conditions we choose two Woods-Saxon (2.1) potentials to generate the single-particle basis of target and projectile. In particular, for the target we fix the paramenters $V_0^T = -1.29$ MeV, $R^T = 1.80$ fm, and $\alpha^T = 0.67$ fm, while for the projectile we use $V_0^P = -1.10$ MeV, $R^P = 2.0$ fm, and $\alpha^P = 0.65$ fm. The reduced mass for this case is $\mu = 0.975$ amu. To generate the bound two-body state in this uncorrelated case, we include one single-particle bound state in addition to the continuum pseudostates[6] The projectile follows the (3.2) trajectory with a constant acceleration $a = 3000/\hbar^2$ fm/ps^2 [7]. The two-particle bound state energies obtained are $E_{2b}^T = -0.39$ MeV and $E_{2b}^P = -0.34$ MeV. An example of the corresponding wavefunction is given in figure 4.11 (upper-left frame) as a contour plot as a function of x_1 and x_2. Note that in this case the wavefunction spatial part is symmetrical, so it shows equal probabilities for the two particles to be on the same side of the potential (cluster-like configuration) or on opposite sides (cigar-like configuration). We then follow in time the two-particle wavefunction according to the time-dependent Schroedinger equation (4.24). The upper-right frame displays the wavefunction at the end of the process. From this wavefunction we can separate the different final states, described in the previous section. In this specific case breakup processes (both one and two-particle) are negligible. The total one-particle transfer probability P_1 amounts to about 40%, while the two-particle transfer probability P_2 amounts to about 4%. Due to the absence of correlations the transfer process is induced by the one-body mean-field generated by the moving well, and in terms of reaction mechanism the two-particle transfer can only be interpreted as produced by the successive

[6] We discretize the continuum using the THO method presented in section 2.2.2. In particular, we include $N_{THO} = 75$ basis states, we also use $\gamma/b = 1.2$ fm$^{-1/2}$ and an energy cutoff of 50.0 MeV in the continuum.

[7] For this case the time is expressed in unit of $\hbar$.

transfer of single particles. In such a situation, in a perturbative approach, we expect a pair transfer probability

$$P_2 \sim (P_1)^2/4, \tag{4.25}$$

which is precisely the value obtained in our calculation.

We move now to the case with correlations. For this calculation we fix the target paramenters $V_0^T = -5.80$ MeV, $R^T = 2.50$ fm, and $\alpha^T = 0.67$ fm, and for the projectile we use $V_0^P = -23.6$ MeV, $R^P = 2.00$ fm, and $\alpha^P = 0.65$ fm. The reduced mass for this case is $\mu = 0.975$ amu. The projectile follows the (3.2) trajectory with same acceleration as in previous example. The initial wave function is obtained by diagonalizing the residual pairing interaction in the two-particle basis. We choose for the residual interaction (4.1) the parameters $V_{RI}^T = -58.50$ MeV and $V_{RI}^P = -58.95$ MeV for target and projectile respectively in order to obtain the two-particle bound state energies as similar as possible: $E_{2b}^T = -5.94$ MeV and $E_{2b}^P = -6.23$ MeV. The parameters $\rho_0 = 0.15$ fm^{-1} and $p = 1$ are the same for both potentials. Since we assume that the core occupies all the bound levels, we do not include those states in the calculation. The continuum is discretized in the same way as in the uncorrelated case.
The corresponding initial and final wave functions are shown in the lower frames of figure 4.11. In the case with correlations, the presence of the pairing interaction, which is a two-body operator, makes possible the simultaneous transfer of the two neutrons in addition to the the successive transfer of single particles. The effect of this initial correlation will propagate during the scattering process and affect the final wavefunction (lower-right frame). As in the previous uncorrelated case we can separate the probabilities for the population of the different final channels. One gets a total one-particle transfer probability P_1 equal to 52% and a pair transfer probability P_2 equal to 13%. This latter value is a factor 2 larger than the uncorrelated estimate of equation (4.25). This factor represents therefore the enhancement factor due to the pairing correlation: the probability of finding both particles on the same side is now clearly favored.

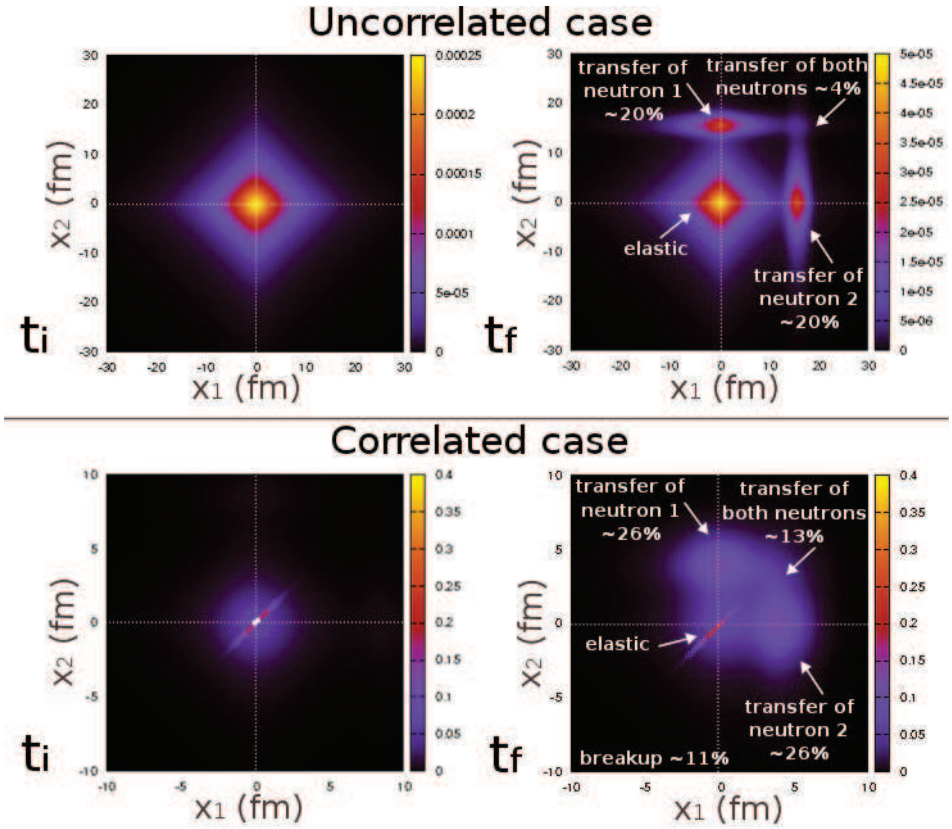

Figure 4.11: Two-body wavefunctions for the uncorrelated (upper) and correlated (bottom) cases. The initial (left) and final (right) results are presented.

4.2.2 Influence of the binding energy on the reaction process

Let us test now the system behaviour by changing the two-body bound state energy of the two potential wells.

For the uncorrelated system we choose as initial parameters the same of the uncorrelated case presented in the previous section. In this case we fix the target two-body ground state energy at -0.34 MeV, and vary the projectile energy by changing the one-body potential depth in the range $[-2.2; -1.1]$ MeV. In the left panel of figure 4.12 the probabilities for the different channels are shown as a function of the projectile two-body energy state. As one can deduce from the results, the transfer probability increases as the projectile state becomes more and more weakly-bound. This is due to the stronger overlap between the initial and final state during the process. The breakup component also increases, as one can expect treating weakly-bound systems. Note that the two-neutron transfer probability predicted by the perturbative theory expressed in equation (4.25) agrees well with the results of our calculations (see right panel of figure 4.12).

In the case of correlated system we have chosen initially for both target and projectile the same model case parameters used for the description of the two-neutron halo nuclei structure in section 4.1. As in the uncorrelated case, we study the probability changing the two-body projectile energy, but now we change this parameter by varying the residual interaction strength parameter in the range $[-35.0; -65.0]$ MeV, keping the target residual interaction fixed at -50.0 MeV, corresponding to a two-body ground state energy of -4.13 MeV. These results are reported in figure 4.13.
In this case, as in the uncorrelated one presented in figure 4.12, we note an increment of transfer and breakup probability decreasing the projectile energy. This is due, as we mentioned for the uncorrelated case, to the larger overlap between target and projectile two-body wavefunctions during the process, which increases as the projectile becomes more weakly-bound and its wavefunction tail extends over a larger region. For this correlated system the two-neutron trasfer probabilities (zoomed in left panel of figure 4.13) do not follow the perturbative prediction: the two-body transfer is enhanced with respect to the result of equation (4.25), even if it increases less strongly than one-body transfer.

Another interesting test is the variation of the two-body state energy for

both target and projectile, keeping them equal. To do so, we change the value of the residual interaction of the two wells in a range of $[-35.0; -60.0]$ MeV. The results are shown in the left panels of figure 4.14. In this case, as the target and projectile become more weakly-bound the wavefunctions related to both potentials extend over larger regions, thus increasing considerably the overlap during the process respect the previous test. This results in a faster increment of transfer and breakup probabilities with respect to the case of figure 4.13. Again, the two-neutron probability is clearly enhanced with respect to the perturbative estimate of equation (4.25) (see the comparison of these two results in the left panel of figure 4.14).

In conclusion, aside from verifying the stronger transfer and breakup probability in the case of weakly-bound systems, we confirm the enhancement of two-neutron transfer due to pairing interaction. For an uncorrelated system, the results clearly follow the perturbative prediction: the only possible way to transfer a pair is in two succesive moments. When we include the pairing interaction between the two halo nucleons, the enhancement of the two-neutron transfer respect to the perturbative estimate proves the possibility to transfer the two particles toghether at the same time, and shows the important role of pairing interaction in the reaction mechanism.

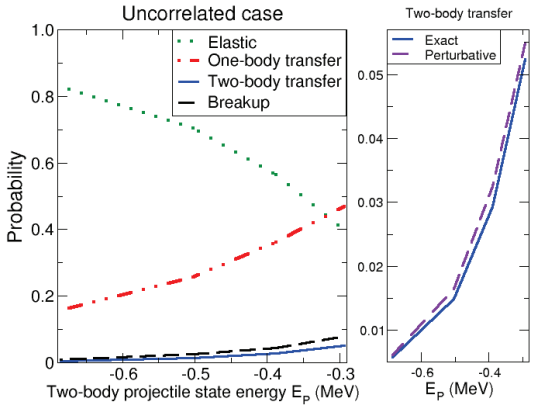

Figure 4.12: Left panel: elastic (green dotted line), one-neutron transfer (red dashed-dotted line), two-neutron transfer (blue solid line), and breakup (black dahed line) probabilities for the uncorrelated case as a function of the projectile two-body energy state, keeping the target energy fixed at -0.34 MeV. Right panel: zoom on the two-neutron transfer (blue solid line) result and perturbative calculation (violet dahed line) obtained applying equation (4.25).

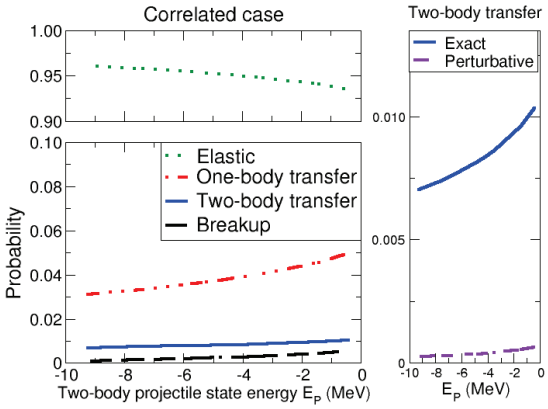

Figure 4.13: Left panels: elastic (green dotted line), one-neutron transfer (red dashed-dotted line), two-neutron transfer (blue solid line), and breakup (black dahed line) probabilities for the correlated case as a function of the two-body energy state of projectile, keeping the target energy fixed at -4.13 MeV. Right panel: zoom on the two-neutron transfer (blue solid line) result and perturbative calculation (violet dahed line) obtained applying equation (4.25).

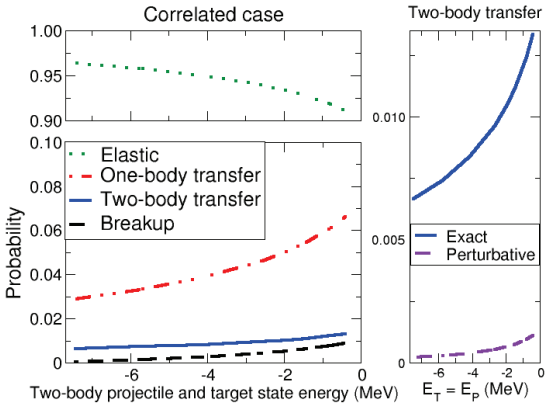

Figure 4.14: Left panels: elastic (green dotted line), one-neutron transfer (red dashed-dotted line), two-neutron transfer (blue solid line), and breakup (black dahed line) probabilities for the correlated case as a function of the two-body energy state of target and projectile. Right panel: zoom on the two-neutron transfer (blue solid line) result and perturbative calculation (violet dahed line) obtained applying equation (4.25).

Chapter 5

Summary and conclusions

In this thesis, we have investigated the structure and dynamics of weakly-bound quantum systems within a one-dimensional model. This is a timely topic in nuclear physics studies, given the interest raised in the past years by the understanding of nuclei in the proximity of proton and neutron drip-lines [65–67]. The one-dimensional model developed in this work provides a simple framework to investigate many properties of these systems, such as the role of the continuum, the consequences of the weak binding, etc), but avoiding the mathematical complexities arising in a full three-dimensional approach. As already mentioned in the introduction, we have developed the computer codes required to perform the calculations presented in this work.

The system under study is composed by an inert core, represented by a Woods-Saxon mean field potential, plus one or two valence neutrons [40]. In the case of two valence particles, we simulate the three body Borromean halo system, i.e. three-body bound systems with no bound binary sub-systems. Examples of these systems are the nuclei ^{6}He and ^{11}Li. It is well known that the residual pairing interaction between the valence neutrons plays a key role in making the full system bound. In our simplified model, this is achieved via a density-dependent delta residual interaction.
It is also well known that the positive-energy spectrum plays an essential role in the structure and collisions of these systems. Since these states form an infinite set of continuum functions, in practical calculations it is formally and computationally convenient to replace the exact continuum states by a discrete representation in terms of square-integrable functions ("pseudostates"). Therefore, we have also explored several discretization techniques. Two of them are based on a diagonalization of the system Hamiltonian in a truncated basis of square-integrable functions, for which we employ hamonic oscillator (HO) and transformed harmonic oscillator (THO) functions. We have also implemented the BOX method, in which the system is confined in a radial box and the states are obtained as the eigenstates of the system under vanishing boundary conditions at the borders of this box.
In the one-body case, in addition to the calculation of the system eigenstates, we compute transition intensities and sum rules of different operators to assess the goodness of the continuum description achieved with the different methods. Moreover, we compare our results with “exact” and approximate

approaches, thus probing the accuracy of the different discretization procedures.
For the two-body system, we build the two-particle bases[1], compute the system eigenvalues and eigenvectors, and study the bound state energy convergence and the nature of its wavefunction. We also compute the transition intensities for the two-body system for the linear (B_1) and quadratic (B_2) operators. We compare our B_1 result with the di-neutron approximation result, showing how the distributions peak at different energies. We suggest that this fact could be used to discriminate among the two approaches.

The results obtained in the one- and two-body cases for HO, THO, and BOX agree satisfactorily. The pseudostate method turns out to be a computationally efficient approach to deal with weakly-bound systems.
In the one-body case, the simplicity of the system allows the use of large basese (several hundred of elements) at a relatively computational cost. However, for the two-body system, despite the symmetrization and energy maximum cutoff, the involved matrices dimension is much larger and the problem is computationally heavier. This makes adventageous the use of the THO which, as compared to the other methods, requires a smaller basis dimension. Although this basis requires additional paramters with respect to the simpler HO method, it offers two important advantages. The first is the possibility of tuning the density of continuum states, making it possible to enlarge the pseudostates density at energies relevant for the process under study. The second advantage is the exponential asymptotic behavior of its basis elements. The combination of these two facts makes the convergence in the THO case faster than in the other two methods. Although in the present case this advantage is not decisive, in more involved many-body calculations it can be of major relevance. For further details on the comparison between HO and THO methods see appendix A.

The simplicity of the present approach allows its use to model direct reactions (elastic and inelastic scattering, transfer, and breakup processes) in a simplified and schematic way, along the line already presented in [41–44]. The reaction is modeled as a collision between two Woods-Saxon potential

[1] In order to construct the basis for the two-body case we need the solution of the one-body mean field potential, both for bound states and pseudostates.

wells in one dimension. In the case of one-particle halo nuclei, the process involves one active neutron initially sitting on a single-particle level of a Woods-Saxon potential and feeling the action of a second moving potential. The target potential is assumed to be at rest in a fixed position, whereas the projectile moves following a classical trajectory. In the case of two-particle sytems one has to construct the initial two-particle wavefunction, and its time evolution is due to the action of two moving one-body Woods-Saxon potentials. For the latter system, one can include a residual density-dependent zero-range pairing interaction between the two valence particles, acting only when the two particles are both inside the same well. The choice of the parameters entering the calculation will lead to various structural and kinematical conditions, corresponding to rather different physical situations and simulating different bombarding energy regimes, impact parameters, and Q-values for particle transfer. Essentially, one has to fix the parameters characterizing the potential wells (energies of single-particle states in both potentials), initial condition (selecting one of the levels in the target potential), distance of closest approach, and asymptotic energy of the collision. The "exact" results can be obtained by directly solving the time-dependent one- or two-particle Schroedinger equation. The probability for populating the different channels after the collision is determined by projecting the asymptotic wavefunction (i.e. the solution for large values of t) onto the corresponding eigenstates of the wells.

In the case of one-body scattering problem, the same equation is solved within the first order approximation and standard coupled-channels formalism, thus testing the validity of the necessary truncations and continuum discretization (in this case we have used the BOX method).
In particular, from this comparison, we might infer the importance of including the continuum to obtain the proper result expected from the "exact" calculation We find that, even for systems which are not so weakly bound or the breakup is not the dominant channel in the reaction, the coupling to the continuum states can be important. We also observe that, in general, transfer and breakup channels are favoured for weakly-bound systems.
When breakup becomes an important channel, it becomes mandatory to include in the coupled-channels scheme, in addition to the bound states of the system, a representation of the continuum states. This is done with the discretization methods mentioned above and described in Chapter 2. The

inclusion of the continnuum results is a significant improvement of the elastic and inelastic probabilities. Overall, the breakup probabilities are also well accounted for by these calculations. Despite this success, in these situations we face some numerical and formal problems, namely:

(i) When increasing the number of continuum pseudostates, the coupled-channels method becomes numerically unstable.

(ii) The coupled-channels method assumes that the internal eigenstates of the overlap between the projectile and target eigenstates vanish asymptotically. This condition is naturally fulfilled when only bound states of the two wells are included but, when continuum states are also present, the condition is only guaranteed if the pseudostates are artificially restricted to a spatial domain centered at the projectile or target wells, avoiding the overlap with the other potential. This introduces some arbitrariness in this approach that would deserve further investigation. As an alternative approach, we have also explored the possibility of considering continuum states extending in the entire spatial grid. Although the final result violates unitarity by a few percent, the computed probabilities compare reasonably well with the exact ones.

An interesting observation is that, when the exact solution is projected onto the projectile and target positive energy states, the corresponding probabilities display distinct features in the proximity of the breakup threshold, which are possibly linked to the properties of the low-lying continuum of each well. In a coupled-channels scheme, this feature can only be reproduced if the continuum states belonging to both wells are included, thus raising again the problem of non-orthogonality of the two basis. Clearly, this problem deserves further investigation.

In the case of reactions involving Borromean systems (in which we discretize the continuum using THO method), our model is used to investigate the reaction dynamics in two-particle transfer processes: is the pair transferred in a single step or in a correlated sequence of two single-particle transfer through a number of intermediate states? To do so, we study the influence of the weak binding energy and of the pairing interaction between the valence particles in the halo.

We confirm the stronger transfer and breakup probability in the case of

weakly-bound systems, that we have verified in the one valence particle case. This is due to the halo wavefunction tails which extend over a longer range, thus favouring a stronger interaction with the reaction partner; while the weakly-bound nature makes the nucleus more easy to break up.
We also observe an enhancement of two-neutron transfer due to pairing interaction. For an uncorrelated system, the results clearly follow the perturbative prediction: the only possible way to transfer a pair is in two succesive steps. When we include the pairing interaction between the two halo nucleons, the enhancement of the two-neutron transfer with respect to the perturbative estimate proves the possibility to transfer simultaneously the two particles, and shows the fundamental role of pairing interaction in the reaction mechanism.

The present results open many possible ways to proceed the investigation on weakly-bound systems. We list some interesting and promising research lines for the future:

- This model could provide a convenient way of reckoning the importance of the pairing interaction in the continuum and the effect of resonances [68]. This implies the introduction of an ad-hoc barrier in the potential to simulate centrifugal barriers.

- By the inclusion of barriers in the potential, to account for the Coulomb interaction, this model could also give a test ground for processes involving protons [69].

- The consideration of core excitations in the model suggests also a very enticing line of research. These core excitations have been proved to play an important role in the determination of the structure of some halo nuclei [22, 24, 25, 70] and this model could offer a convenient (and simple) test ground for their study.

- This model could also provide a framework to test reactions of astrophysical interest, which is a popular field cooperating with nuclear physics, but it can also start an interchange with other fields less commonly related to nuclear physics, like atomic physics, in which this kind of simulations is rather common [71, 72].

Appendix A

Approximate continuum discretization methods comparison

In this work we have made use of continuum discretization using pseudostates obtained with two different approximate methods

- Harmonic Oscillator basis (HO), presented in section 2.2.1,
- Transformed Harmonic Oscillator basis (THO), shown in section 2.2.2.

Both approaches have their pros and cons.

The HO method is computationally very efficient and simple. The convergence of the calculation needs to be explored only as a function of the basis size, N, which simplifies the task. This method has been applied in the 70's to the calculation of resonances with stabilization plots [46] with satisfactory results. The main drawback of the HO method is the Gaussian asymptotic dependence of the basis functions. This makes basis states tend to zero much faster than the exponentially decaying bound states. A sensible election of the inverse oscillator length parameter a can help to deal with weakly-bound states, as explained in appendix D.1. However, the HO approach requires larger N values to obtain the bound system eigenvalues with a certain degree of accuracy compared to the other methods.

The main advantage of the THO method is that it corrects the asymptotic Gaussian dependence of basis functions of the HO case, including the useful possibility of tuning via the γ/b parameter value the distribution of pseudostates in the positive energy region. As in the HO case, the only parameter that needs to be varied looking for convergence is N, the basis size. The THO makes calculations more involved, but the degree of complexity is not too high and computing time increments are almost negligible. This is certainly so with the analytical local scale transformation (LST) from [51] compared to the original formulation of the THO method [73]. As we have stated, another difference with the HO method is that we need to assign values to the γ/b ratio parameter. The best option is to fix it considering the continuum region which is of major interest in each particular case and give γ/b values according to this [50].

Let us illustrate in a particular case the possible advantage of using the LST transformation, as compared to the pure HO basis. As a help for the comparison of the approaches considered in the one- and two-body cases, we present in table A.1 the basis dimension in the HO and THO cases such that for a $\Delta N = 10$ the variation in the bound eigenvalues of the Woods-Saxon model potential is $\Delta E_b < 5$ keV.

	N	$x_{max}(fm)$
$HO^{(1)}$	90	55.0
$HO^{(2)}$	50	60.0
$THO^{(1)}$	50	75.0
$THO^{(2)}$	20	75.0

Table A.1: One body dimension N and integration length x_{max} required to achieve converged energies for the different methods. In the $HO^{(1)}$ case the inverse oscillator length a is assessed with $N = 1$ calculation, though in the $HO^{(2)}$ case the value of a is fixed using a recipe described in appendix D.1. The $THO^{(1)}$ and $THO^{(2)}$ notation stands for THO with $\gamma/b = 2.4$ fm$^{-1/2}$ and $\gamma/b = 1.2$ fm$^{-1/2}$, respectively.

The $HO^{(1)}$ and $HO^{(2)}$ notation stands for truncated Harmonic Oscillator basis in which: in the $HO^{(1)}$ case the inverse oscillator length a is determined with $N = 1$ calculation, whereas in the $HO^{(2)}$ case the value of a is fixed using a recipe described in appendix D.1, aiming to improve the description

of weakly-bound states. The THO$^{(1)}$ and THO$^{(2)}$ notation stands for THO with $\gamma/b = 2.4$ fm$^{-1/2}$ and $\gamma/b = 1.2$ fm$^{-1/2}$, respectively. The value of x_{max} is the integration interval in both cases; integrals range from $-x_{max}$ to $+x_{max}$ and we check that this value is large enough in each case by computing the basis states normalization.

In figure A.1 the least-bound state of the model Woods-Saxon potential $\Psi_2(x)$ is depicted for HO$^{(1,2)}$ and THO$^{(1,2)}$. Panel (a) shows the full spatial dependence of $\Psi_2(x)$, and panel (b) shows a zoom in logaritmic scale of the wavefunction tails, where differences are more noticeable. It can be seen that the THO achieves a better description of the wavefunction tail with a smaller number of basis states.

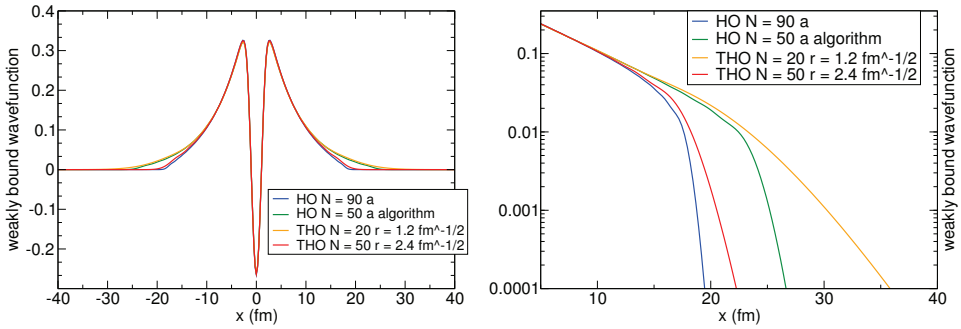

Figure A.1: Panel a: the weakly-bound wavefunctions for the 1D one-body problem calculated with HO and THO basis using different parameters. Panel b: the logaritmic plot of the wave functions tails; the main differences are located on the tails region, and in particular it can be noticed that with THO$^{(2)}$ one can reproduce the proper tail using a smaller number of basis states.

In figure A.2 we include, for the one-body case, the results obtained for the total strength sum rule of $\Psi_2(x)$ with the four approaches considered in table A.1.

Finally, for the two-body case, we study the weakly-bound ground state energy dependence with N in table A.2 as well as a plot of the ground state energy (panel a) and (panel b) ground state anomalous density value (as defined in section 4.1.2) in figure A.3.

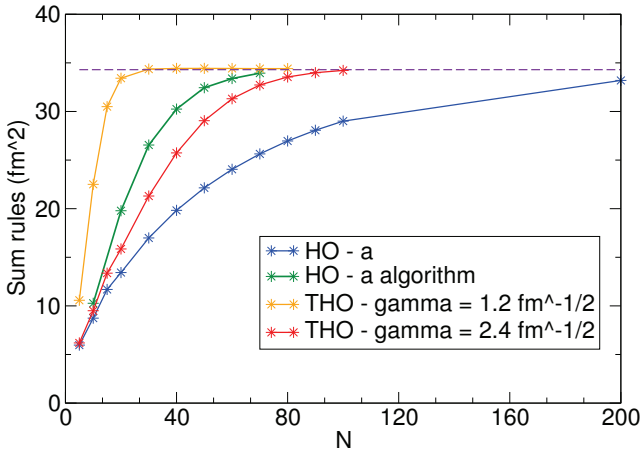

Figure A.2: The total strength sum rule convergence calculated with the weakly-bound state for the 1D one-body problem in a Woods-Saxon potential, for HO and THO methods.

	N_{1b}	$x_{max}(fm)$
$\mathrm{HO}^{(1)}$	200	30.0
$\mathrm{HO}^{(2)}$	45	75.0
$\mathrm{THO}^{(2)}$	50	75.0
$\mathrm{THO}^{(1)}$	85	75.0

Table A.2: One-body dimension N and integration length x_{max} required to achieve converged two-body energy for the different methods. In the $\mathrm{HO}^{(1)}$ case the inverse oscillator length a is determined with $N = 1$ calculation, whereas in the $\mathrm{HO}^{(2)}$ case the value of a is fixed using a recipe described in appendix D.1. The $\mathrm{THO}^{(1)}$ and $\mathrm{THO}^{(2)}$ notation stands for THO with $\gamma/b = 2.4$ fm$^{-1/2}$ and $\gamma/b = 1.2$ fm$^{-1/2}$, respectively.

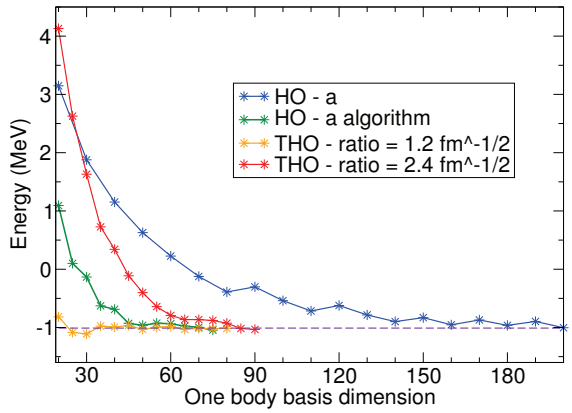

(a) Two-body energy

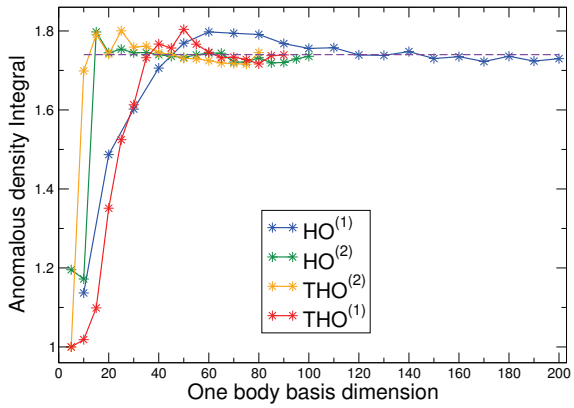

(b) Anomalous density

Figure A.3: Panel a: the energy convergence for the 1D two-body problem in a Woods-Saxon potential for HO and THO methods. Panel b: the anomalous density for the ground state convergence for HO and THO methods.

As can be seen in the tables A.1 and A.2 and in the figures A.1, A.2, A.3, results from the three approaches are in good agreement, as expected. The THO$^{(2)}$ seems the most flexible method, as it manages to obtain converged energies and a fairly good description of asymptotic wave functions. Among the considered method for the one-body case, this is the case with the fastest convergence and a best asymptotic wave function description.
The difference in basis sizes in tables A.1 and A.2 seems not too dramatic in this case, but we should take into account that these continuum discretization methods are of interest for two-body studies and beyond [74–77] and in this case having a small one-body basis confers a very important advantage in the full problem.
The convenience of THO$^{(2)}$ is further confirmed in the one-body case by the fast convergence of the Total strength sum rule for the $\Psi_2(x)$ weakly-bound state, and in the two-body case for the fast energy and anomalous density convergence.
It is important to emphasize that all methods agree on the large N limit for the different quantities computed.

Appendix B

Continuum structure: resonances and virtual states

By observing what happens to the bound states of a one dimensional potential well (with barriers) $V(x)$ as it becomes less deep, one should notice that the bound states move up to the zero energy threashold and evetually disappear into continuum [78]. Shortly after a bound state ceases to exist, a new resonance state appears above the well. In the interim a virtual state is formed at the threshold energy. Decreasing the potential depth, it melts with another virtual state that is moving up towards it. This melt gives rise to a pair of complex energy states inside the well which eventually become a resonance above the well and its conjugate virtual state.
The solutions of the time-independent Scroedinger equation for a square well

$$\left[-\frac{\hbar^2}{2\mu}\frac{d^2}{dx^2} + V(x) - E\right]\Psi(x) = 0 \tag{B.1}$$

is given by

$$\Psi(x) = \begin{cases} ce^{ik_0x} + c'e^{-ik_0x}, & x < -L \\ ae^{ikx} + be^{-ikx}, & -L < x < L \\ de^{ik_0x} + d'e^{-ik_0x}, & x > L \end{cases} \tag{B.2}$$

where $[-L, L]$ defines the range in which the potential $V(x)$ is defined, $k = \sqrt{2\mu(E+V)}/\hbar$ and $k_0 = \sqrt{2}/\hbar$. The coefficients a, b, c, c', d, d' are constants depending on boundary conditions. The functions $e^{\pm ikx}$ are

waves moving to $+\infty$ or $-\infty$ according to the sign + or −. By requiring $c = d' = 0$ (or $c' = d = 0$) we define an outgoing (or incoming) wave.
Real solutions of the equation (B.1) are possible only for $E < 0$, when k_0 is purely imaginary ($k_0 = i|k_0|$), and the outgoing waves become decaying exponentials belonging to bound states: $\Psi \to e^{-|k_0|x}$ when $x \to \infty$. When k_0 is purely imaginary but negative ($k_0 = -i|k_0|$) and $E < 0$ we are in the presence of a virtual state; in this case the solution is an incoming wave. Although these are non-physical solutions with negative energies, their signature shows up at positive energies (for example, as a bump in the breakup probability distributions). Complex energy solutions are related to resonances if $Im(E) < 0$ fixing outgoing boundary conditions, and to conjugate virtual states if $Im(E) > 0$ for the case of incoming waves. The conjugate virtual states, also called "capture resonance states", are associated with exponential divergent asymptotes; while resonant states are recognized among continuum levels because most of their probability density is concentrated in the potential area.

B.1 Study of resonances in one dimension

Some of the most striking effects in scattering theory are associated with resonances. The appearance of a resonance in the continuum of a quantum system implies sudden changes of phase shifts and reflection/transmission coefficients at particular energy values, associated with the resonance. This implies the occurrence of a "quasibound" state of the scattering potential, that is, a long-lived state which has sufficient energy to breakup into two or more subsystems.
The usual approach to resonances implies the study of complex poles of the scattering matrix and complex eigenvalues of the system Hamiltonian $\epsilon = E - i\Gamma/2$ (Gamow-Siegert functions [79]). A standard approach to study resonances imply complex scaling, defining a complex scaled Hamiltonian, and associating the resonance to a single square-integrable eigenfunction of this scaled Hamiltonian [80].
Simpler alternatives to study resonances are quantum-mechanical stabilization methods, using bound-state techniques [46, 81, 82]. This approach is based on the fact that the resonance wavefunction in the potential region is akin to a bound state wavefunction. When the energies of a system

possessing resonances are plot as a function of the basis dimension (or, more generally, any non-linear parameter characterizing the basis extension), there are certain eigenvalues that vary very little compared to the rest: they mark the resonant state energies, and thus the name stabilization plot [83].
Resonances are pervasive in 2D and 3D systems due to centrifugal barrier effects. In order to study resonances using pseudostates in a 1D system without including Coulomb interaction, we consider first the potential studied by Hazi and Taylor [46] to reproduce their results. We also address an analytical case, namely the Ginocchio potential, which has been previously studied with THO states in 3D [84], and as a third example we define a Woods-Saxon with barriers.
We show stabilization plots for each of the cases as a function of the relevant parameters and compute the resonance energy from the stabilization plots. We also plot the resonant wave functions.

Hazi-Taylor potential

We have first reproduced the Hazi-Taylor potential resonances [46].
The Hazi and Taylor potential is defined as

$$V(x) = \begin{cases} \frac{1}{2}x^2 & x \leq 0 \\ \frac{1}{2}x^2 e^{-\lambda x^2} & x \geq 0 \end{cases} \tag{B.3}$$

where $\lambda > 0$. In Figure B.1 we plot the potential and its first wave functions.

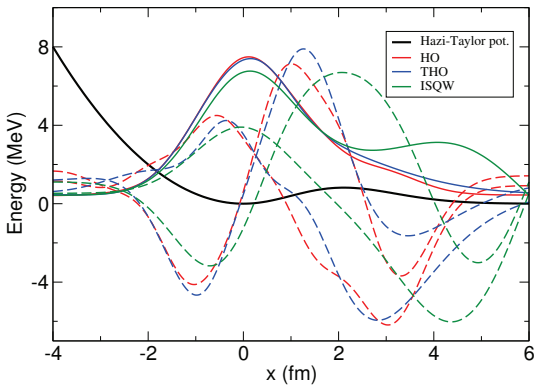

Figure B.1: The Hazi-Taylor potential with its first three wavefunctions calculated with each method; in solid line the resonant waves.

Using the parameters from reference [46] and the HO method, the energies and the wavefunctions have been perfectly reproduced. The stabilization plot for the HO case as a function of the basis size is shown in figure B.2 (left panel), while in the right panel the resonance wave function in shown for different N values.

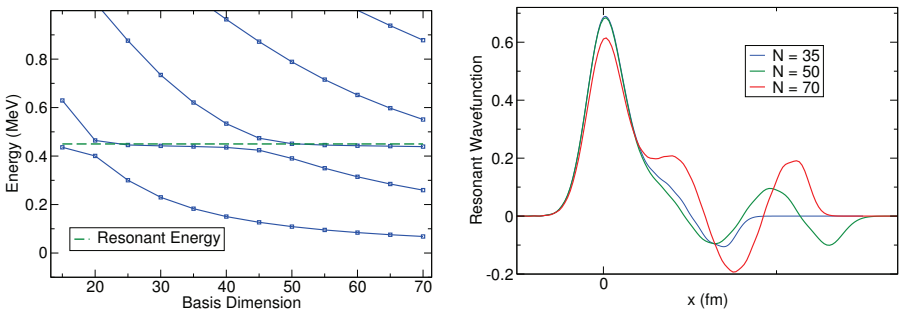

(a) (b)

Figure B.2: Left panel: stabilization plot in the HO case as a function of N for the Hazi-Taylor potential. The green dashed line corresponds to the nominal resonance energy. Right panel: the resonance wavefunction for different basis dimension values.

The stabilization plot with the box radius x_b is shown in figure B.3 in the BOX case. The THO case results are shown in figure B.4 with stabilization plots as a function of the basis dimension (left panel) and γ/b ratio (right panel). The resonance wave function obtained with the THO basis is shown in figure B.5 (in left panel varying N, in the right panel varying γ/b).

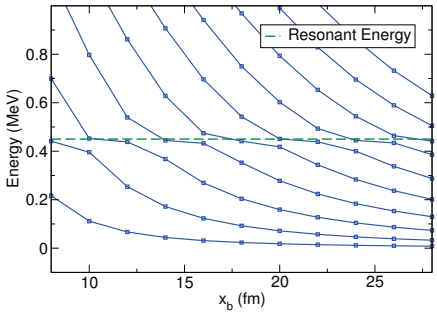

Figure B.3: Stabilization plot in the BOX case as a function of the box radius x_b for the Hazi-Taylor potential. The green dashed line corresponds to the resonance energy.

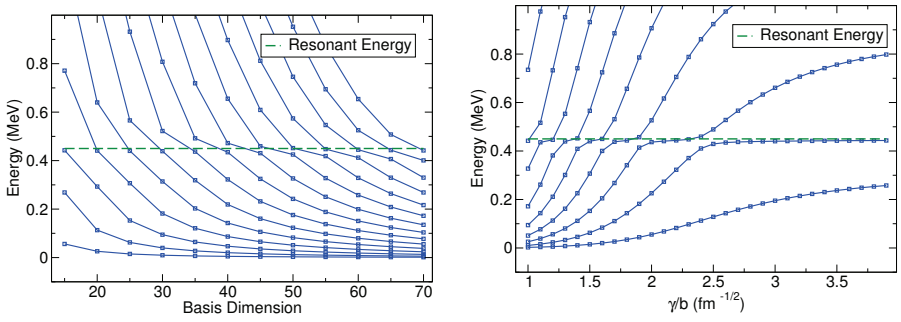

(a) (b)

Figure B.4: Stabilization plots in the THO case (in panel a as a function of N and in panel b as a function of γ/b) for the Hazi-Taylor potential. The green dashed line corresponds to the resonance energy.

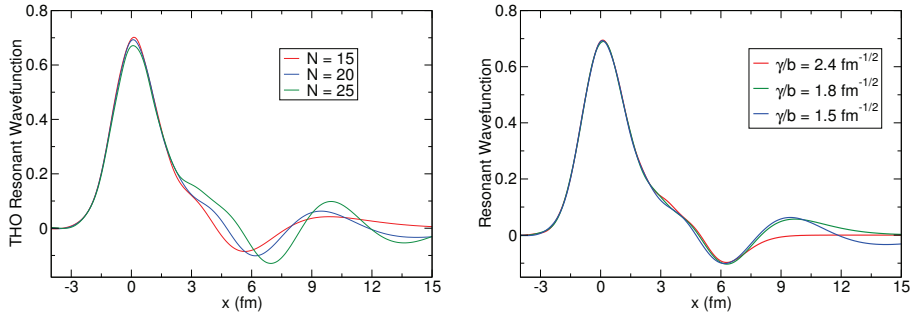

(a) (b)

Figure B.5: Left panel: resonance wavefunction for the Hazi-Taylor potential in the THO case varying the basis dimension N for a fixed value of $\gamma/b = 1.5$ fm$^{-1/2}$. Right panel: resonance wavefunction for the Hazi-Taylor potential in the THO case and varying γ/b for a fixed value of the basis dimendion N = 20.

Ginocchio potential

Resonances for the Ginocchio potential [85] have been reproduced according to [84] using HO and THO methods.

The Ginocchio potential is

$$\frac{V(x)}{V_0} = -\lambda^2\nu(\nu+1)(1-y^2)+\left(\frac{1-\lambda^2}{4}\right)(1-y^2)[2-(7-\lambda^2)y^2+5(1-\lambda^2)y^4] \tag{B.4}$$

where

$$x(y) = \frac{1}{\lambda^2}\arctan h(y) + [\lambda^2 - 1]^{1/2}\arctan([\lambda^2 - 1]^{1/2}y), \tag{B.5}$$

the parameter λ regulates the wideness of the potential, ν the the number of bound states.

We report the stabilization plots or both HO and THO cases in figures B.6 and B.7. In particular, in the THO case we plot the energy as a function of N (with γ/b fixed at 2.6 $fm^{-1/2}$) or of the γ/b (with N fixed at 30).

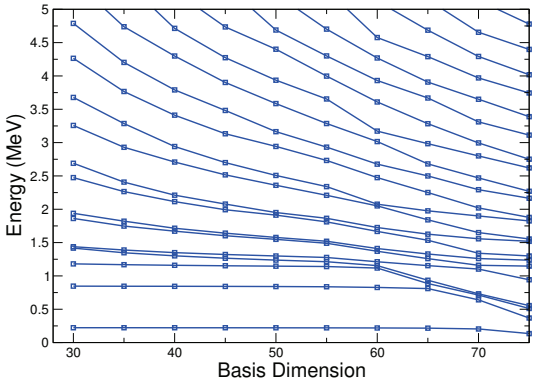

Figure B.6: The stabilization plot in the HO case as a function of the basis dimension N for the Ginocchio potential.

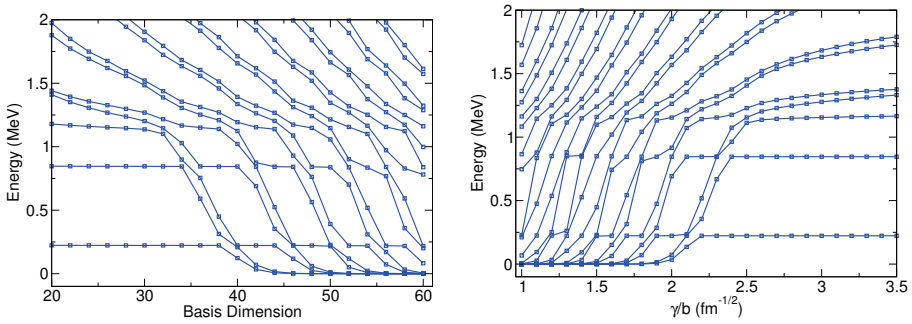

(a) (b)

Figure B.7: Stabilization plots in the THO case for the Ginocchio potential as a function of N (with the ratio fixed at 2.6 $\mathrm{fm}^{-1/2}$) in the right panel, and of the ratio (with N fixed at 30) in the left panel.

Woods-Saxon potential with barriers

The Woods-Saxon with barriers potential is defined as

$$V(x) = V_{WS}(x) + V_1 e^{-(|x|-x_0)^2} \tag{B.6}$$

where V_{WS} is the standard potential of equation (2.1).
The parameters chosen are the same used in chapter 2, and, in addition

$$V_1 = 30 \ MeV \tag{B.7a}$$

$$x_0 = 4.0 \ fm \tag{B.7b}$$

This potential has resonances, we show them in the stabilization plots of Figure B.8 for the HO and THO ($\gamma/b = 2.4 fm^{-1/2}$) cases.

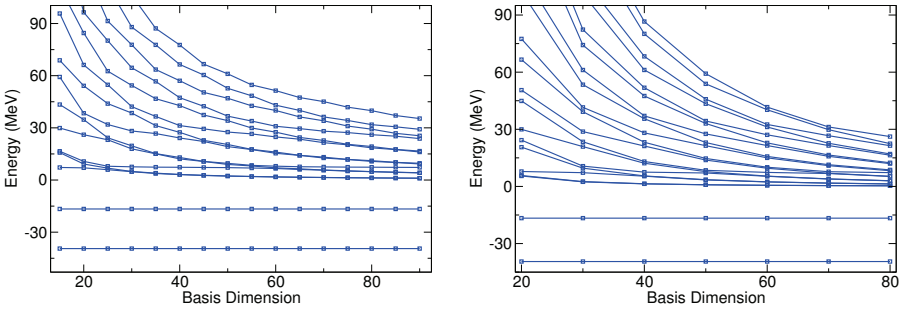

(a) HO (b) THO

Figure B.8: Left panel: stabilization plot in the HO case as a function of the basis dimension for the Woods-Saxon potential with barriers. Right panel: stabilization plot in the THO case as a function of the basis dimension fixing $\gamma/b = 2.4 fm^{-1/2}$ for the Woods-Saxon potential with barriers.

In Figure B.9 it can be appreciated the first resonant wave function (red); note that it is very narrow and concentrated into the potential range.

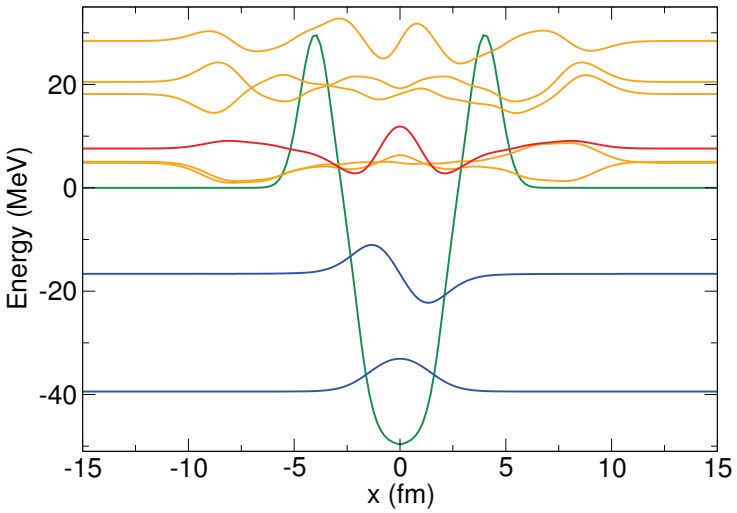

Figure B.9: The Woods-Saxon with barrier potential and the first wave functions calculated with the HO method. In red the resonant wave function; its probability density is higher into the potential.

B.2 Signature of a virtual state in the breakup probabilities

In figure 3.13, the projectile distribution of probability presents a very sharp peak at small energy (around 0.06 MeV above the breakup threshold). It can not represent a resonance because of the one-dimensional nature of the problem and because of the absence of barriers, so it might indicate the presence of a virtual state. To check if the projectile well we are using for the model case B has a virtual state at positive energy 0.06 MeV, we depicted in figure B.10 the square value of energy as a function of the potential depth. For a depth of 5.0 MeV, which is exactly the parameter we are using to construct the projectile potential, the system should present a virtual state at 0.06 MeV. The fact that the momentum corresponding to this state (proportional to $\sqrt{E}$) is negative also supports the presence of a virtual state.

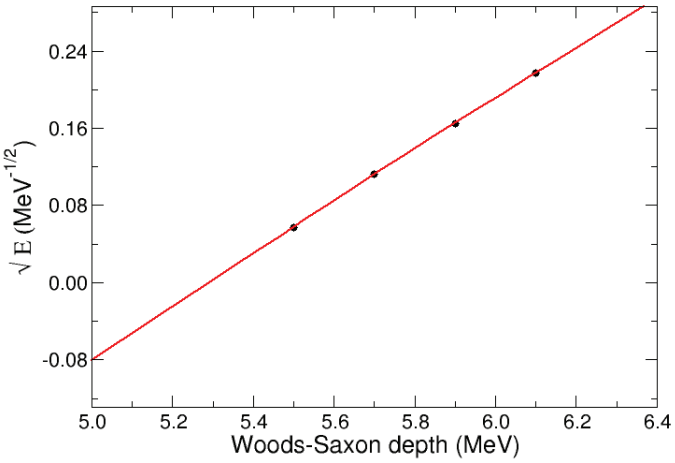

Figure B.10: Determination of the virtual state energy for the test case B discussed in chapter 3.

Appendix C

Non-covariance of Schroedinger equation in non-inertial reference frames

In classical physics and special relativity the inertial frames of reference are defined as those frames in constant, rectilinear motion with respect to another. Measurements in one inertial frame can be converted to measurements in another by a simple transformation (the Galilean transformation in Newtonian physics and the Lorentz transformation in special relativity). A non-inertial reference frame is an accelerated frame with respect to an inertial one. The laws of motion in non-inertial frames do not take the simple form they do in inertial frames: to explain the motion of bodies within the viewpoint of non-inertial reference frames, fictitious (or inertial) forces must be introduced to account for the observed motion, such as the Coriolis force or the centrifugal force.

To have a schematic visualization of the situation, imagine a glass full of water. If you accelerate it, you can see how the water surface inclinates under the effect of the inertial forces; when the acceleration is sufficiently high, the water could also fall outside of the glass. In an analougus way, imagine the glass to be a potential well and the water to be the wavefunction related to its bound state. If the potential is accelerated, the wavefunction feels the inertial forces and so it appears deformed and could also have a component excaping from the well. This is due to the fact that the Hamiltonian changes under a transformation to a non-inertial frame, so the Shroedinger equation

is not covariant under Galilean boosts [86–89]. Let us consider the one dimensional Shroedinger equation[1] for a non-relativistic particle in an external field $V(x,t)$

$$i\frac{\partial}{\partial t}\Phi(x,t) = \mathcal{H}\Phi(x,t), \qquad H \equiv -\frac{1}{2}\frac{\partial^2}{\partial x^2} + V(x,t). \tag{C.1}$$

This Shroedinger equation corresponds to the one we solve in this thesis for the one-body case presented in chapter 3. The inertial frame of reference indicated by coordinates x with origin corresponding to the target potential center, is the one in which we solve this problem and corresponds to the center of mass frame of reference for this system.
In our case the potential is of the form

$$V(x,t) = V(x - R(t)), \tag{C.2}$$

where $R(t)$ corresponds to the projectile equation of motion [35]. Let us consider the problem from the point of view of the frame of reference centered in the projectile potential center of coordinates y, to which we should make the general time-dependent translation defined by

$$\tau \equiv t, \qquad y \equiv x - R(t). \tag{C.3}$$

The projectile frame of reference is non-inertial because the projectile is accelerated. This is the so-called *extended Galilean transformation* [90, 91], i.e. a transformation to a rigid system having an arbitrary time-dependent acceleration.
In this frame are valid the new relations

$$\frac{\partial}{\partial t} = \frac{\partial}{\partial \tau} - \dot{R}\frac{\partial}{\partial y}, \qquad \frac{\partial}{\partial x} = \frac{\partial}{\partial y}. \tag{C.4}$$

The wavefunction of projectile non-inertial frame is defined according to a change of coordinates and a gauge transformation as

$$\Psi(y,\tau) \equiv e^{-i\dot{R}x - i\int_{t_0}^{t} dt' \dot{R}^2(t')/2}\Phi(x + R(\tau), \tau), \tag{C.5}$$

[1] Note that the Planck's constant $\hbar$ and particle reduced mass μ are all unity in this example.

where t_0 represents the arbitrarily chosen origin of time, and $\dot{R}$ corresponds to the momentum of the particle due to the motion of the well. This new wavefunction obeys

$$i\frac{\partial}{\partial\tau}\Psi(y,\tau) = -\frac{1}{2}\frac{\partial^2}{\partial y^2} + V(y + R(\tau),\tau) + \ddot{R}(t)y, \tag{C.6}$$

where the last term $+\ddot{R}(t)y$ represents the linear inertial force felt by the particle in the projectile potential well, thus showing that in the accelerated system there appears a gravitational field.

Appendix D

Other demonstrations

We collect here those demonstrations supporting the discussion, that would interrupt the flow of the text.

D.1 A procedure for the HO inverse oscillator length optimization

The inverse oscillator length parameter $a = \left(\frac{k\mu}{\hbar^2}\right)^{1/4}$ determines the curvature of the HO potential at the origin and thus, how wide is the potential.
In accordance to other cases [50] the value of this parameter is fixed to minimize the ground state energy with a small HO basis. In fact, we use a $N = 1$ basis, that is, a basis with the HO ground state as its only component to obtain an approximation to the system's ground state energy. The value of a is varied to minimize this energy.
In cases with several bound states that include weakly–bound states, as the chosen model Woods-Saxon potential, the a value obtained using the ground state is too large (Harmonic potential too narrow) and a very large number of HO states in the basis is request to sample the large x value where the weakly-bound state wavefunction tails are still significant. To overcome this problem one should diminish the a value of the oscillator in order to include the whole range of the significant states.
This can be done fixing the value by hand, though we define the following recipe or algorithm. We first make the minimization explained above; then with the value of a obtained we build the basis and the system Hamiltonian is

diagonalized. At this point it is possible to evaluate the expectation value of the x^2 operator for the weakly-bound wave function e.g. $\langle\Psi_2|x^2|\Psi_2\rangle$. We then compare this result with the same matrix element calculated for an Harmonic Oscillator basis, which in this case can be easily computed analytically using the relations (2.32), though it is more direct to make use of the creation and annihilation operator formalism:

$$\langle i|x^2|j\rangle = a^{-2}\left[\frac{2j+1}{2}\delta_{i,j} + \frac{\sqrt{j(j-1)}}{2}\delta_{i,j-2} + \frac{\sqrt{(j+1)(j+2)}}{2}\delta_{i,j+2}\right]. \tag{D.1}$$

So we can set a new inverse oscillator length a calculated analytically following equation (D.1), $\langle\Phi_2^{(HO)}|x^2|\Phi_2^{(HO)}\rangle$ with $i = j = 2$. Once obtained the new parameter we reconstruct the basis and diagonalize again before proceeding with the observables calculation.
In figure D.1 is shown the comparison between the model Woods-Saxon potential and the Harmonic Oscillator potentials obtained by minimization (label *a*), by fixing the value by hand after minimization (label *a/2*) and by following the procedure described (label *a algorithm*).
It is evident that the variation of the inverse oscillator length allows to construct a Harmonic Oscillator basis which stretches to the full bound states range limiting the number of necessary HO functions in the basis.

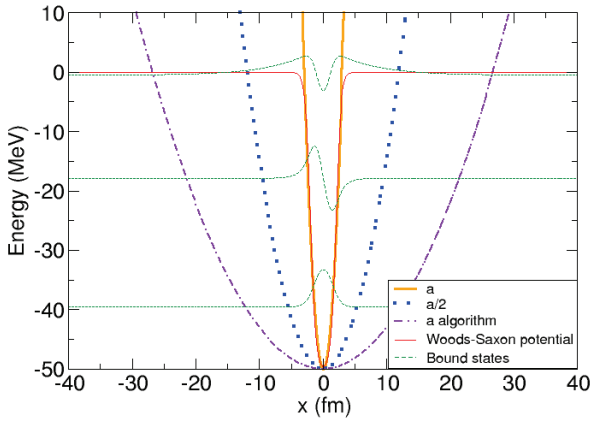

Figure D.1: The Woods-Saxon potential with the wavefunctions and the different tries for the basis harmonic oscillator.

D.2 Energy weighted sum rule demonstration

Assuming that for large N values the basis is complete $\sum_i |\Psi_i\rangle\langle\Psi_i| = 1$, and considering the time dependent Schroedinger equation $\mathcal{H}|\Psi_b\rangle = E_b|\Psi_b\rangle$ with the Hamiltonia $\mathcal{H} = -\frac{1}{2}\frac{\hbar^2}{\mu}\frac{d^2}{dx^2} + V(x)$, the energy wighted sun rule is

$$\begin{aligned}
\mathcal{E}_W^{(b)}(\mathcal{O}(x)) &= \lim_{N\to\infty} \mathcal{E}_W^{(b)}(\mathcal{O}(x), N) \\
&= \sum_i^N (E_i - E_b) \mid \langle\Psi_i|\mathcal{O}(x)|\Psi_b\rangle \mid^2, \\
&= \sum_j^N (E_i - E_b)\langle\Psi_b|\mathcal{O}(x)|\Psi_j\rangle\langle\Psi_j|\mathcal{O}(x)|\Psi_b\rangle, \\
&= \langle\Psi_b|\mathcal{O}(x)\sum_j^N |\Psi_j\rangle\langle\Psi_j|(\mathcal{H} - E_b)\sum_{j'}^N |\Psi_{j'}\rangle\langle\Psi_{j'}|\mathcal{O}(x)|\Psi_b\rangle, \\
&= \tfrac{1}{2}\langle\Psi_b|2\mathcal{O}(x)(\mathcal{H} - E_b)\mathcal{O}(x)|\Psi_b\rangle, \\
&= \tfrac{1}{2}\langle\Psi_b|2\mathcal{O}(x)(\mathcal{H} - E_b)\mathcal{O}(x) - (\mathcal{H} - E_b)\mathcal{O}(x)^2 - \mathcal{O}(x)^2(\mathcal{H} - E_b)|\Psi_b\rangle, \\
&= \tfrac{1}{2}\langle\Psi_b|\left[\mathcal{O}(x), (\mathcal{H} - E_b)\mathcal{O}(x) - \mathcal{O}(x)(\mathcal{H} - E_b)\right]|\Psi_b\rangle, \\
&= \tfrac{1}{2}\langle\Psi_b|\left[\mathcal{O}(x), [\mathcal{H} - E_b, \mathcal{O}(x)]\right]|\Psi_b\rangle.
\end{aligned} \tag{D.2}$$

Acting with the double commutator on a function $\varphi(x)$ one finally obtains

$$\begin{aligned}
[\mathcal{O}(x), [\mathcal{H} - E_b, \mathcal{O}(x)]]\,\varphi(x) &= -\tfrac{1}{2}\tfrac{\hbar^2}{\mu}\left[\mathcal{O}(x), \left[\frac{d^2}{dx^2}, \mathcal{O}(x)\right]\right]\varphi(x), \\
&= -\tfrac{1}{2}\tfrac{\hbar^2}{\mu}\left[2\mathcal{O}(x)\frac{d^2}{dx^2}(\mathcal{O}(x)\varphi(x)) - \mathcal{O}(x)^2\frac{d^2}{dx^2}\varphi(x) - \frac{d^2}{dx^2}\mathcal{O}(x)^2\varphi(x)\right], \\
&= \tfrac{\hbar^2}{\mu}\left(\frac{d\mathcal{O}(x)}{dx}\right)^2\varphi(x).
\end{aligned} \tag{D.3}$$

In this case the operator is $\mathcal{O}(x) = x$ so in the $N \to \infty$ limit the result expected is $\mathcal{E}_W^{(b)}(\mathcal{O}(x)) = \frac{1}{2}\frac{\hbar^2}{\mu}$.

D.3 The wavefunction current

An interesting observable is the wavefunction curret [11]. This quantity is defined as

$$j(x,t) = -\frac{i\hbar}{2m}\left(\Psi^*(x,t)\frac{\partial\Psi(x,t)}{\partial x} - \Psi(x,t)\frac{\partial\Psi^*(x,t)}{\partial x}\right) \tag{D.4}$$

and measures the flux of the wavefunction leaving the collision area. In this model it represents the wavefunction component escaping in the continuum.

We can demonstrate that the plane wave's current corresponds to its velocity. Given a plane wave $\Psi(x) = e^{ikx}$, its derivatives are $\frac{d\Psi}{dx} = ike^{ikx}$ and $\frac{d\Psi^*}{dx} = -ike^{-ikx}$. So

$$\begin{aligned} j &= \frac{\hbar}{2mi}\left(\Psi^*(x,t)\frac{\partial\Psi(x,t)}{\partial x} - \Psi(x,t)\frac{\partial\Psi^*(x,t)}{\partial x}\right) \\ &= \frac{\hbar}{2mi}\left(e^{-ikx}ike^{ikx} - e^{ikx}(-ik)e^{-ikx}\right) \\ &= \frac{\hbar}{2mi}2ik = \frac{\hbar k}{m} = \frac{p}{m} = v. \end{aligned} \tag{D.5}$$

Bibliography

[1] I. Tanihata, H. Hamagaki, O. Hashimoto, Y. Shida, N. Yoshikawa, K. Sugimoto, O. Yamakawa, T. Kobayashi, and N. Takahashi, Phys. Rev. Lett. **55**, 2676 (1985).

[2] I. Tanihata, T. Kobayashi, O. Yamakawa, S. Shimoura, K. Ekuni, K. Sugimoto, N. Takahashi, T. Shimoda, and H. Sato, Phys. Lett. B **206**, 592 (1988).

[3] S. G. Nilsson, K. Dan. Vidensk. Selsk. Mat. Fys. Medd. **29** (1955).

[4] B. R. Mottelson and S. G. Nilsson, Mat. Fys. Skr. Dan. Vid. Selsk. **1** (1959).

[5] K. Heyde, *Basic Ideas and Concepts in Nuclear Physics: An Introductory Approach* (IOP Publishing, 1999).

[6] I. Tanihata, J. Phys. G: Nucl. Part. Phys. **22**, 157 (1996).

[7] I. Tanihata, H. Savajols, and R. Kanungo, Prog. Part. Nucl. Phys. **68**, 215 (2013).

[8] A. S. Jensen, K. Riisager, D. V. Fedorov, and E. Garrido, Rev. Mod. Phys. **76**, 215 (2004).

[9] J. Dobaczewski, H. Flocard, and J. Treiner, Nucl. Phys. A **422**, 103 (1984).

[10] G. R. Satchler, *Introduction to Nuclear Reactions* (The Macmillan Press LTD, 1980).

[11] K. S. Krane, *Introductory Nuclear Physics* (John Wiley & Sons, 1988).

[12] H. D. Marta, L. F. Canto, R. Donangelo, and P. Lotti, Phys. Rev. C **66**, 024605 (2002).

[13] G. Rawitscher, Phys. Rev. C **9**, 2210 (1974).

[14] N. Austern, Y. Iseri, M. Kamimura, M. Kawai, and G. H. Rawitscher, Phys. Rep. **154**, 125 (1987).

[15] P. Banerjee and R. Shyam, Phys. Rev. C **61**, 047301 (2000).

[16] J. A. Tostevin, S. Rugmai, and R. C. Johnson, Phys. Rev. C **57**, 3225 (1998).

[17] S. Typel and G. Baur, Phys. Rev. C **64**, 024601 (2001).

[18] P. Capel, G. Goldstein, and D. Bay, Phys. Rev. C **70**, 064605 (2004).

[19] A. García-Camacho, A. Bonaccorso, and D. M. Brink, Nucl. Phys. A **776**, 118 (2006).

[20] R. Crespo, A. Deltuva, and A. M. Moro, Phys. Rev. C **83**, 044622 (2011).

[21] A. M. Moro and R. Crespo, Phys. Rev. C **85**, 054613 (2012).

[22] A. M. Moro and J. A. Lay, Phys. Rev. Lett. **109**, 232502 (2012).

[23] R. DeDiego, J. M. Arias, J. A. Lay, and A. M. Moro, Phys. Rev. C **89**, 064609 (2014).

[24] K. Kato, T. Yamada, and K. Ikeda, Prog. Theor. Phys. **101**, 119 (1999).

[25] K. Ikeda, T. Myo, K. Kato, and H. Toki, Clusters in Nuclei, Lecture Notes in Physics **818**, 165 (2010).

[26] T. Sawada and K. Thushima, Progr. Theoret. Phys. **76**, 440 (1986).

[27] Z. C. Kuruoğlu, Phys. Rev. C **43**, 1061 (1991).

[28] N. J. Upadhyay, A. Deltuva, and F. M. Nunes, Phys. Rev. C **85**, 054621 (2012).

[29] L. D. Faddeev, Zh. Eksp. Theor. Fiz. **39**, 1459 (1960).

[30] E. O. Alt, P. Grassberger, and W. Sandhas, Nucl. Phys. B **2**, 167 (1967).

[31] C. A. Bertulani and G. F. Bertsch, Nucl. Phys. A **556**, 136 (1993).

[32] C. A. Bertulani and G. F. Bertsch, Phys. Rev. C **49**, 2834 (1994).

[33] C. H. Dasso and A. Vitturi, Phys. Rev. C **79**, 064620 (2009).

[34] C. H. Dasso and A. Vitturi, Nucl. Phys. A **787**, 476 (2007).

[35] H. Esbensen, R. A. Broglia, and A. Winther, Ann. Phys. **146**, 149 (1983).

[36] A. Vitturi and F. Pérez-Bernal, AIP Conf. Proc. **1165**, 305 (2009).

[37] A. Vitturi and F. Pérez-Bernal, Nucl. Phys. A **834**, 482c (2010).

[38] A. Vitturi and F. Pérez-Bernal, AIP Conference Proceedings **1488**, 220 (2012).

[39] K. Hagino, A. Vitturi, F. Pérez-Bernal, and H. Sagawa, J. Phys. G: Nucl. Part. Phys. **38**, 015105 (2011).

[40] L. Moschini, F. Pérez-Bernal, and A. Vitturi, J. Phys. G: Nucl. Part. Phys. **43**, 045112 (2016).

[41] L. Moschini, J. Phys.: Conf. Ser. **566**, 012027 (2014).

[42] A. Vitturi and L. Moschini, J. Phys.: Conf. Ser. **590**, 012007 (2015).

[43] L. Moschini, A. Vitturi, and A. M. Moro, in *Basic concepts in Nuclear Physics: Theory, Experiments and Applications*, Springer Proceedings in Physics, Vol. 182, edited by J. E. García-Ramos, C. E. Alonso, M. V. Andres, and F. Pérez-Bernal (2016) pp. 181–183.

[44] A. Vitturi, L. Moschini, K. Hagino, and A. M. Moro, AIP Conf. Proc. **1681**, 060001 (2015).

[45] C. A. Moyer, Comp. Sci. Eng. **8**, 32 (2006).

[46] A. U. Hazi and H. S. Taylor, Phys. Rev. A **1**, 1109 (1970).

[47] M. Abramowitz and I. A. Stegun, *Handbook of Mathematical Functions* (Dover Publications, 1965).

[48] F. Pérez-Bernal, I. Martel, J. M. Arias, and J. Gómez-Camacho, Phys. Rev. A **67**, 052108 (2003).

[49] A. M. Moro, J. M. Arias, J. Gómez-Camacho, and F. Pérez-Bernal, Phys. Rev. C **80**, 054605 (2009).

[50] J. A. Lay, A. M. Moro, J. M. Arias, and J. Gómez-Camacho, Phys. Rev. C **82**, 024605 (2010).

[51] S. Karataglidis, K. Amos, and B. G. Giraud, Phys. Rev. C **71**, 064601 (2005).

[52] J. A. L. Valera, *Descripción de la estructura y reacciones de núcleos exóticos en una base de oscilador armónico transformado* (PhD Thesis, Universidad de Sevilla, 2012).

[53] P. Bonche, S. Koonin, and J. W. Negele, Phys. Rev. C **13**, 1226 (1976).

[54] K. Alder and A. Winther, *Electromagnetic excitation: Theory of Coulomb excitation with heavy ions* (North Holland, 1975).

[55] H. C. Brinkman and H. A. Kramers, Proc. Acad. Sci. Amsterdam **33**, 973 (1930).

[56] R. A. Broglia and A. Winther, Nucl. Phys. A **182**, 112 (1972).

[57] R. A. Broglia and A. Winther, Phys. Rep. C **4**, 154 (1972).

[58] K. Dietrich and K. Hara, Nucl. Phys. A **211**, 349 (1973).

[59] L. Corradi, S. Szilner, G. Pollarolo, G. Colò, P. Mason, E. Farnea, E. Fioretto, A. Gadea, F. Haas, D. Jelavić-Malenica, N. Mărginean, C. Michelagnoli, G. Montagnoli, D. Montanari, F. Scarlassara, N. Soić, A. M. Stefanini, C. A. Ur, and J. J. Valiente-Dobón, Phys. Rev. C **84**, 034603 (2011).

[60] L. Corradi, G. Pollarolo, and S. Szilner, J. Phys. G: Nucl. Part. Phys. **36**, 113101 (2009).

[61] G. Pollarolo, Acta Phys. Pol. B **44**, 407 (2013).

[62] G. F. Bertsch and H. Esbensen, Ann. Phys. **209**, 327 (1991).

[63] P. Schuck and P. Ring, *The Nuclear Many-Body Problem* (Springer, 2004).

[64] A. M. Moro, K. Rusek, J. M. Arias, J. Gómez-Camacho, and M. Rodríguez-Gallardo, Phys. Rev. C **75**, 064607 (2007).

[65] J. Casal, M. Rodríguez-Gallardo, and J. M. Arias, Phys. Rev. C **88**, 014327 (2013).

[66] J. Casal, M. Rodríguez-Gallardo, J. M. Arias, and I. J. Thompson, Phys. Rev. C **90**, 044304 (2014).

[67] J. Singh, L. Fortunato, A. Vitturi, and R. Chatterjee, Eur. Phys. J. A **52**, 209 (2016).

[68] R. IdBetan, G. G. Dussel, and R. J. Liotta, Phys. Rev. C **78**, 044325 (2008).

[69] T. Maruyama, T. Oishi, K. Hagino, and H. Sagawa, Phys. Rev. C **86**, 044301 (2012).

[70] M. Gómez-Ramos, A. M. Moro, J. Gómez-Camacho, and I. J. Thompson, Phys. Rev. C **92**, 014613 (2015).

[71] A. S. Kadyrov and I. Bray, Phys. Rev. A **66**, 012710 (2002).

[72] I. B. Abdurakhmanov, A. S. Kadyrov, S. K. Avazbaev, and I. Bray, J. Phys. B: At. Mol. Opt. Phys. **49**, 115203 (2016).

[73] F. Pérez-Bernal, I. Martel, J. M. Arias, and J. Gómez-Camacho, Phys. Rev. A **63**, 052111 (2001).

[74] M. Rodríguez-Gallardo, J. M. Arias, J. Gómez-Camacho, R. C. Johnson, A. M. Moro, I. J. Thompson, and J. A. Tostevin, Phys. Rev. C **77**, 064609 (2008).

[75] T. Matsumoto, E. Hiyama, M. Yahiro, K. Ogata, Y. Iseri, and M. Kamimura, Nucl. Phys. A **738**, 061601(R) (2004).

[76] T. Matsumoto, E. Hiyama, K. Ogata, Y. Iseri, M. Kamimura, S. Chiba, and M. Yahiro, Phys. Rev. C **70**, 471 (2004).

[77] T. Matsumoto, T. Egami, K. Ogata, Y. Iseri, M. Kamimura, and M. Yahiro, Phys. Rev. C **73**, 051602(R) (2006).

[78] N. Moiseyev, *Non-Hermitian Quantum Mechanics* (Cambridge University Press, 2011).

[79] G. Gamow, Z. Phys. **51**, 204 (1928).

[80] N. Moiseyev, Phys. Rep. **302**, 203 (1998).

[81] E. Holdren and J. Midtal, J. Chem. Phys. **45**, 2209 (1966).

[82] T. C. Thompson and D. G. Truhlar, Chem. Phys. Lett. **92**, 71 (1982).

[83] B. H. Lippman and T. F. O'Malley, Phys. Rev. **A2**, 2115 (1966).

[84] M. Rodríguez-Gallardo, J. M. Arias, and J. Gómez-Camacho, Phys. Rev. C **69**, 034308 (2004).

[85] J. N. Ginocchio, Ann. Phys. **152**, 203 (1984).

[86] D. M. Greenberger, Am. J. Phys. **47**, 35 (1979).

[87] S. Takagi, Progr. Theoret. Phys. **85**, 463 (1991).

[88] D. M. Greenberger, Phys. Rev. Lett. **87** (2001).

[89] A. B. vanOosten, Apeiron **13** (2006).

[90] G. Rosen, Lett. Nuovo Cim. **2**, 61 (1971).

[91] G. Rosen, Am. J. Phys. **40**, 683 (1972).